DEVELOPMENT OF A MULTICHANNEL INTEGRATED YOUNG INTERFEROMETER IMMUNOSENSOR

Aurel Ymeti

DEVELOPMENT OF A MULTICHANNEL INTEGRATED YOUNG INTERFEROMETER IMMUNOSENSOR

PROEFSCHRIFT

ter verkrijging van
de graad van doctor aan de Universiteit Twente,
op gezag van de rector magnificus,
prof. dr. F.A. van Vught,
volgens besluit van het College voor Promoties
in het openbaar te verdedigen
op donderdag 22 april 2004 te 13.15 uur

door

Aurel Fatbardha Elmaz Ymeti
geboren op 11 december 1972
te Skrapar, Albanië

Dit proefschrift is goedgekeurd door

promotor:	Prof. Dr. J. Greve
promotor:	Prof. Dr. P.V. Lambeck
assistent-promotor:	Dr. Ir. J.S. Kanger

CONTENTS

6. DRIFT CORRECTION IN THE MULTICHANNEL IO YI FOR SENSING APPLICATIONS

7. INTEGRATION OF MICROFLUIDICS WITH A FOUR-CHANNEL IO YI IMMUNOSENSOR

8. MULTIPLE WAVELENGTH APPROACH

9. DISCUSSION AND CONCLUSIONS

10. FURTHER DEVELOPMENT OF THE MULTICHANNEL INTEGRATED INTERFERENCE-BASED SENSORS

CHAPTER ONE

INTRODUCTION

In this chapter, a brief introduction to bio-chemical and immuno sensors will be presented. The immunosensing principle will be introduced followed by a short survey of the current status of optical immunosensors developed so far. Here, we will limit ourselves to the discussion of some widely used optical techniques. An overview of all possible technologies is beyond the scope of this work. The prospects of an integrated optical Young interferometer device will be discussed and new aspects of a multichannel sensor will be presented. This chapter concludes with the outline of the thesis.

1.1 Immunosensors

A sensor is a device that converts the value of a non-electrical parameter, e.g. a chemical, thermal, or mechanical one, into an electrical signal. For example in a chemo-optical sensor, changes in chemical domain are converted into changes of optical parameters that can be converted into electrical signals using various readout principles.

There is a high need for bio-chemical sensors [1], which can be used e.g. for determination of an analyte concentration in a given sample solution. The use of these sensors in different areas of production and monitoring, as well as in the field of research, is becoming an increasingly interesting issue nowadays. In areas such as food analysis, health care, environmental monitoring, biotechnology and bioprocess control, life science research, etc., it is necessary to monitor different processes in a fast, accurate, and reliable way. In the food and beverage industry, these sensors are required to measure the concentration of unwanted components, such as pesticides in milk or in drinking water, hormones in meat products, etc. In the field of health care, one needs to monitor for instance the presence of a given virus in a blood sample, e.g. Hepatitis B and C, HIV, the newly-discovered SARS virus, etc. In the environmental monitoring, it is necessary to monitor the presence of contaminating substances, such as detergents and/or other chemicals in the urban areas; care should be also given to the industrial areas in order to prevent contamination from different substances used for various production processes in chemical and pharmaceutical industry, etc. In biotechnology and bioprocess control, such sensors can be involved in monitoring of different processing steps that aim at the production of various components, etc. Life science research uses sensor technology to study biomolecular interactions, e.g. in cancer research, immunology, neuroscience, etc.

The chemical transduction layer, or the chemical interface, is an important component of the chemical sensors that selectively reads the information from the chemical domain. That type of sensor that uses a biological receptor interface is called a biosensor. In that case the bio-interface layer performs the chemical selectivity, as a preliminary step for measuring the component of interest in a given sample solution. When an antibody or an antigen layer is used as a transducer layer in a biosensor, that type of biosensor is called an immunosensor. The interaction between an antibody and its specific partner, the antigen, is very specific, which results from non-covalent binding forces, such as electrostatic, hydrophobic, van der Waals forces, etc., involved in the antibody-antigen complex

3

formation [2]. The antibody consists of two Fab fragments, being the regions where the antigen binds, and one Fc fragment, which is almost the same for all antibodies. The advantage of immunosensors is that using modern biotechnology, antibodies can be generated against almost any type of analyte molecule.

In order to use these chemical sensors for various real life applications, as mentioned above, they should fulfill various requirements such as being sensitive, selective, accurate, stable, robust, easy-to-use, as integrated as possible, multipurpose, reusable, cheap (both in production and operation), fast (preferably on-line), need a low amount of sample, etc. Combination of as many of these properties as possible in a single device may result in an advanced sensing system.

One single sensor out of the various types of chemical sensors that are realized so far based on different principles and using various technologies cannot satisfy the entire spectrum of requirements as described above yet. On one hand, there is a demand for better performance and sensing systems that are more reliable (market pull), and on the other hand, there is an ongoing development of new sensing principles as well as improvement of various sensor devices already realized (science push).

Being attracted to the idea of a sensor system that can involve as many of these properties as possible and motivated by new developed technologies, the work that will be described in this thesis will be focused on the development of highly sensitive and multifunctional chemical and immuno sensing systems.

1.2   Optical immunosensors

Different types of immunosensors have been developed so far. These sensors differ in various aspects such as working principle, complexity of the equipments needed to implement a given principle, use of labeling, operating conditions, monitoring time, etc. In addition, features such as sensitivity, resolution, accuracy, stability, selectivity, robustness, multipurpose, reusability, etc., are some other important aspects that differ from one type of sensor to another. All these parameters combined with each other give an indication about sensing techniques that can be easily developed and effectively used for a given type of application.

In this project, we will focus on development of integrated optical (IO) based chemical and immuno sensors. In the past several types of IO sensors have been developed. Here we can mention the waveguide-based sensors such as interferometric sensors [3-7], grating couplers [8], resonant mirrors [9], integrated

4

microcavity based sensor [10]; surface plasmon resonance (SPR)-based sensor [11], and reflectance-based sensors like reflectance interference device [12], etc.

One of the main advantages of the optical-based sensors is their high resolution. Integrated optical sensors [13], especially the interferometric ones that have been developed in recent years, such as the Mach-Zehnder interferometer (MZI) [14] and the Young interferometer (YI) [15-18], show an extremely high refractive index resolution, being in the range of 10^{-7}-10^{-8} [14, 18], which is equivalent to detection of a protein mass coverage of ~ 30 fg/mm^2.

Furthermore, the IO readout systems are robust and small, allowing for a miniaturization where many elements of the device can be integrated in a single chip, which on the other hand occupies a relatively small area. These features offer the prospect for development of multisensing systems. Furthermore, this implies an increase of the analysis throughput, a reduction in the consumption of biomaterials, and cost reduction.

Moreover, the optical-based sensors are label free sensing techniques, which require less complex sample preparation, do not need special laboratories and skilled personnel, and costs of a test are lower. In addition, usually a simpler and faster signal analysis can be performed.

Considering all different aspects discussed above, we have chosen for the development of an IO interference-based immunosensing system, which will be discussed in more detail in the next section.

1.3   Interferometric IO sensors

Integrated optical waveguide-based sensors can monitor the antibody-antigen interactions by making use of the evanescent field sensitivity of guided modes propagating through the waveguide structure of the sensor. The evanescent field sensing has the advantage that it matches well with the availability of many chemical interfaces. Figure 1.1 shows a scheme of a binding event taking place at the core-cover interface of a three-layer waveguide structure. Here, the core-cover interface of the optical waveguide structure is coated with a chemo-optical transducer receptor layer, which can selectively bind to a certain type of analyte molecules present in the cover medium.

When the binding of an analyte occurs, the substitution of solvent by the analyte molecules will result in an increase of the refractive index n at the core-cover interface. Therefore, the effective refractive index N_{eff} of a guided mode, which probes the core-cover interface during the propagation through the waveguide,

5

will be changed within the interaction length, and this will result into a phase change of the mode at the exit of the interaction region.
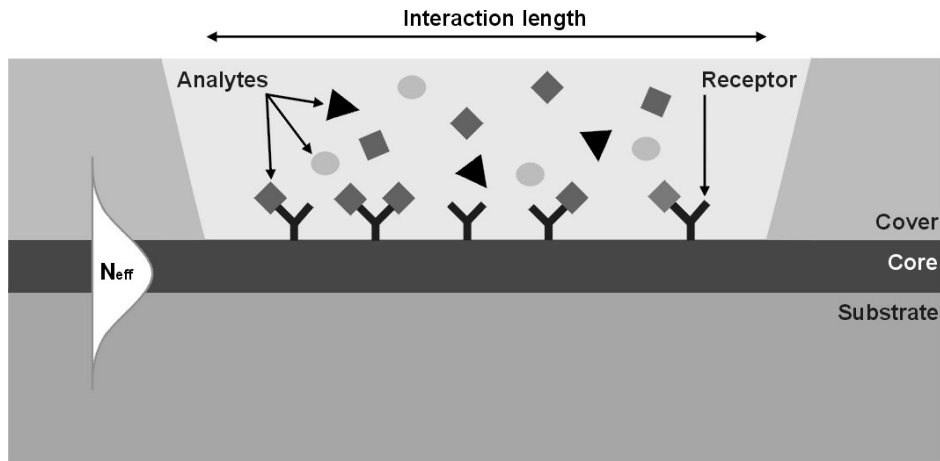
Figure 1.1 *Schematic presentation of a binding event between analyte and receptor molecules occurring at the core-cover interface of a three-layer waveguide structure within the evanescent region of a guided mode. N_{eff} indicates the effective refractive index of the guided mode.*

Here, two different situations can be distinguished: in the first situation, the evanescent region is completely occupied with one sensitive material, being e.g. a solution of one given analyte (homogeneous sensing). In that case, the refractive index change counts for the analyte concentration C in the solution. In the second situation, a chemo-optical transduction layer is immobilized at the core-cover interface of the waveguide structure, e.g. in an immunoreaction, this can be an antibody layer (surface sensing).

The phase change that results from a binding event can be measured with a high sensitivity by using an interferometric sensor, e.g. the MZI [14], the YI [16, 18], or differential interferometer [19], due to relatively long interaction length of these devices (up to several centimeters). In the group of interferometric devices, those that have a reference branch to compensate for common mode effects, such as temperature changes, pressure, fluctuations of light source power, etc., are more preferable such as the MZI and the YI.

Both the MZI and the YI based two-channel devices can be expanded to a multichannel one. In this thesis, the research is focused on multiplexing only the YI type of sensor. For this decision, we used the following arguments. Firstly, for an IO YI no optical phase modulation is required to achieve a high sensitivity as in the case of a phase-modulated MZI [14], resulting in a simpler chip design.

Secondly, the YI offers the prospect of an array configuration with relatively small chip area. Thirdly, no extra hardware is required for development of a multichannel device based on a YI, apart from the chip design, as it will be shown later in this thesis.

In Figure 1.2, a schematic layout of a two-channel IO YI is shown. Light is coupled into an integrated optical channel waveguide and split by an Y-junction to two output parallel branches positioned at a certain distance from each other, as shown in Figure 1.2. An interference pattern is generated as a result of the overlap of both outgoing divergent beams. The interference pattern is recorded by a CCD camera, which is placed at a given distance from the endface of the integrated chip. A sensing window is realized on the top of the core layer of the measuring channel where the sampling liquids to be analyzed are applied. When a binding event takes place on the sensing window of the measuring channel, as shown schematically in Figure 1.2, a phase change between reference and measuring branches will result and the interference pattern will be shifted with respect to the camera surface. By measuring the spatial shift of the interference pattern, the phase change can be calculated, and furthermore, the refractive index change occurring on the sensing window of the measuring arm can be determined.
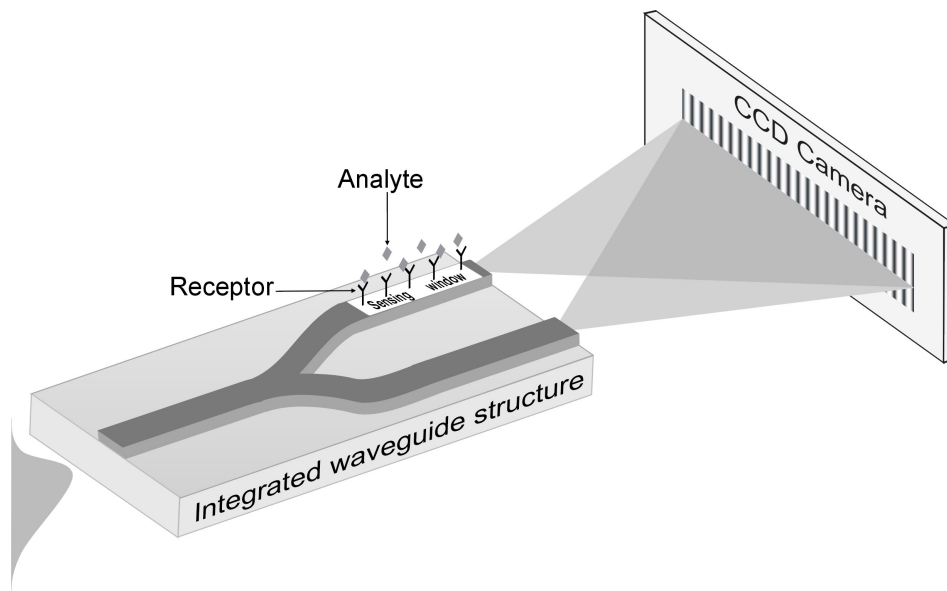

Figure 1.2 *Schematic layout of a two-channel integrated optical Young interferometer sensor.*

7

1.4   Goal of this thesis

A common feature of the interferometric sensors developed so far is that they contain one sensor only [3-5, 14-19]. This enables the monitoring of a single analyte at a time. Concerning applications where many analytes have to be determined simultaneously and where a large sample throughput is important, e.g. in medical diagnostics (proteomics), it is required to develop multichannel sensors, as it has been done e.g. for SPR-based sensors [20-21].

A multichannel interferometer sensor could enable monitoring of multiple binding events simultaneously and independently from each other by immobilizing different receptor molecules to different channels. In addition, by using such a device, a binding curve of an analyte to a specific receptor layer can be achieved by applying different concentrations of the analyte molecules to different channels. Finally, one or some of the channels can be used to determine the non-specific binding.

Nevertheless, a two-channel IO YI sensor needs to be realized first for exploring the possibilities that offer a YI-based system, as a preliminary step towards realization of a multichannel sensor.

The interferometric sensors have been mainly used for detection of proteins, e.g. binding of antigen molecules to a specific antibody layer that is immobilized on the sensor surface [16, 18, 22-25]. It is scientifically interesting and relevant from the application point of view to explore the use of these sensors not only for monitoring proteins, but also for other types of analytes, e.g. viruses, which so far have been detected with time-consuming methods [26]. The principle of the sensor allows that given the proper receptor, relevant viruses such as HIV, SARS, Hepatitis B and C may be possible to be detected.

Another aspect that requires attention for the interferometric sensors is the flow system. Usually, bulky cuvette-based systems are used for these sensors, resulting in a long-time response and requiring relatively large sample volumes [14-18]. It is desirable in that case to implement microfluidics [27], which might offer a number of advantages, such as a short response time and a better discrimination of bulk effects in an immunoreaction, offering in that way the prospect of using the kinetics of the immunoreaction.

Using such sensitive sensors it is possible to measure e.g. very low concentrations of an analyte in solution. However, long-term resolution of these sensors is limited by the drift, which may be caused e.g. by temperature differences between reference and measuring channels, and it may deteriorate up to one order of magnitude [14-18] compared to the short-term resolution. It is

therefore imperative implementation of any correction method to suppress the temperature effects and improve the performance of these sensors.

To this end, it is the general aim of this project to develop highly sensitive and multichannel IO chemical and immuno sensors of the YI type, where microfluidics can be integrated and drift correction method may be applied, and which can be effectively used for various applications in areas such as medical screening (virus detection), food analysis, environmental monitoring, etc.

1.5   Outline of the thesis

In this thesis, realization and characterization of highly sensitive multichannel integrated optical Young interferometer sensing systems for sensing applications will be presented.

In Chapter 2, a full theoretical description of a multichannel YI based sensor will be presented. The working principle of such a device will be given followed by application of different schemes for reduction of the phase error and cross talk caused by the Fast Fourier Transform algorithm. To this end, a discussion will be made and some conclusions will be given based on the analysis presented.

In Chapter 3, the design and realization of an IO YI sensing system will be described. Here, analysis of sensitivity and disturbing factors will lead to the functional design and implementation of the different subfunctions. At the end, the final design of the sensing system and manufacturing of the IO channel waveguide structures based in SiON technology will be described.

Experimental characterization of the two-channel and four-channel YI sensor devices will be presented in Chapter 4. Here, different schemes for reduction of the phase error and cross-talk will be experimentally implemented. To this end, the performance of these devices will be discussed.

Chapter 5 describes the use of the YI sensor for virus detection, as an important application in the medical screening. Multichannel detection of virus particles and proteins will be presented, as well as measurement of different analyte concentrations. Based on the results achieved, a discussion concerning the detection of viruses and performance of the YI immunosensor will be made.

A new method to improve the long-term stability in the multichannel YI sensor will be demonstrated in Chapter 6. Here, the phase information obtained for different pairs of channels will be used to correct the drift due to temperature differences between measuring and reference channels, drift in the alignment of the set-up, etc. The drift-correction method will be experimentally tested by applying it for sensing applications.

In Chapter 7, the development of a microfluidic sensing system obtained by bonding a microfluidic system to an IO four-channel YI chip will be presented.

9

Such a system will be experimentally tested and it will be shown that in an immunoreaction the bulk effects can be well separated from the layer formation, resulting in results that are more accurate. At the end, the prospects of such a system will be given.

A theoretical approach, which aims at the compensation of the temperature changes in the interference-based sensors by using multiple wavelengths, will be described in Chapter 8. New analytical expressions, which describe dependency of the refractive index of a given medium from its temperature and concentration will be derived and compared to available results that are experimentally achieved.

In Chapter 9, some conclusions that concern the development of the multichannel IO YI sensor and its use for different applications will be presented. Here, a comparison between the multichannel YI sensor and other interferometric sensors, as well as other techniques, will be made. This Chapter concludes with an outlook concerning further improvement of the performance of the IO YI sensing system.

Finally, some new approaches for future development of the multichannel interference-based sensors will be discussed in Chapter 10. Here, attention will be paid to the improvement of the resolution and multichannel operation of these sensors.

References

[1]   C. Nylander, Chemical and biological sensors, J. Phys. E. 18, 736-750 (1985).

[2]   M.P. Byfield and R.A. Abuknesha, Biochemical aspects of biosensors, Biosensors and Bioelectronics 9, 373-400 (1995).

[3]   R.G. Heideman, R.P.H. Kooyman, and J. Greve, Performance of a highly optical waveguide Mach-Zehnder interferometer immunosensor, Sensors and Actuators B 10, 209-217 (1993).

[4]   E.F. Schipper, A.M. Brugman, C. Dominguez, L.M. Lechuga, R.P.H. Kooyman, and J. Greve, The realization of an integrated Mach-Zehnder waveguide immunosensor in silicon technology, Sensors and Actuators B 40, 147-153 (1997).

[5]   I.S. Duport, P. Benech, and R. Rimet, New integrated-optics interferometer in planar technology, Applied Optics 33, 5954–5958 (1994).

[6]   C. Stamm and W. Lukosz, Integrated optical difference interferometer as immunosensor, Sensors and Actuators B 31, 266-271 (1996).

[7]   E.R. Cox and B.E. Jones, Fiber optic color sensors based on Fabry-Perot interferometry, Proceedings of First international conference on optical fiber sensors, London, 1993.

[8]   D. Clerc and W. Lukosz, Integrated optical grating coupler as biochemical sensor, Sensors and Actuators B 18-19, 581-586 (1994).

[9]   R. Cuch, J.M. Cronin, W.J. Stewart, C.H. Maule, J. Molloy, and N.J. Goddard, The resonant mirror: a novel optical biosensor for direct sensing of biomolecular interactions part 1: Principle of operation and associated instrumentation, Biosensors and Bioelectronics 8, 347-353 (1993).

[10] E. Krioukov, D.J.W. Klunder, A. Driessen, J. Greve, and C. Otto, A new type of sensor based on an integrated optical microcavity, Opt. Lett. 27, 512-514 (2002).

[11] R.P.H. Kooyman, A.T.M Lenferink, R.G. Eenink, and J. Greve, Vibrating mirror surface plasmon resonance immunosensors, Anal. Chemistry 63, 83-85 (1991).

[12] A. Brecht, J. Piehler, G. Lang and G. Gauglitz, A direct optical immunosensor for atrazine detection, Analytica Chimica Acta 311, 289-299 (1995).

[13] P.V. Lambeck, Integrated opto-chemical sensors, Sensors and Actuators B 8, 103-116 (1992).

[14] R.G. Heideman and P.V. Lambeck, Remote opto-chemical sensing with extreme sensitivity: design, fabrication and performance of a pigtailed integrated optical phase-modulated Mach-Zehnder interferometer system, Sensors and Actuators B 61, 100-127 (1999).

11

[15] A. Brandenburg, Differential refractometry by an integrated-optical Young interferometer, Sensors and Actuators B 38-39, 266-271 (1997).

[16] A. Bradenburg, R. Krauter, C. Kuenzel, M. Stefan, and H. Schulte, Interferometric sensor for detection of surface-bound bioreactions, Applied Optics 39, 6396-6405 (2000).

[17] G.H. Cross, Y. Ren, and N.J. Freeman, Young's fringes from vertically integrated slab waveguides: Applications to humidity sensing, Journal of Applied Physics 86, 6483-6488 (1999).

[18] G.H. Cross, A.A. Reeves, S. Brand, J.F. Popplewell, L.L. Peel, M.J. Swann, and N.J. Freeman, A new quantitative optical sensor for protein characterization, Biosensors and Bioelectronics 19, 383-390 (2003).

[19] T. Koster and P.V. Lambeck, Fully integrated polarimeter, Sensors and Actuators B 82, 213-226 (2002).

[20] C.E.H. Berger, T.A.M. Beumer, R.P.H. Kooyman, and J. Greve, Surface plasmon resonance multisensing, Anal. Chem. 70, 703-706 (1998).

[21] BIACORE, Pharmacia Biosensor AB, Uppsala, Sweden (www.biacore.com).

[22] R.G. Heideman, Optical waveguide based evanescent field immunosensors, Ph.D. Thesis, University of Twente, The Netherlands, 1993.

[23] R.G. Heideman, R.P.H. Kooyman, and J. Greve, Immunoreactivity of adsorbed anti human chorionic gonadotropin studied with an optical waveguide interferometric sensor, Biosensors and Bioelectronics 9, 33-43 (1994).

[24] E.F. Schipper, A.J.H. Bergevoet, R.P.H. Kooyman, and J. Greve, New detection method for Atrazine pesticides with the optical waveguide Mach-Zehnder immunosensor, Analytica Chimica Acta 341, 171-176 (1997).

[25] E.F. Schipper, Waveguide immunosensing of small molecules, Ph.D. Thesis, University of Twente, The Netherlands, 1997.

[26] A.C. Minson, Alphaherpesviruses: herpes simplex and varicella zoster virus infections. In *Topley and Wilson's microbiology and microbial infenctions,* Vol 1, Edn. 9 (eds Mahy, B. & Collier, L.) 325-339 (Arnold, London; 1998).

[27] J.M. Ramsey and A. van den Berg, *Micro Total Analysis Systems* (Kluwer, Dordrecht, 2001).

CHAPTER TWO

THEORETICAL ANALYSIS

A theoretical description of the multichannel YI sensor will be given and the working principle of such a device will be presented. Furthermore, an analysis of the phase error and cross-talk observed in the multichannel YI sensor and different methods to reduce these errors, leading to more accurate measurements, will be discussed. To this end, a discussion of the results achieved in the presented analysis will be given. [1]

---

[1] Part of the results of this chapter has been published as:

a. A. Ymeti, J.S. Kanger, R. Wijn, P.V. Lambeck, and J. Greve, Development of a multichannel integrated interferometer immunosensor, Sensors and Actuators B 83, 1-7 (2002).

b. A. Ymeti, J.S. Kanger, J. Greve, P.V. Lambeck, R. Wijn, and R.G. Heideman, Realization of a multichannel integrated Young interferometer chemical sensor, Applied Optics 42, 5649-5660 (2003).

2.1   Introduction

In a three-layer waveguide structure, guiding of the light is performed due to appropriate refractive index contrast between the core layer and the cladding. In Figure 2.1, such a structure is presented, consisting of a substrate, core, and cover layer, which have respectively a refractive index of n_S, n_F, and n_C. A higher refractive index of the core layer allows total internal reflection of the light at the core-cladding interface, as shown schematically in Figure 2.1, in that way making possible propagation of the light through the slab waveguide.
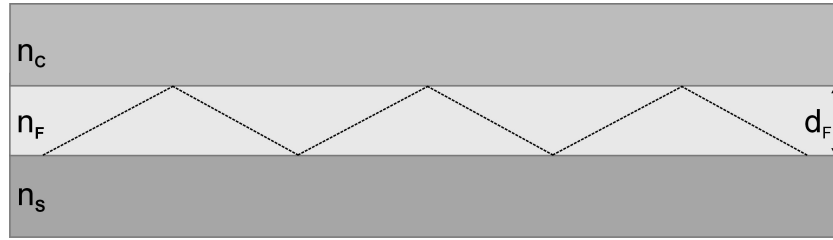
Figure 2.1 *Schematic layout of the total internal reflection in a three-layer waveguide structure. n_i (i = C, F, S) indicates the refractive index of layer i of the waveguide structure, $n_F > n_{C,S}$; d_F is the thickness of the core layer.*

In conditions of total internal reflection, guided modes are obtained due to the constructive interference between the light rays propagating through the waveguide [1]

$$\frac{2\pi}{\lambda} 2 d_F n_F \cos\theta - \Phi_C - \Phi_S = n \cdot 2\pi \qquad (2.1)$$

where λ is the vacuum wavelength of the guided light, d_F is the thickness of the core layer, θ is the angle of incidence at the core-cladding boundary, Φ_C and Φ_S are the phase changes arising from the reflection at the core-cover and core-substrate boundary, respectively, and n is the order of the guided modes.

In a channel waveguide structure, schematically shown in Figure 2.2, the light is confined not only in the transversal direction, but also in the lateral one. This confinement is caused by the lateral contrast of the (effective) refractive indices between the channel region, N_{eff-C}, and the slab one, N_{eff-S}, i.e. $N_{eff-C} > N_{eff-S}$ that can be due to presence of a ridge in the core section, where the effective

refractive index is defined as $N_{eff} = n_F \cdot \sin\theta$. Generally, at a given channel structure the parameters expressing quantitatively the propagation of guided light beams (modes) can be calculated using Maxwell theory based software.

Cross-section

3D-view

Top-view

N_{eff-S} N_{eff-C} N_{eff-S}
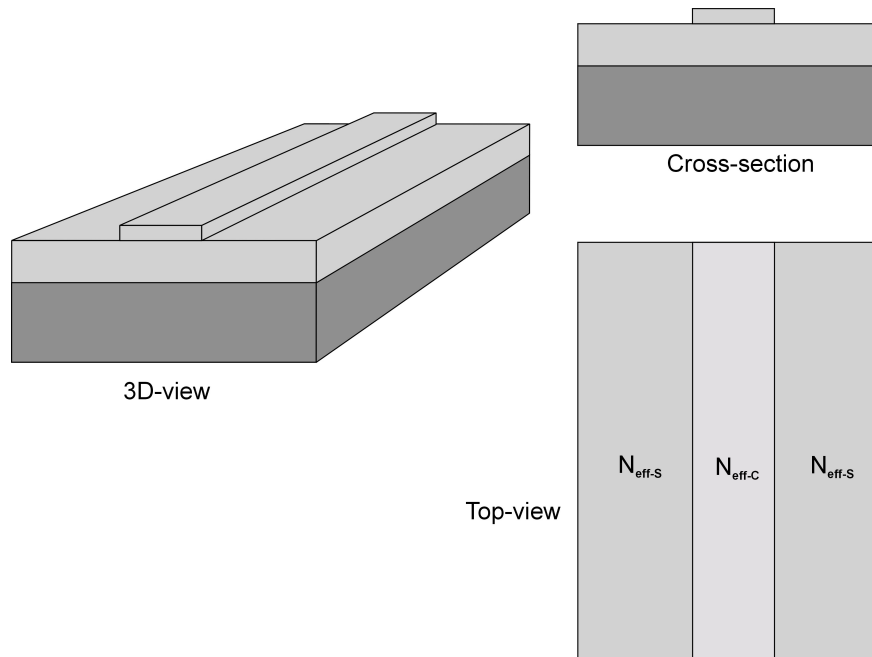
Figure 2.2 *Schematic 3D-view, cross-section and top-view of a channel waveguide structure; N_{eff-C} and N_{eff-S} indicate the effective refractive indices of the channel and slab region, respectively.*

Channel waveguide structures can be used to guide the light not only along a straight section, but also in a bent one, e.g. in an S-bend, etc.

(A)   (B)   (C)
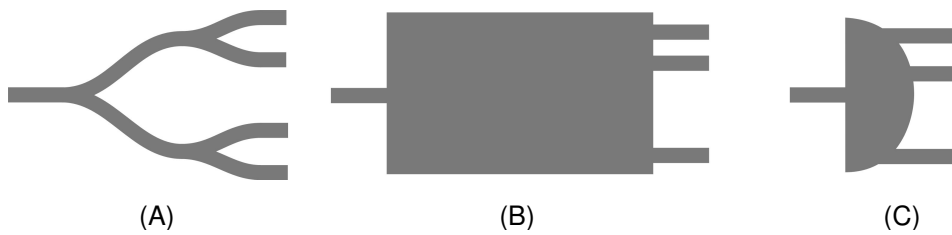
Figure 2.3 *Schematic layout of a multiple Y-junction (A), a 1 x N MMI coupler (B) and a 1 x N star coupler (C).*

Furthermore, using channel waveguides, the light coupled into an input channel can be divided to several output channels, e.g. in a multiple Y-junction, Multimode interference (MMI) coupler, star coupler, etc. (see Figure 2.3).

For the theoretical description of the multichannel YI principle, the choice of the splitter type is not important and will be treated in detail in chapter 3. Here, a multichannel YI based on Y-junctions is shown.

2.2 Multichannel integrated optical YI

The principle of a multichannel YI is similar to that of a two-channel YI [2]. As will be shown in this section, in the multichannel YI all pairs of parallel output channels will act as a two-channel YI, each with a unique distance between its two arms.
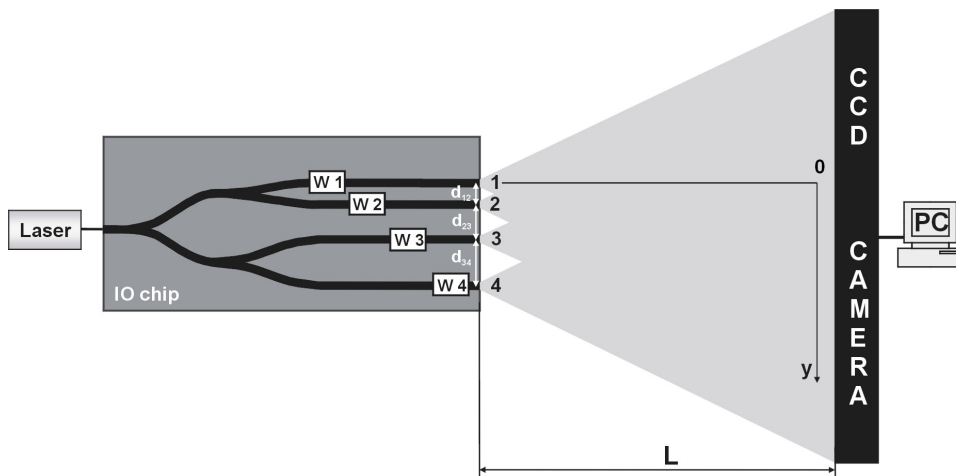
Figure 2.4 *Layout of the four-channel IO YI (not on scale); W i indicates the sensing window on channel i, d_{ij} is the distance between channels i and j, L indicates the distance of the CCD camera from the chip endface.*

2.2.1 Theoretical description

In a multichannel YI, monochromatic laser light with a vacuum wavelength λ is coupled into an input channel waveguide and split to *N* output parallel channels, as shown in Figure 2.4 (in this figure a network of 3 Y-junctions is used to split the light to 4 output channels).

17

The output divergent beams will overlap with each other and the final interference pattern will be a superposition of individual interference patterns, each of them representing the overlap of the divergent beams of a specific channel pair. The interference pattern is recorded by a CCD camera, which is placed at a distance L from the chip endface. The irradiance distribution of the sum interference pattern at the input face of the camera can be derived to be [3]

$$I(y) \approx \sum_{i=1}^{N} I_i + 2 \sum_{i,j=1; i<j}^{N} \left(I_i I_j\right)^{\frac{1}{2}} cos\left(\Delta\Phi_{ij}(y) - \Delta\phi_{ij}\right) \qquad (2.2)$$

where I_i and I_j are the output power from channels i and j, respectively. A channel output is approximated as a point source. Eq. (2.2) is only valid if L is chosen such that the output divergent beams fully overlap at the CCD camera. In Eq. (2.2), $\Delta\Phi_{ij}(y)$ is the phase difference between the interfering beams coupled out from channels i and j as a result of their different optical path length at the interfering position y on the CCD camera. The phase change $\Delta\phi_{ij}$ represents the sum of the initial phase difference at the channel outputs in absence of the measurand, $\Delta\phi_{ij}^{0}$, and the phase change $\Delta\varphi_{ij} = \Delta\varphi_i - \Delta\varphi_j$ induced by refractive index changes Δn_i and Δn_j in channels i and j, respectively, i.e. $\Delta\phi_{ij} = \Delta\phi_{ij}^{0} + \Delta\varphi_{ij}$. The phase difference $\Delta\Phi_{ij}(y)$ can be derived to be [3]

$$\Delta\Phi_{ij}(y) = \frac{2\pi}{\lambda} \frac{d_{ij}}{L} y - \frac{2\pi}{\lambda} \frac{d_{ij}}{L}\left(d_{1i} + \frac{1}{2}d_{ij}\right) \qquad (2.3)$$

provided that the distance between channels i and j $d_{ij} << L$ for all i, j values, a condition that is well satisfied in our case. Hence, an individual interference pattern shows a spatial frequency k_{ij} given as

$$k_{ij} = \frac{1}{\lambda} \frac{d_{ij}}{L} \qquad (2.4)$$

The second term in Eq. (2.3) corrects for the shift of the center between two channels i and j with respect to the origin of the y-axis along the CCD camera (see Figure 2.4).

The refractive index changes in channels i and j can be induced due to binding between analyte and receptor molecules in the sensing window of each channel, see Figure 1.1. As a result, the effective refractive index of guided modes in channels i and j (N_{eff-i} and N_{eff-j} respectively) will be changed, and consequently the phase changes $\Delta\varphi_i$ and $\Delta\varphi_j$ will result. The phase change $\Delta\varphi_{ij}$ can then be derived as

18

$$\Delta\varphi_{ij} = \frac{2\pi}{\lambda}\, l\left(\frac{\partial N_{eff-i}}{\partial n_i}\Delta n_i - \frac{\partial N_{eff-j}}{\partial n_j}\Delta n_j\right) \qquad (2.5)$$

where l is the length of the sensing window realized on top of each output channel, $\partial N_{eff-i}/\partial n_i$ and $\partial N_{eff-j}/\partial n_j$ indicate the sensitivity coefficient of N_{eff} with respect to the change of the refractive index in channels i and j respectively, which can be calculated for a given wavelength and waveguide structure [4]. In case of identical channels, i.e. $\partial N_{eff-i}/\partial n_i = \partial N_{eff-j}/\partial n_j \equiv \partial N_{eff}/\partial n$, Eq. (2.5) can be written as

$$\Delta\varphi_{ij} = \frac{2\pi}{\lambda}\, l\,\frac{\partial N_{eff}}{\partial n}\Delta n_{ij} \qquad (2.6)$$

where $\Delta n_{ij} = \Delta n_i - \Delta n_j$.
The resulting refractive index change between channels i and j can cause a spatial shift of Δy_{ij} of the individual interference pattern for this channel pair along the camera surface. This shift can be calculated based on Eq. (2.3) and (2.6) as

$$\Delta n_{ij} = \frac{d_{ij}}{lL}\left(\frac{\partial N_{eff}}{\partial n}\right)^{-1}\Delta y_{ij} \qquad (2.7)$$

If one chooses channel i, $i = 1, 2, …, N$-1, to be the measuring channels, and channel N as a reference channel, where N is the total number of the channels, the refractive index changes Δn_{iN} may be determined using Eq. (2.7) by measuring the spatial shifts Δy_{iN}.
If $N = 2$, there will be one measuring channel, and this is the case of a two-channel YI device [2]. In case of $N = 4$, the refractive index changes Δn_{14}, Δn_{24}, and Δn_{34} can be calculated based on the measurement of the spatial shifts Δy_{14}, Δy_{24}, and Δy_{34} [5]. Condition for that is that these spatial shifts have to be measured simultaneously and independently from each other requiring a proper design of the four-channel YI device, which will be described in the next section.

2.2.2 Working principle

The output parallel channels of the multichannel device will be positioned at different distances d_{ij} from each other in such a way that channels of each pair are separated by a unique distance, as shown in Figure 2.4. In other words, $d_{12} \neq d_{23} \neq … \neq d_{ij}$, where d_{ij} denotes the distance between channel i and j, and $i \neq j = 1, 2, …, N$, where N is the total number of the channels.
In this way all spatial frequencies k_{ij}, each of them corresponding to the specific distance d_{ij} as shown from relation (2.4), are different, which makes it possible to

19

well-separate different peaks in the amplitude of the Fourier-transformed interference pattern and select the spatial frequency for each peak. As a result, the phase change $\Delta\phi_{ij}$ between both channels of one pair, corresponding to the selected spatial frequency k_{ij}, can be monitored independently from the other channel pairs at the phase of the Fourier-transformed interference pattern.

A more detailed theoretical analysis of the working principle of the multichannel YI is given for a four-channel device ($N = 4$). In Figure 2.4, the four-channel IO YI is schematically shown. The distances between the channels have been chosen such that $d_{12} \neq d_{23} \neq d_{34} \neq d_{13} \neq d_{24} \neq d_{14}$. There are six possible different channel pairs corresponding to six different distances of $d_{12} = 60$ μm, $d_{23} = 80$ μm, $d_{34} = 100$ μm, $d_{13} = 140$ μm, $d_{24} = 180$ μm, and $d_{14} = 240$ μm. These distances match the sensor structure 1 described in chapter 3. The final interference pattern will thus be a superposition of six interference patterns. The calculated interference pattern for the four-channel YI is shown in Figure 2.5.A. The amplitude (lower graph) and the phase (upper graph) of the Fourier-transformed interference pattern are presented in Figure 2.5.B.

(A)   (B)
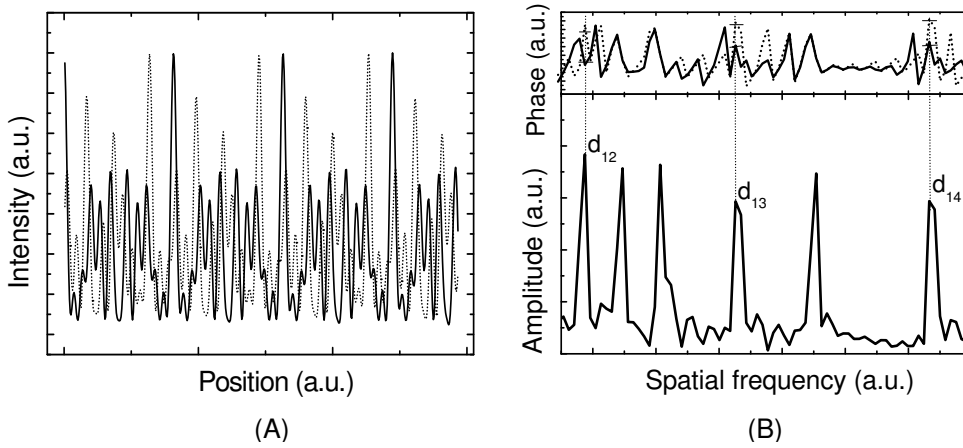
Figure 2.5 *(A) The interference pattern in the four-channel YI calculated for L = 6 cm, d_{12} = 60 μm, d_{23} = 80 μm, d_{34} = 100 μm (solid line). The dotted line represents the interference pattern calculated when an extra phase shift is introduced on channel 1. (B) Amplitude (lower graph) and the phase (upper graph) of the Fourier-transformed interference patterns shown in A (solid and dotted line respectively).*

As one might expect, there are six different peaks in the amplitude of the Fourier-transformed interference pattern located at six different spatial frequencies k_{ij}, each of them corresponding to the interference pattern obtained as a result of overlap of the channels that are separated by the specific distance d_{ij}. Looking at

the selected spatial frequencies at the phase part of the Fourier-transformed interference pattern, the phase of each "two-channel sensor" can be monitored simultaneously and independently from each other. The difference between distances d_{ij} should be such that they allow a good separation of the six different peaks.

If an extra phase change will result in one of the channels, e.g. in channel 1, the same phase change is expected between channels of those pairs that involve channel 1. In Figure 2.5.A, the dotted line represents the calculated interference pattern when an extra phase change is introduced in channel 1. Calculating the Fast Fourier Transform (FFT) of this interference pattern results in having six different peaks in the amplitude of the Fourier-transformed interference pattern, located at the same spatial frequencies when no extra phase shift is added in one of the channels. In the phase part of the Fourier Transform, one can clearly observe a phase change corresponding to those channel pairs where channel 1 is involved, see dotted line in Figure 2.5.B.

If channels 1, 2, and 3 are chosen as measuring channels and channel 4 as a reference channel, it will be possible in principle to monitor independently and simultaneously three different binding events, each of them taking place in one of the measuring channels.

2.3   Theoretical analysis of the phase error and cross-talk

In section 2.2.2, we have introduced the basic working scheme of the multichannel YI. In principle it is concluded that when a given phase change is introduced in one of the channels, the same phase change occurs for those channel pairs that involve that channel.

Starting from this principle, we have performed a more detailed calculation regarding the accuracy of the extracted phase change for each pair of channels when a given phase change is introduced at the channels of the device. For these calculations, we have considered the experimental parameters in order to approach as good as possible the real experimental situation. A more detailed analysis of these calculations is described in Appendix A.

According to these calculations, it results that when a given phase change is introduced in one of the channels of the four-channel YI device, there is a deviation between the resulting phase changes and the expected ones. Concretely, if a phase change of 0.5 x 2π is introduced in channel 1, the phase changes between channel 1 and 2, 1 and 3, and 1 and 4 differ from the expected one with a maximum of ~ 0.05 x 2π. In addition, a phase change is observed between channels 2 and 3, 3 and 4, and 2 and 4, being ~ 0.035 x 2π at maximum. For the expected phase changes, the difference is noted as phase error (PE),

21

whereas the deviation where no phase change is expected is noted as cross-talk (CT).

The origin of these deviations can be explained based on the FFT algorithm [6-7], which is part of the signal analysis. In the four-channel YI, the interference pattern is recorded with a CCD camera, which has a finite number of pixels that are equally spaced from each other. According to the Discrete Fourier Transform theory [8-9], the outcome of the Fourier transformation will be a discrete spectrum of spatial frequencies, which are determined by the total number of camera pixels and the sampling interval. On the other hand, the spatial frequency of the interference pattern between two channels i and j depends on their distance d_{ij}, the wavelength used, and the distance between the CCD camera and chip endface, L, see Eq. (2.4).

(A)	(B)
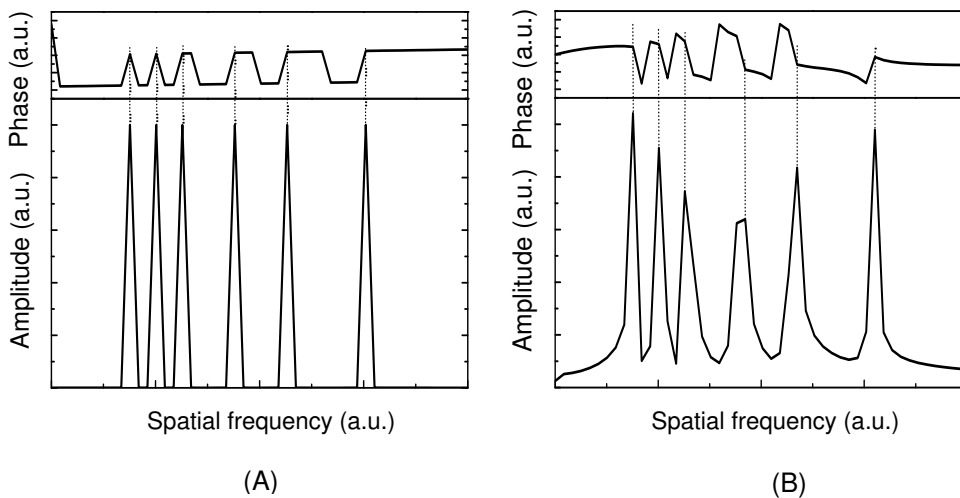
Figure 2.6 *The amplitude and the phase of the FFT of the interference pattern in the four-channel YI calculated (A) when a matching of spatial frequencies between individual interference patterns and those of the CCD camera is achieved, (B) in case of a mismatching condition.*

For a particular set of these parameter values, the spatial frequency of a given interference pattern can be either equal to one of the spatial frequencies determined from the CCD camera, or different from them. The distance of the CCD camera from the chip endface where all spatial frequencies of individual interference patterns match with one of the spatial frequencies determined from the CCD camera is noted as a 'matching' distance. It is known that if the frequency of the original signal matches a spatial frequency of the CCD camera exactly, in other words, if an integer number of fringes is acquired, only the main

lobe of the spectrum is present. In that case, the frequency of the original signal can be read very precisely, and so can the phase of the signal that is extracted at that particular frequency. On the other hand, if this condition is not satisfied, the frequency of the signal will not be positioned at any of the spatial frequencies of the discrete spectrum, but it will fall between the two closest ones [10]. In that case, the energy from the main peak leaks out to the surrounding frequencies, known as the spectral leakage, resulting in the appearance of side-lobes in the spectrum. For signals containing more than one spatial frequency, side-lobes of one frequency can overlap with main lobes of other frequencies, introducing in such a way an additional error in the positioning of the main lobe. In the four-channel YI, where the original signal contains even six individual interference patterns, resulting in six different spatial frequencies, this effect is significant. In Figure 2.6.A, the calculated amplitude of the Fourier-transformed interference pattern is shown for one of the 'matching' distances: the amplitude of the Fourier-transformed interference pattern has regular and symmetrical peaks that are positioned at well-defined spatial frequencies. In contrast, in case no matching of all spatial frequencies exists, the six different amplitude peaks of the Fourier-transformed sum interference pattern are distorted, as shown in Figure 2.6.B: they have undergone a change in their height and width.
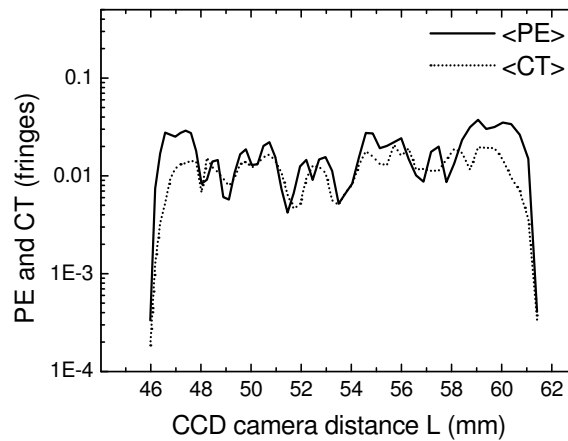
Figure 2.7 *Calculated average PE (<PE> for PE_{1i}, i = 2,3,4) and CT (<CT> for CT_{ij}, i,j ≠ 1) in the four-channel YI, when a phase change of 0.5 x 2π is introduced in channel 1 vs. the CCD camera distance L. Note the two 'matching' positions L = 45.9 and L = 61.4 mm.*

23

Consequently, an error is introduced on extracting the corresponding phase values at the phase part of the Fourier Transform, giving rise to both the PE and CT.

The influence of the chip - CCD camera distance *L* was calculated and is illustrated in Figure 2.7. The PE and CT for a phase change of 0.5 x 2π introduced in channel 1 of the four-channel YI are shown. Details of these calculations are given in Appendix A.

The calculations show that the resulting PE and CT are reduced to a minimum of ~ 0.0005 x 2π at the 'matching' distances of 45.9 and 61.4 mm, while they can grow up to values of ~ 0.05 x 2π at intermediate distances. This result clearly shows that the PE and CT are minimized when a match between the spatial frequencies of the individual interference patterns in the four-channel YI and the spatial frequencies determined by the CCD camera is implemented; it also shows that matching is very critical. Calculations also demonstrate that even when one or some of the spatial frequencies of individual interference patterns, but not all of them, match with one of spatial frequencies determined from the CCD camera, the PE and CT are still considerable.

2.3.1 Calculation of the PE and CT for different phase changes introduced in the channels

In Figure 2.7, the PE and CT are calculated when a phase change of 0.5 x 2π is introduced in channel 1 of the four-channel YI device.
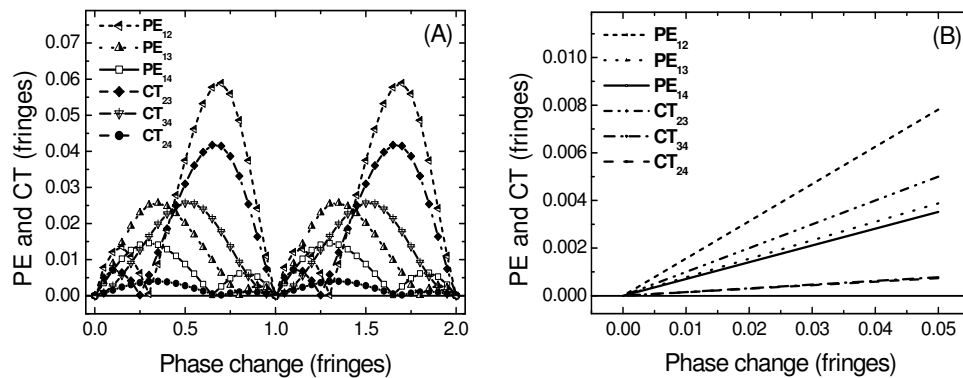

Figure 2.8 *Calculated PE (PE$_{1i}$, i = 2,3,4) and CT (CT$_{ij}$, i,j ≠ 1) in the four-channel YI when the phase change introduced in channel 1 is gradually increased from: (A) 0 to 2 x 2π (B) 0 to 0.05 x 2π.*

We are interested to know how the PE and CT depend on the introduced phase change at the channels for a non-matching condition. For that purpose, we have calculated the PE and CT as a function of the real phase change introduced in channel 1 (see Figure 2.8).

According to this calculation, it results that the PE and CT are minimized to ~ 0 when the phase change introduced at one of the channels is an integer number of fringes, regardless of the spatial frequency matching condition. Moreover, the PE and CT are periodically changing with a period of 2π and they reach a maximum when the introduced phase change at the channels is around $(N + 0.5) \times 2\pi$, where N is an integer number.

2.3.2 Implementation of different techniques to reduce the PE and CT

In previous section, it has been concluded that the algorithm-induced PE and CT are minimal for particular values of L only, these values depending on the channel distance only. So in fact, it should be possible to calculate these particular L-values when all d_{ij} are given. Experimental problems exist in adjusting the real L value to the intended ones. However alternatively, one can try to modify the algorithm to cope with the frequency matching problems.

The different techniques, which can be used for the PE and CT reduction in the four-channel YI, can be divided in two groups. The first group includes techniques that can be implemented experimentally by hardware modification and the second category deals with techniques that can be incorporated in the signal analysis software. In the first group we can mention:

- adjustment of the set-up geometry with the purpose of achieving a spatial frequency matching, e.g. by adjusting the CCD camera distance to one of the 'matching' distances;
- optimization of the distances d_{ij} between output channels of the YI device.

Some of the techniques that can be implemented in the signal analysis software deal with:

- the application of the windowing technique;
- an artificial increase of the spatial frequency resolution;
- a matching of the spatial frequencies.

These error reduction techniques will be described followed by calculations that estimate the PE and CT in the four-channel YI when these techniques are applied.

Reducing the error due to the side-lobe effect can be done by increasing the difference of the distances between output channels. In that way, the spatial frequencies of individual interference patterns will be located at larger distance from each other at the frequency spectrum. Consequently, less overlapping between the side-lobe and the main-lobe responses of different spatial frequency components is expected. In Table 2.1, the PE and CT calculated for three

25

different sets of distances between the channels are presented. The maximum PE and CT can be reduced by a factor of ~ 3 going from the structure with output distances of $d_{12} = 60$ µm, $d_{23} = 80$ µm, and $d_{34} = 100$ µm to the one with output distances of $d_{12} = 100$ µm, $d_{23} = 200$ µm, and $d_{34} = 400$ µm.

Table 2.1 *Calculated maximum PE and CT for three configurations of the four-channel YI in case when no matching of spatial frequencies is present; the CCD camera is positioned at L = 60 mm.*

PE and CT (2π)	Distance between output channels (µm)		
	$d_{12} = 60$ $d_{23} = 80$ $d_{34} = 100$	$d_{12} = 50$ $d_{23} = 100$ $d_{34} = 200$	$d_{12} = 100$ $d_{23} = 200$ $d_{34} = 400$
PE_{12}	0.048	0.038	0.019
PE_{13}	0.044	0.024	0.014
PE_{14}	0.043	0.032	0.017
CT_{23}	0.042	0.016	0.008
CT_{34}	0.025	0.016	0.010
CT_{24}	0.033	0.019	0.010

If spatial frequency matching is not satisfied, the PE and CT can be reduced by implementation of techniques that can reduce side-lobes and spectral leakage effects and improve the accuracy of peak positioning, directly contributing to the accuracy of the extracted phase information. A technique that is very often used is the so-called windowing technique [11-12] where the original signal is multiplied with a window function, e.g. the Hanning window, before the FFT step is applied. According to this calculation, when the Hanning window is used, the PE and CT can be reduced by a factor of ~ 5 compared to the case when no window is used. Increasing the spatial frequency resolution can also reduce the error that is introduced because the frequency of the original signal is lying in between two spatial frequencies of the discrete spectrum. Before the FFT is applied to the original data, one can artificially increase the number of data points, e.g. from 512 to 1024, where the first 512 points are those of the original signal and the rest can be filled with zeros. In that case, the frequency resolution is increased two times compared to the previous situation, with the cost of decreasing the peak amplitudes, which do not effect the peak positioning. The frequency of the original signal will then be lying in between two spatial frequencies that are positioned a two times smaller distance from each other, which obviously reduces the error on selecting the spatial frequency where the phase value is extracted. A remark

should be made about the artificial increase of the number of data points. This number cannot be indefinitely large because the error that will be introduced due to decrease of the peak amplitudes will predominate the effect of spatial frequency increase. Our calculations show that by applying this technique, the maximum PE and CT can be reduced by a factor of ~ 2.

Finally, a technique that aims at removal of the mismatching effect will be described. When the spatial frequency of an individual interference pattern in the four-channel YI matches with one of the spatial frequencies of the discrete spectrum, the interference pattern contains an integer number of fringes. In the case when the recorded interference pattern contains a fractional number of fringes, before the FFT is applied, one can truncate the recorded data by keeping only an integer number of fringes. For that purpose, it is often necessary to initially resample the signal data to a larger number of data points using an interpolation step, such that after the truncation procedure the total number of fringes will be comprised by an integer number of data points. In the four-channel YI truncation has to be done such that an integer number of fringes remains for each individual interference pattern. On the other hand, one should take in consideration the fact that by applying this technique, some errors can be introduced because of the interpolation procedure. The best compromise is to apply this technique using a limited number of data points for the resampling step. Using such a technique, the PE and CT calculated in the four-channel YI can be reduced by a factor of ~ 5.

Combination of different techniques showed that the errors can be further reduced, but the result is not a multiplication of the individual contributions, as it might be expected.

2.4 Discussion and conclusions

A full theoretical analysis of the multichannel YI sensor is presented. The working principle of a two-channel IO YI is elegantly expanded to a multichannel device by positioning the output parallel channels at well-defined distances from each other such that each pair of channels functions as a two-channel YI with a unique distance between its two arms. The first design of the multichannel Young interferometer has four output parallel channels positioned at different distances from each other, such that the phase change between both channels of one pair can be monitored independently from the other channel pairs.

The phase error and cross-talk that result in the four-channel YI can be found on the mismatch between spatial frequencies of individual interference patterns and those determined by the CCD camera. These deviations can be as large as ~ 0.05 x 2π at mismatching conditions, but they can be decreased to ~ 0 when a matching is achieved. For a given wavelength of the light source and chosen distances between the channels, minimization is achieved at particular distances of the CCD camera from the chip endface, noted as 'matching' distances. Calculations have also shown that the PE and CT can be minimized to ~ 0 when the phase changes introduced at the channels are an integer number of fringes.

Different error reduction schemes are proposed, such as adjustment of the CCD camera at one of the 'matching' distances, increase of the difference between channel distances, as well as the Hanning window, increase of the spatial frequency resolution, and resampling and truncation of original data to achieve the spatial frequency matching. These techniques can reduce in mismatch conditions the PE and CT by a factor of ~ 5.

In the four-channel YI configuration, if channel 1, 2, and 3 will be chosen as measuring channels and channel 4 as reference channel, then by using such a device three different binding events can be monitored simultaneously and independently from each other. This implies measuring of three different concentrations of the same analyte to obtain a complete binding curve of this analyte, or monitoring three different analytes by immobilizing specific receptor layers at three different measuring channels. Finally, one or more channels can be used to measure non-specific binding.

Appendix A

A computer program is written for estimation of the PE and CT in the four-channel YI. In that program, the intensity of the sum interference pattern, which is obtained by superposition of six individual interference patterns, is calculated using Eq. (2.2). Each of the individual interference patterns has a spatial frequency equal to one of the spatial frequencies for a pair of channels in the four-channel YI. These spatial frequencies are calculated using Eq. (2.4). We have considered 512 data points for the intensity of the sum interference pattern, equal to the number of the CCD camera pixels that is used for recording the sum interference pattern. The calculated interference pattern is digitized to 12-bit information and analyzed by a home-written software in which an FFT algorithm is implemented. The FFT algorithm can calculate the amplitude and the phase of the calculated sum interference pattern. A given phase change can be introduced for each individual interference pattern, in analogy with the phase change that occurs between two channels of one pair when a binding event is taking place in one of the channels. After calculating the interference pattern and its Fast Fourier Transform, the resulting phase changes for different pair of channels in the four-channel YI are extracted. Finally, by comparing the calculated phase changes with the introduced ones, the PE and CT can be calculated for all channel pairs. This calculation can be performed for different distances of the CCD camera from the chip endface and/or different phase changes introduced at each channel.
In short, these calculations are presented in the following diagram:

```
┌─────────────────────────┐
│ Initialize:             │
│ Nr. of channels = 4     │          ┌──────────────────────┐
│ Nr. of camera pixels = 512│ ◄──────│ Add phase change     │
└─────────────────────────┘          │ to output channels   │
            │                         └──────────────────────┘
            ▼                                     ▲
┌─────────────────────────┐                       │
│ Calculate intensity of the│                     │
│ interference pattern using│                     │
│ Eq. (2.2) and (2.3)     │                       │
└─────────────────────────┘                       │
            │                                      │
            ▼                                      │
┌─────────────────────────┐                       │
│ Apply the FFT algorithm │                       │
└─────────────────────────┘                       │
            │                                      │
            ▼                                      │
┌─────────────────────────┐                       │
│ Determine each peak     │                       │
│ position and the        │                       │
│ corresponding phase     │                       │
└─────────────────────────┘                       │
            │──────────────────────────────────────┘
            ▼
┌─────────────────────────┐
│ Calculate the PE and CT │
└─────────────────────────┘
```

29
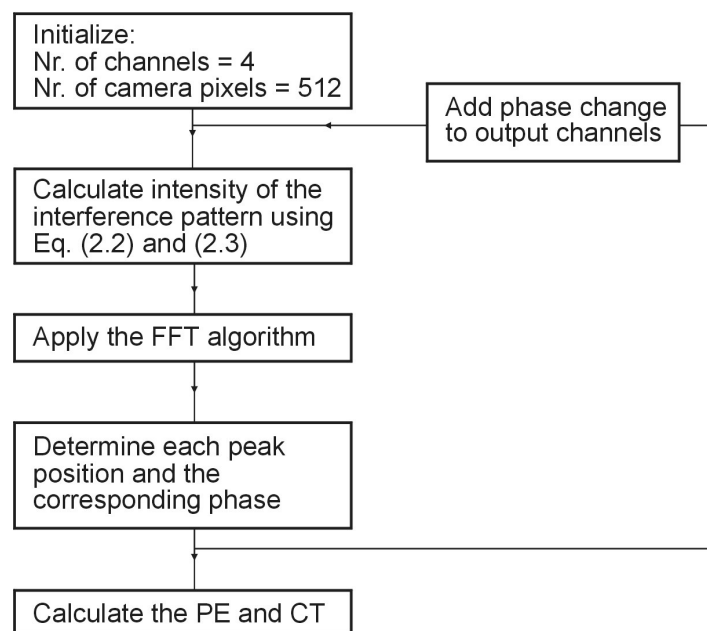
References

[1] J. Wilson and J.F.B Hawkes, *Optoelectronics: An introduction* (Prentice Hall, London, 1989).

[2] A. Ymeti, J.S. Kanger, R. Wijn, P.V. Lambeck, and J. Greve, Development of a multichannel integrated interferometer immunosensor, Sensors and Actuators B 83, 1-7 (2002).

[3] E. Hecht, *Optics* (Addison Wesley, Reading, Mass., 1998).

[4] K. Tiefenthaler and W. Lukosz, Sensitivity of grating couplers as integrated-optical chemical sensors, J. Opt. Soc. Am. B 6, 209-220 (1989).

[5] A. Ymeti, J.S. Kanger, J. Greve, P.V. Lambeck, R. Wijn, and R.G. Heideman, Realization of a multichannel integrated Young interferometer chemical sensor, Applied Optics 42, 5649-5660 (2003).

[6] S. Nakadate, Phase detection of equidistant fringes for highly sensitive optical sensing. I. Principle and error analysis, J. Opt. Soc. Am. A 5, 1258-1264 (1988).

[7] M. Kujawinska and J. Wojciak, High accuracy Fourier Transform fringe pattern analysis, Optics and Lasers in Engineering 14, 325-339 (1991).

[8] R.N. Bracewell, *The Fourier Transform and its Applications* (McGraw-Hill, New York, 1965).

[9] E.R. Brigham, *The Fast Fourier Transform* (Prentice-Hall, Englewood Cliffs, N. J., 1974).

[10] M. Cerna and A.F. Harvey, The fundamentals of FFT-based signal analysis and measurement, Application Note 041, National Instruments, (2000), (www.ni.com).

[11] F.J. Harris, On the use of windows for harmonic analysis with the discrete Fourier transform, in *Proceedings of IEEE 66* (Institute of Electrical and Electronics Engineers, New York, 1978), pp. 51-83.

[12] A.H. Nuttall, Some windows with very good sidelobe behavior, *IEEE Transactions on Acoustics, Speech, and Signal Processing 29*, 84-91 (1981).

CHAPTER THREE

DESIGN AND REALIZATION

In this chapter, the design and realization of an IO sensor array, based on Young interferometry for immunosensing, will be described. First, a number of objectives and requirements will be listed, followed by the boundary conditions and degrees of freedom. Analysis of sensitivity and disturbing factors will lead to the functional design of the sensing system. Next, the design of each individual subfunction will be described in detail. The final design of the multichannel IO YI sensor will be presented and the process flow for realization of the optical chip will be described.[1]

---

[1] Part of the results of this chapter has been published as:

a. A. Ymeti, J.S. Kanger, R. Wijn, P.V. Lambeck, and J. Greve, Development of a multichannel integrated interferometer immunosensor, Sensors and Actuators B 83, 1-7 (2002).

b. A. Ymeti, J.S. Kanger, J. Greve, P.V. Lambeck, R. Wijn, and R.G. Heideman, Realization of a multichannel integrated Young interferometer chemical sensor, Applied Optics 42, 5649-5660 (2003).

3.1   Objectives and requirements

The feasibility character of the project implies the investigation of the potential of the principle for an IO YI sensor array, to be given in terms of many aspects related to both performance and price. Hence, the array has not to obey a well-defined set of quantitative specifications. The focus will be on exploring limits of performance while taking into account the costs, where aims are expressed in terms of properties, being e.g. "as high as possible" (shortened as high), "as low as possible" (shortened as low), etc.

The chapter focuses on the design and realization of the IO readout system taking into account its relations to the chemo-optical interfaces and the microfluidic system.

First aims are:

1.   High sensitivity to the measurand
2.   Low sensitivity to disturbing factors

Both objectives in fact imply already the three following objectives:

3.   High resolution
4.   Low detection limit
5.   Good stability

Other objectives related to the system performance are:

6.   Tolerant to technological imperfections (calibration)
7.   Simultaneous readout of all channels
8.   Short response time
9.   Good selectivity

Objectives related to the costs:

1.   Simple technology
2.   Small chip area
3.   Cheap peripheral equipment
4.   Low costs of use

Often there is some contradiction between performance and costs requirements in the sense that better performance often requires more-expensive technology and equipment. However, generally we will aim at a comprise in which a satisfactory performance can be achieved with a relatively cheap technology and equipment.

Furthermore, aims such as monomodality and low insertion losses will be derived from a further analysis that will be presented later in this chapter.

33

3.2   Boundary conditions

1. In the sensor array the integrated optical readout system, the sensitive chemical interfaces and a cuvette or a microfluidic transport system will be (hybridly) integrated.
2. For the realization of the IO readout system the Silicon-oxynitride technology as developed by the IOMS- group of the MESA[+] Institute [1-3] will be applied. Here, it has to be noted that this technology also shows its limitations, which in a first instance have to be considered as boundary conditions during the design, e.g. a chip size of 4" and a minimum channel width of 2 μm. This technology affords the production of amorphous, dense SiON layers with refractive indices in between 1.45 (SiO_2) and 2.0 (Si_3N_4) and applying lateral structures in these layers. Technological tolerances of the processes are known.
3. The spatial frequency matching condition, as derived in the previous chapter, has to be obeyed.
4. In first instance peripheral equipment (light source and CCD camera) as available at the Biophysical Techniques Group will be used.

3.3   Degrees of freedom

1. With respect to the IO - readout system:
-    the specific SiON materials
-    the functional structure
-    the implementation of the subfunctions
-    the number of channels
-    the layout
-    the transversal and lateral geometry of the structures
-    the wavelength

2. With respect to the microfluidics: Nearly identical as for the IO readout system. Note that there was no focus on this part.

3. With respect to the chemo-optical interfaces: Interfaces already tested by others will be applied.

3.4   Analysis of sensitivity

Here, the sensitivity chain: $\Delta C => \Delta n => \Delta N_{eff} => \Delta\varphi => \Delta$(interference pattern) will be discussed in detail.

- For the relation of refractive index change Δn with the change in concentration ΔC we have:

$\Delta n = \dfrac{\partial n}{\partial C} \Delta C$: $\partial n / \partial C$ depends on the properties of the material, e.g. in case of proteins this coefficient is ~ 0.188 ml/g.

- $\Delta N_{eff} = \dfrac{\partial N_{eff}}{\partial n_{eff}} \Delta n_{eff}$: $\partial N_{eff} / \partial n_{eff}$ is the sensitivity coefficient of N_{eff} with respect to

the change of the effective refractive index of the immobilized receptor layer n_{eff}, which represents both the refractive index change, which is caused by an exchange of solution by analyte particles at the filled receptor sites, and the refractive index change of the receptor molecule itself as a consequence of the change of its electron structure at being filled. In order to have a high sensitivity, $\partial N_{eff} / \partial n_{eff}$ should be maximized. This sensitivity coefficient depends on the refractive indices of the substrate, core, and analyte solution (n_S, n_F, and n_{sol}, respectively), the thickness of the core layer, d_F, the wavelength of the light source, λ, and polarization used (TE or TM).

Using the SiO_xN_y technology, highest sensitivity is obtained (Parriaux et al. [4]), by using Si_3N_4 as material for the core layer of the structure, having the highest refractive index of the SiON family. The requirement that the modal field should be well confined within a layer stack as thin as possible (costs) implies that the substrate and cover layers should have a low refractive index, hence: SiO_2. The low index of the substrate layer also favors the sensitivity (Parriaux et al. [4]).

In addition, $\partial N_{eff} / \partial n_{eff}$ depends on the thickness of the core layer, which in the same time should be chosen such that given the wavelength and polarization (TE is chosen whereas TM will be attenuated by optimization of $d_{substrate}$), the channel waveguide should be monomode (interference of one mode only is required) in the transversal direction. The width and ridge height of the ridge type channel waveguide should be chosen such that the channel is monomodal in the lateral direction too and in addition, in such a way that modal field should be confined at maximum in the lateral direction. The lateral field profile is preferred to be as small as possible, because this gives the best agreement with the point source approximation used to describe the sensing system (see chapter 2).

- $\Delta \varphi = \dfrac{2\pi}{\lambda} l \Delta N_{eff}$: Increasing the interaction length, l, and choosing a smaller

wavelength λ can result in a higher sensitivity of $\Delta \varphi$ with respect to N_{eff}. However, l is limited by the size of the chip and for choosing λ, other factors such as scattering losses, which increase when λ decreases, should be considered.

- In a final stage, the change of the phase difference effects a change of the interference pattern from which using Fourier analysis, the $\Delta \varphi$ can be derived. This has been treated in chapter 2 already and has consequences for the distance between the output channels only.

35

- Finally, the complete sensitivity chain can be written as: $\Delta\varphi = \frac{2\pi}{\lambda} l \frac{\partial N_{eff}}{\partial n_{eff}} \frac{\partial n_{eff}}{\partial C} \Delta C$. $\Delta\varphi$ is retrieved from the interference pattern using Fourier analysis (see chapter 2).

3.5   Analysis of disturbing factors

1. Light, not contained in the channel modes, that arrives from the endface of the IO chip (propagating as slab modes) at the CCD camera, but also light from other light sources, is one of the major disturbing factors. Therefore, generation of slab modes or their arrival at the chip endface have to be suppressed as much as possible. Suppression of generation of the slab light also favors low insertion losses.

The slab light can be caused by:
- Functional losses, where we can first mention non-complete coupling of the light into the input channel waveguide, e.g. when end-fire coupling (using a microscope objective) is implemented, but also in case when a fiber-to-chip (fc) connection is used. Hence, both because of reduction of slab light and because of the power budget, the incoupling efficiency has to be as high as possible. In addition, the power splitting functions e.g. consisting of a network of Y-junctions contribute to the slab light, as well as edges of the sensing window do.
- Scattering within the materials or at material boundaries.
 Less generation of the slab light can be achieved by:
- A local adaptation of the channels cross-section by tapering, at the input endface of the IO chip in order to have maximum overlap of the incoming field distribution and the modal field. This can be implemented by using a fiber-to-chip incoupling connection, which allows a high coupling efficiency (up to ~ 50% [5]).
- In case of Y-junctions used in the power splitter, implementing a splitting angle θ of the Y-junction $1 < \theta < 2^0$, as a compromise between relatively low functional losses, a splitting ratio well approaching 1:1 (technological tolerances do play a role here) and an acceptable Y-junction length [6].
- Scattering losses at the sensing window can be reduced by implementing a transversal tapering section in the SiO_2 cladding layer. In order to have small losses, the taper angle should be small ($< 10^0$) which can be easily realized in SiON technology by using wet etching techniques.
- In the standard SiON technology materials have been optimized already with respect to bulk scattering.
- Reduction of scattering at materials boundaries requires the surface roughness to be as low as possible, and this is related with the technology used for realization of different waveguide layers and the refractive index difference

between both adjacent layers. The technology allows for channel propagation losses < 1 dB/cm in the visible light region.

Implementing a 90^0-bend input waveguide can prevent arrival of the slab light, which is generated by an imperfect fc coupling, at the chip endface. This type of layout also allows for efficient incorporation of slab light absorbers around the fc coupling region.

2. Endface roughness: If the chip endface is not cleaved along the proper crystal plane, the endface will not be smooth and as a result, the phase relation at the output is disturbed. This will effect the propagation of the output light both with respect to direction and phase and it will result in deterioration of the interference pattern.

3. In the measuring channel of the sensor, the evanescent field probes also the solution to be analyzed. In order to compensate for this sensitivity, an identical sensing window should be realized in the reference channel. Technological tolerances hamper the sensing windows to be perfectly identical. In case an immunosensing event is monitored, if possible, the reference window has to be supplied with a passive layer that has a refractive index, thickness, and temperature dependence nearly identical as the active receptor layer immobilized in the measuring channel. The reference channel also compensates for homogeneous temperature changes of the chip.

4. Temperature difference between channels: This can be caused by temperature changes of the environment, e.g. draught, etc. Furthermore, a temperature difference can occur between channels e.g. in case an immunoreaction takes place in the measuring channel where a heat exchange with the surrounding medium may occur. A difference in the temperature of the sample solutions, which are flown in measuring and reference channel, can also result in a temperature difference between both channels and hence, this has to be avoided. The effect of temperature differences can be reduced:

- by thermostating the system.
- by positioning the channels close to each other, such that these differences will be reduced. The distance is limited however by the requirement, that the overlap of the modal fields of two adjacent channels has to be negligible. Also here the channel optimization done in 3.4, directed on maximum lateral confinement of the modal profile, is advantageous. Calculations using Prometheus software [7] show that, for the finally applied channels and wavelength, at a distance of ~ 15 μm this overlap is negligible.
- by using a substrate material with a high thermal conductivity such as Silicon (thermal short circuit).
- by applying corrections: e.g. later on in chapter 6 it will be shown that in a multichannel YI sensor the information from one or several channels can be used to correct the effect of temperature differences between channels where a binding event is measured.

37

5. Noise generated by the light source and the CCD camera: Noise generated by the light source and the CCD camera limits the resolution of the sensor. As a result, light source and CCD camera that show low noise levels should give the best performance, but here a compromise with associated costs has to be taken.

6. Air medium between the channels output and the CCD camera: Density fluctuations (e.g. caused by turbulence) of the air between the output channels and the CCD camera can deteriorate the stability of the interference pattern, which directly influences the stability of the measurements. Covering the whole system and keeping the room temperature constant can reduce the influence of these disturbances.

7. Vibrations of the set-up: Vibrations of the set-up may cause a drift in the output signals. This effect can be reduced by firmly fixing all components of the set-up; also, the use of an air-lifted optical table can isolate the vibrations caused by the support.

8. Contaminations: contaminations that are present in the analyte solution such as dust particles can disturb the measurements once being at the sensing surface.

9. Presence of TM light: Here, it is important the appropriate choice of d_{buffer} in order to have a strong attenuation of TM while TE attenuation is < 0.01 dB/cm. In that way, only TE mode can propagate through the waveguide.

10. Technological imperfections: Here, we mention as examples non-uniformity of the thickness and width of the channel waveguide, imperfect splitting ratio of the input light, e.g. in a Y-splitter, different length of the channels, as well as that of the sensing windows. These deviations are constant, suggesting application of calibration to reduce their influence.

3.6   The functional design

After this analysis, we can give the complete scheme of the functional design (see Figure 3.1). Light from a light source (1) is polarized (2) and is launched into a monomodal channel waveguide as the TE mode by means of a fiber-to-chip connection (3). A 90^0–bend input channel waveguide (4) is used to prevent arrival of the slab light at the chip endface. If necessary, slab light absorbers (5) can be applied around the fiber-to-chip coupling function. A distributed TM attenuator (6, not shown in figure) is applied for removing remaining TM light by adjusting the thickness of the buffer layer to an appropriate value (see section 3.5). A splitter (7) will divide the power equally over four output channels. Furthermore, sensing windows (8-11) are realized on top of each output channel where the TE_{00} channel mode can probe the chemo-optical interfaces applied on each window. The coherent output beams are overlapping each other and an interference pattern is generated, which is recorded by a CCD camera (12) and analyzed by a

computer program (13) based on an FFT algorithm. The divergent light beams are collimated in the vertical direction by a cylindrical lens (14) in order to increase the amount of light reaching the CCD camera. All subfunctions in the optical chip are connected by single mode channel waveguides.
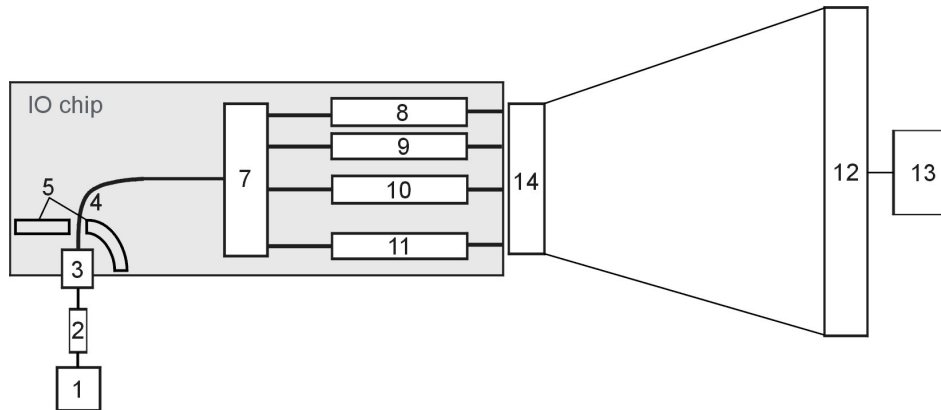

Figure 3.1 *The functional design of an IO YI sensing system. See the text for meaning of the numbered subfunctions.*

3.7 Requirements to and implementations of the subfunctions

3.7.1 The CCD camera

In order to have a large *S/N* ratio, the noise level of the CCD camera should be low. In addition, a relatively high frame rate is preferred to allow a fast signal processing, and by averaging, the noise level of the signal can be suppressed. Furthermore, a high dynamic range will also effectively increase the signal. In our case we used a CCD camera (Teli CS-3440; 756 x 575 pixels) with a frame rate of 25 Hz, 12-bit dynamic range, pixel width w_{pixel} = 11.6 μm, and recording length L_{CCD} = 8.8 mm.

3.7.2 Signal analysis

A computer program based on a 2D-FFT algorithm is implemented for analysis of the sum interference pattern, which is recorded by the CCD camera and digitized to 12-bit information. The algorithm consists of selecting all different peaks, which correspond to all pair of channels, in the amplitude of the Fast Fourier-

39

transformed interference pattern. The phase value corresponding to each pair of channels is extracted at the phase part of the FFT at the given spatial frequencies. The program allows the phase data to be extracted and plotted on-line, which can also be later used for further signal processing. The maximum bandwidth used for the measurements is 25 Hz, which is limited by the frame rate of the CCD camera.

3.7.3   The light source

The light source should be monochromatic as a requirement for generation of the interference pattern. There is a preference for a laser diode with a wavelength between 560 nm and 850 nm, as a cheap light source and for an efficient coupling to the fiber. The available CCD camera matches this wavelength range, while the propagation losses of the SiON materials in this wavelength range are well acceptable (< 1 dB/cm, its specific value depending on the specific material, wavelength and channel structure). In addition, the light source should have a high output power and low shot noise, both contributing to a large S/N ratio.
The definitive choice of the wavelength depends on other points of analysis such as sensitivity, functional losses, etc. A relatively high sensitivity with moderate scattering losses can be achieved for $\lambda = 647$ nm, which was decided to be used for our measurements. We used an Ar laser (Coherent, INNOVA 70 SPECTRUM, power stability $< 0.5\%$).

3.7.4   The fiber-to-chip connection unit

An efficient fiber-to-chip coupling can be achieved by a good match of the field profile of the single-mode fiber mode and the mode of the channel waveguide. This can be implemented by adapting the channel waveguide to the fiber using tapering. The single mode fiber ($\lambda = 647$ nm) has a nearly Gaussian field profile with a waist of $\sim$ 4.75 μm. Optimal fiber-to-chip coupling can be calculated (Prometheus software [7]) to require for a channel of 4 μm width and a ridge height of 2 nm, a core layer thickness of about 8 nm. In practice a safer value of $\sim$ 15 nm is used, as a compromise between coupling efficiency and wafer yield. For obtaining monomodality, a 2 nm ridge height is applied. Adiabatic transition from this endface cross-section to the cross-section of the common waveguide requires a transversal taper as described in reference [8]. Alignment of the fiber with respect to the chip channel will be done using V-shaped grooves obtainable in silicon <100> wafers perpendicular to [100]-crystal plane. For further details on implementation and performance of the fiber-to-chip connection, see reference [8].

40

3.7.5 The single-mode channel waveguides

For reasons of technological simplicity, the single-mode channel waveguides that connects different subfunctions should have an identical core cross-section with the sensing waveguides. The core cross-section with SiO_2 as substrate should also be monomodal in the sensing region.

The thickness of the core layer has to be determined based on the criteria for a maximum sensitivity. For homogeneous sensing, the optimal core layer thickness depends on the refractive index of the sensitive material. Calculations using the Slab software [9] show that in a watery environment (n_{water} ~ 1.33) the maximum sensitivity can be achieved for a core layer thickness of ~ 55 nm. For surface sensing, being restricted to biochemical reactions in a watery environment and assuming a refractive index n_p ~ 1.45 for a protein layer [10] bound on a sensor surface, the optimal Si_3N_4 layer thickness can be calculated to be ~ 70 nm. In our sensor system we will choose the thickness of the core layer to be 70 nm.

The channel waveguides will be of the ridge type in order to cope well on the one hand with the boundary condition of minimum width of 2 μm and on the other hand with the requirements of monomodality and lateral confinement. The latter will be stronger, the larger the lateral contrast. The ridge of the single mode channel waveguides will be realized in the core layer. The height of the channel ridge should be as large as possible for optimal lateral confinement, while maintaining monomodality. This value also depends upon the material on the top of the core layer such as SiO_2 in the propagation guides and sensing material in the interaction window. The choice of the ridge height should also take into account the fabrication tolerances, which in lateral direction can be as large as ~ 0.1 μm, in order to guarantee monomodal behavior. Considering a channel width of 4 μm (see 3.7.4), and a core layer thickness of 70 nm, best ridge height can be calculated to be 0.7 nm.

3.7.6 Bend

A requirement for the bend is that its radius should be sufficiently large such that the functional radiation losses are negligible, in our case meaning less than 0.1 dB. On the other hand, the bend radius has to be as small as possible in order to reduce the required chip area. For our waveguide structure and for 647 nm wavelength, the optimal bend radius can be calculated to be R_{bend} ~ 10 mm [11].

3.7.7 Polarizer

As we have concluded in section 3.5, the TE_{00} mode has to be transmitted, while the TM_{00} mode is not allowed to be present at the outputs of the IO chip. To exclude TM output, a distributed TM attenuator is inserted by adjusting the buffer

layer thickness. Allowing a 0.02 dB/cm leakage induced attenuation for the TE_{00} mode, a maximum TM_{00} mode attenuation of ~ 8 dB/cm is obtained at a buffer layer thickness of 1.25 μm [8].

3.7.8   Number of the channels

The number of channels is decided to be 4, resulting in 6 spatial frequencies in the interference pattern. This choice is made because we consider this to be the minimum number of channels required for an efficient exploration of the properties of a sensor array. The maximum number of channels depends on the requirements for a good separation of different peaks at the amplitude of the FFT in order to have a small PE and CT (see chapter 2), which in its turn depends on the minimum and maximum distance between the channels. Considering a simultaneous and independent monitoring of the phase change for each pair of channels, λ = 647 nm, and given parameters of the CCD camera, the maximum number of channels is estimated to be ~ 17.

3.7.9   The splitting function

Different optical components can be used to perform splitting of the input light to different channels, e.g. Y-junctions, 3-dB couplers, MMI couplers, Star couplers, etc. For designing a multichannel YI, multiple Y-junctions will be used considering their simplicity, fabrication tolerances, etc. In section 3.5, we discussed already the opening angle of the Y-junction. In our design a Y-junction angle of 2^0 has been chosen. To obtain splitting over four channels, a network of three Y-junctions has been used in such a way that two output channels of the first Y-junction serve as input channels for the next two ones. This network has to end up in channel distances appropriate for the output channels. To shorten the length of the Y-junctions appropriately, S-bends with bending radii of 50 mm have been applied.

3.7.10   Flow system

Application of sample solutions to the sensing windows of the four-channel sensor will be made by integrating either a flow cuvette (see chapter 4, 5, and 6) or a microfluidic system (see chapter 7). These systems are required to apply simultaneously different sample solutions in all four sensing windows. The flow cuvette will be fixed onto the optical chip by slightly pressing it on the top, whereas the microfluidic system will be permanently bonded to the optical chip. The flow cuvette we will use for the four-channel sensor is made from Perspex and is 31 mm long and 7 mm wide. It has four flow chambers each with a volume of 1.2 μl (6 mm long and 3 mm wide), see Figure 3.2.
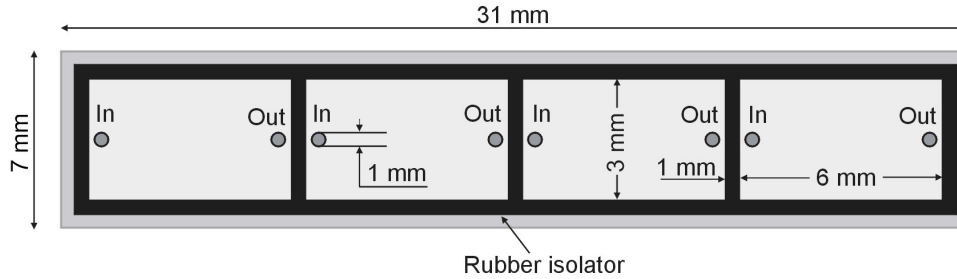
Figure 3.2 *Bottom-view of the four-chamber flow-through cuvette; each chamber has an In(let) and an Out(let), through which the sampling liquid flows to/from the sensing window.*

Each chamber of the cuvette has an inlet and outlet that are connected via a tubing system with the sampling reservoirs, which contain solutions to be monitored, and to the waste, respectively. Samples are flown by means of a peristaltic pump (Ismatec MS-REGLO) that has four separate pumping channels, each of them functioning independently from each other. The microfluidic system will be treated in detail in chapter 7.

3.7.11 The sensing windows

Besides the limited size of the chip (4'') and the required minimum length of other subfunctions in the optical chip (see 3.6), the need for integrating the four sensing windows with a microfluidic system or a flow cuvette (see 3.7.10) further reduces the interaction length. In addition, an interdistance between windows along channel direction is needed to allow a good alignment of the cuvette. Considering all aspects already discussed, the length of the four sensing windows will be chosen $l = 4$ mm (width $w_{win} = 100$ μm) with an interdistance of $l_{int} = 3$ mm.

Last two restrictions can be overcome by using a microfluidic system, where the sensing windows can be implemented parallel to each other and no interdistance is necessary. In that case, each sensing window can be as long as ~ 28 mm, resulting in an improvement of the sensitivity by almost one order of magnitude.

3.7.12 Chip endface

The integrated chip should be cleaved along [100]-crystal plane to suppress the output phase disturbances and scattering losses effects. In that way, a better-defined interference pattern will be generated. This means that channel direction

in the output part should be chosen perpendicular to that plane. In case the quality of the endfaces should be the resolution-limiting parameter, polishing of the endfaces may be required. For this however, no facilities are present in the MESA$^+$ clean room lab.

3.7.13 Channel distances d_{ij} and the chip endface - CCD camera distance L

The spatial frequency matching condition requires that $\dfrac{1}{\lambda}\dfrac{d_{ij}}{L} = \dfrac{N_{ij}}{L_{CCD}}$, where d_{ij} is the distance between channel i and j and N_{ij} is an integer. All values of L that fulfill this condition for a given d_{ij} are noted as 'matching' distances. From this relation it results that if the distances between the channels will be increased, the 'matching' distances of the CCD camera will occur more often. In addition, if these distances will be chosen as an integer number of the smallest distance, more often 'matching' distances will occur too.

The minimum and maximum distance between channels should be chosen such that combined with the distance of the CCD camera from the chip endface, L, at least one interference fringe will be recorded by the CCD camera and at least two pixels should correspond to one interference fringe, both conditions being necessary for signal processing [12]. Considering also the discussion in 3.5 about the requirement that the overlap of the modal fields of two adjacent channels has to be negligible, the minimum distance between the channels should be ~ 15 μm.

An increase of the distances between channels may also result in smaller PE and CT (see section 2.3.2).

The distances between channels should be small compared to the chip endface – CCD camera distance (several centimeters) for good agreement with the point source approximation in section 2.2.1.

Table 3.1 *Three different configurations of the distance between the channels in the four-channel IO YI sensor.*

	Structure		
	1	2	3
d_{12} (μm)	60	50	100
d_{23} (μm)	80	100	200
d_{34} (μm)	100	200	400

Furthermore, for a given *d*, *L* is required to be such that the interference pattern generated can be recorded by all pixels of the CCD camera, called as the optimal distance. Use of a cylindrical lens to collimate the output divergent beams in the vertical direction for an optimal covering of the interference pattern along this direction does not introduce any additional limitation for *L*. A compromise should be found between the optimal distance and 'matching' distances. We have chosen for the distance between the channels the three configurations that are given in Table 3.1.

Structures 2 and 3 were prepared with larger difference between output channels distances in order to explore the PE and CT as a function of this difference, see section 2.3.2. The three different configurations were implemented in the same chip.

3.8   Design of the four-channel IO YI sensor

Based on the analysis already presented in previous sections, here the final design of the four-channel YI sensor will be presented. The optimization of the individual components resulted in multilayer cross-sections that are strongly dependent on the desired function. For connecting these components, while maintaining their optimized structures, transversal adiabatic tapers are needed, which have a small taper angle ($< 0.03^0$) to have functional tapering losses < 0.1 dB [13].

The final structure design of the four-channel YI sensor is shown in Figure 3.3: top-view (A), cross-section perpendicular to output channels (B) and side-view along the optical path (C).

The parameters of the final design of the four-channel IO YI sensor (structure 1), which will be applied in chapters 5, 6, and 7, are summarized in Table 3.2. The distance between the mutually parallel output branches of the first Y-junction is chosen $D = 160$ μm and the length of the splitting section is $L_{split} \sim 10$ mm.

For exploring the working principle and performance of a multichannel YI sensor before starting optimization and improvement, as an initial design a simpler four-channel IO YI sensor has been realized that has everywhere a core-layer thickness of 90 nm, ridge height of 1 nm, and width of 2 μm (sensor structure 4, see section 4.3). Here, coupling of the TE-polarized light was performed by the end-fire coupling method using a microscope objective with an $NA = 0.65$. All other parameters were chosen as described before.

45

Figure 3.3 *Schematic top-view (A), cross section along AA' (B) and side-view (C) of the four-channel IO YI sensor; Wi indicates the sensing window on channel i, d_{ij} indicates the distance between channels i and j, R_{bend} and R_{S-bend} are the radius of 90^0-bend and S-bends respectively, W is the width of the channel waveguide. The dimensions of the chip are 63 mm x 24 mm.*

In addition, a two-channel YI sensor (sensor structure 5), which has the same waveguide parameters as sensor structure 4, was realized in the beginning of this project to explore the performance of a two-channel YI, as a first step towards realization of a multichannel sensor. In this structure, the distance between output channels was chosen 60 µm, whereas the length of sensing windows was 20 mm for the sensor that has a window in the measuring channel only (sensor structure 5.1, see section 4.1), and 9 mm for the two-channel sensor that has windows in both measuring and reference channels (sensor structure 5.2, see section 4.2).

Table 3.2 *Parameters of the four-channel IO YI sensor. See text and Figure 3.3 for a detailed description of each parameter.*

Parameter			
Name	Symbol	Value	Dimension
Thickness of the core layer	d_{F1}	15	nm
	d_{F2}	70	nm
Height of the channel ridge	h_1	2	nm
	h_2	0.7	nm
Thickness of SiO_2 subs. layer	d_S	1.25	µm
Thickness of SiO_2 cover layer	d_C	1.5	µm
Channel width	W	4	µm
Radius of 90^0-bend	R_{bend}	10	mm
Radius of S-bend	$R_{S\text{-}bend}$	50	mm
Length of sensing windows	l	4	mm
Width of sensing windows	w_{win}	100	µm
Windows interdistance	l_{int}	3	mm
Distance between channels	d_{12}	60	µm
	d_{23}	80	µm
	d_{34}	100	µm

47

3.9 Realization

The main processing steps that are applied for realization of the optical chip are summarized in a flow chart presented in Figure 3.4.

Processing step	**Cross-section perpend. to the channel**
1. Starting with a highly conductive (0.010-0.018 Ω cm) 4'' Silicon <100> wafer.	
2. Thermal wafer oxidation (at 1150 ^{0}C), resulting into a SiO_2 layer thickness > 1300 nm.	
3. Measuring thermal SiO_2 layer thickness with ellipsometer.	
4. Etching back thermal SiO_2 layer to a thickness of 1300 nm.	
5. Determination of the Si crystal planes orientation with an accuracy better than 0.1^0, as is required for realization of appropriately oriented V- grooves and output channels.	
6. Applying alignment marks by etching > 500 nm thermal SiO_2 layer.	
7. Deposition of 70 nm Si_3N_4 using LPCVD at 800 ^{0}C.	
8. Etching the fc tapered region (55 nm LPCVD Si_3N_4) using BHF.	
9. Channel ridge definition using BHF. By applying a two-step photolithography method [14] a ridge height of 2.0 nm is etched in the fiber-to-chip region and 0.7 nm elsewhere. The applied masks in addition define the position of the V-grooves.	
10. After an additional photolithographic step, etching away 15 nm LPCVD Si_3N_4 in V-grooves region.	

11. Etching away 1300 nm thermal SiO_2 in V-grooves region.

12. Etching of V-grooves with a KOH solution (73-74 ^{0}C, V-groove width 145 μm); during this process, the SiO_2 layer is partly etched off, diminishing its thickness to 1.25 μm.

13. Deposition of the 1.5 μm thick SiO_2 layer using PECVD at 300 ^{0}C.

14. Etching of the sensing windows (length of 4 mm and width of 100 μm) and window tapers using BHF.

15. Sawing grooves at the V-groove ends near the waveguiding channel.

16. Dicing.

17. Mounting the fibers.

Cross-section along the channel

Si SiO_2 Si_3N_4
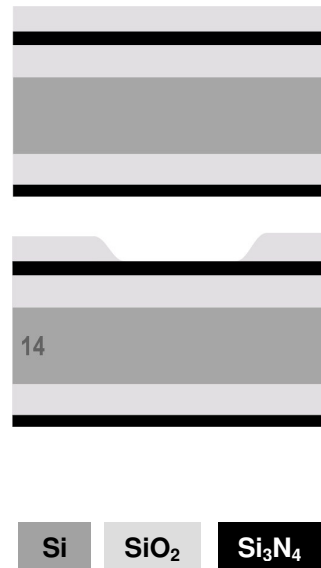
Figure 3.4 *Flow chart for realization of the optical chip.*

After performing all the steps described in Figure 3.4, the integrated chip is cleaved along [100]-crystal plane and an input fiber is applied.

For characterization purposes, testing functions such as straight waveguide channels, 90^0-bends, Y-junctions, fiber-to-chip connecting unit, tapers, and sensing windows were also prepared separately in order to figure out the cause of any malfunction in the device in case it could occur. However, because the performance of the sensor was in line with expectations, the characterization of these individual components has not been done.

3.10   **Summary**

This chapter presents the design and realization of a multichannel IO YI sensor system. Such a system is designed based on a number of requirements related to the performance such as high sensitivity and resolution, simultaneous readout of all channels, good selectivity, etc., and according to some boundary conditions, e.g. hybrid integration of the optical readout system, the sensitive chemical interfaces and a microfluidic system; realization of the IO readout system in the Silicon-oxynitride technology, obeying the spatial frequency matching condition, etc. Degrees of freedom with respect to the IO - readout system, the microfluidics, and the chemo-optical interfaces, should also have to be taken into consideration.

An analysis of the sensitivity is presented, based on which a number of conclusions is drawn, e.g. choice of materials, choice of layer thickness, ridge and the width of the ridge-type channel waveguide, etc. Analysis of the disturbing factors such as slab light, endface roughness, temperature difference between channels, noise generated by the light source and the CCD camera, contaminations, technological imperfections, etc., has introduced some more requirements for the design of the sensor system.

Based on the initial analysis, the functional design of the multichannel IO YI sensor system is implemented. Next, requirements for each individual subfunctions are introduced, starting from the light source, the single-mode channel waveguides, the fiber-to-chip connection unit, input bend, polarizer; continuing further with the splitting function, flow system, the sensing windows, chip endface, the CCD camera, and finally concluding with the spatial frequency matching condition, distance between the channels, and the chip endface – CCD camera distance and ending up with optimal values of the specifying parameters.

This extensive analysis leads to the final design of the sensor system. Here, all the parameters of the system are summarized and illustrated by showing a top-view and cross-sections (transversal and longitudinal) of the optical chip. Finally, different processing steps applied for realization of the optical chip are described using a flow chart.

References

[1]   K. Wörhoff, P.V. Lambeck, N. Albers, O.F.J Noordman, N.F. van Hulst, and T.J.A. Popma, Optimization of LPCVD Silicon onxynitride growth to large refractive index homogeneity and layer thickness uniformity, Proc. SPIE 3099, 257-268 (1996).

[2]   K. Wörhoff, A. Driessen, P.V. Lambeck, L.T.H. Hilderink, P.W.C. Linders, and T.J.A. Popma, Plasma enhanced chemical vapour deposition of silicon oxynitride optimized for application in integrated optics, Sensors and Actuators B 74, 9-12 (1999).

[3]   K. Wörhoff, L.T.H. Hilderink, A. Driessen, and P.V. Lambeck, Silicon oxynitride - A versatile material for integrated optics applications, Journal of the Electrochemical Society 149 (8): F85-F91 (2002).

[4]   O. Parriaux and G.J. Veldhuis, Normalized analysis for the sensitivity optimization of integrated optical evanescent sensors, Journal of Lightwave Technology 16, 573-582 (1998).

[5]   R.G. Heideman and P.V. Lambeck, Simple and reusable fiber-to-chip interconnect with adjustable coupling efficiency, Proceedings of SPIE 3099, Micro-Optical Technologies for Measurement, Sensors, and Microsystems II and Optical Fiber Sensor Technologies and Applications, Munich, Germany, 238-247 (1997).

[6]   G. van Elzakker, Integrated optical evanescent field based read out system for a MEMS gyroscope, M.Sc. Thesis, IOMS - MESA[+], University of Twente, The Netherlands, 2003.

[7]   Prometheus simulation software, C2V, Enschede, The Netherlands.

[8]   R.G. Heideman and P.V. Lambeck, Remote opto-chemical sensing with extreme sensitivity: design, fabrication and performance of a pigtailed integrated optical phase-modulated Mach-Zehnder interferometer system, Sensors and Actuators B 61, 100-127 (1999).

[9]   Slab simulation software, C2V, Enschede,The Netherlands.

[10]   R.G.C. Oudshoorn, R.P.H. Kooyman, and J. Greve, Refractive index and thickness of an adsorbing protein as reporters of monolayer formation, Thin Solid Films 285, 836-840 (1996).

[11]   R. Syms and J. Cozens, *Optical guided waves and devices* (McGraw-Hill, London, 1992).

[12]   S. Chen, B.T. Meggit, and A.J. Rogers, Electronically scanned white light interferometer with enhanced dynamic range, Electron. Lett. 26, 1663-1664 (1990).

[13]   G.I. Parishi, S.E. Haszko, and G.A. Rozgonyi, Tapered windows in SiO_2: the effect of NH_4F:HF dilution and etching temperature, Journal of Electrochemical Society: Solid State Science and Technology 124, 917-921 (1997).

[14] E.C.M. Pennings, Bends in optical ridge waveguides, modeling and experiments, Ph.D. Thesis, Delft University of Technology, The Netherlands, 1990.

52

CHAPTER FOUR

EXPERIMENTAL CHARACTERIZATION

Experimental characterization of the two-channel and four-channel IO YI sensor devices will be presented. The working principle of the multichannel YI sensor will be tested and different error reduction schemes will be applied to reduce the phase error and cross talk. The results obtained will be compared with the calculations performed in chapter 2. Finally, a discussion about the performance of the YI sensor will be made and some conclusions will be presented. [1]

---

[1] Part of the results of this chapter has been published as:

a. A. Ymeti, J.S. Kanger, R. Wijn, P.V. Lambeck, and J. Greve, Development of a multichannel integrated interferometer immunosensor, Sensors and Actuators B 83, 1-7 (2002).

b. A. Ymeti, J.S. Kanger, J. Greve, P.V. Lambeck, R. Wijn, and R.G. Heideman, Realization of a multichannel integrated Young interferometer chemical sensor, Applied Optics 42, 5649-5660 (2003).

4.1   Two-channel IO YI with one sensing window

The two-channel IO YI sensor that has only one sensing window (sensor structure 5.1, page 47) has been tested by measuring the refractive index change between water and water in which a given amount of glucose was dissolved [1].

Figure 4.1 shows the response of the sensor when 0.14% (by weight) glucose solution was applied in the sensing area of the measuring channel. Water was flown through the cuvette before a new sample was introduced. The expected phase change, as calculated by using Eq. (2.6), is ~ 1.1 x 2π, corresponding to a refractive index change of ~ 1.9 x 10^{-4}. The refractive index change between water and water in which a given amount of glucose is dissolved was taken from [1], whereas the effective refractive index N_{eff} was calculated using the Slab simulation Software [2].
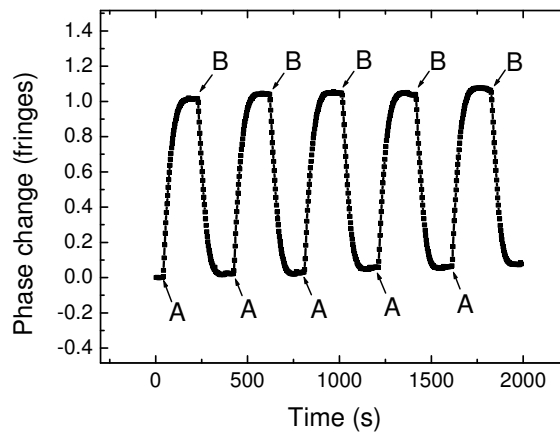

Figure 4.1 *Time-response of the two-channel YI sensor to a repeated stepwise refractive index change of 1.9 x 10^{-4} induced by a glucose solution. A: change from water to glucose solution with concentration of 0.14% (by weight); B: change from glucose solution to water.*

Further test measurements were realized by applying glucose solution with concentrations of 0.07%, 0.14% and 0.21% (by weight). The results are shown in Figure 4.2.A. The measured phase change is plotted versus the glucose concentration in Figure 4.2.B.

The experimental results are in good agreement with the theoretical calculations. The present deviations (maximum of ~ 0.03 x 2π) may be caused due to the

mismatch of the spatial frequency of the interference pattern with discrete spatial frequencies determined from the CCD camera, as concluded from the calculations in section 2.3. These calculations show that in the two-channel YI this error can be as large as ~ 0.025 x 2π. Different error reduction schemes can be applied in that case to reduce the error due to the mismatching effect. In addition, an extra deviation might be caused by systematic errors in preparation of the glucose concentration, which can differ up to ~ 1% from the intended one, errors in the construction of the waveguide structure, such as the length of the sensing window, where a tolerance of ~ 0.1 μm is present, etc. The deviation due to systematic errors is estimated to be ~ 0.01 x 2π. Temperature differences between channels may also introduce a deviation from the expected results.
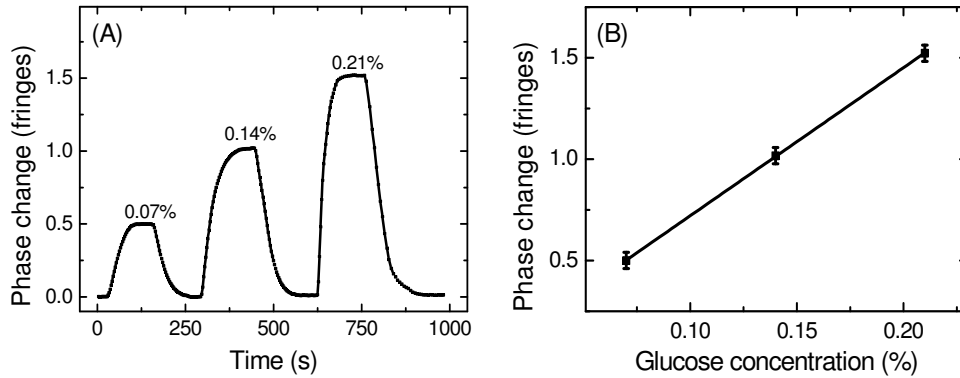

Figure 4.2 *(A) Measured phase change for three glucose solutions with concentrations of 0.07%, 0.14% and 0.21% (by weight). (B) Phase change vs. the glucose concentration: measured (■) and linear fit (—).*

In Figures 4.1 and 4.2.A, it is observed that when a phase change is introduced in the measuring channel, it takes ~ 100 s until a stable base line is obtained. This may be caused by a mixing that takes place between sampling solutions, in this case water and glucose solution, due to the relatively large volume of the cuvette chambers, including that of the tubing system. Implementation of a microfluidic cuvette system can decrease such a long-time response to several seconds, as it will be shown in chapter 7.

These measurements have shown a phase resolution (*S/N* = 1) $\Delta\varphi$ ~ 1 x 10^{-4} x 2π, which corresponds to a refractive index resolution Δn ~ 2 x 10^{-8} and a spatial shift resolution of the interference pattern Δy ~ 70 nm. The long-term phase stability (drift) was ~ 1 x 10^{-3} x $2\pi \cdot h^{-1}$, corresponding to a refractive index change of ~ 2 x 10^{-7} h^{-1}.

4.2 Two-channel IO YI with two sensing windows

4.2.1 Improvement of the data acquisition software

In the two-channel YI, in which a sensing window has been implemented in the measuring channel only, the recorded interference pattern was processed with a frequency of ~ 0.5 Hz, while the CCD camera has a frame rate of 25 Hz. This processing speed was then increased up to ~ 25 Hz by using a faster processor.
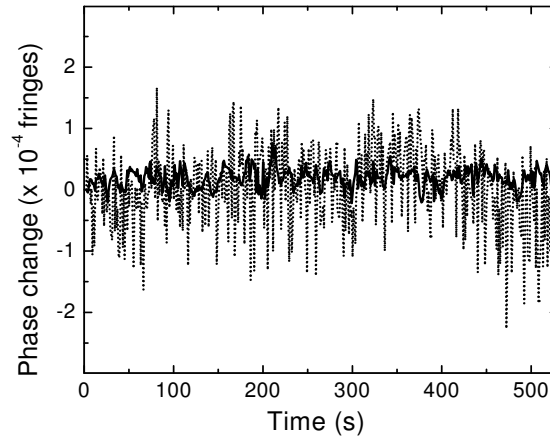

Figure 4.3 *Interferometer signal measured at constant refractive index change using processing speed of 0.5 Hz (dotted line) and 25 Hz (solid line).*

Therefore by averaging, the noise of the measured phase change is expected to be decreased as the square root of the processing speed increase, i.e. by a factor of ~ 7. Figure 4.3 shows the interferometer signal measured at constant refractive index change, i.e. when no refractive index change takes place in any of the channels, for both cases. As expected, the measurements performed with the new higher processing speed show a phase resolution of ~ $1.5 \times 10^{-5} \times 2\pi$ (see Figure 4.3), which is ~ 7 times smaller compared to the previous measured phase value of ~ $1 \times 10^{-4} \times 2\pi$. This phase resolution corresponds to a refractive index resolution of ~ 3×10^{-9}.

Further measurements with the two-channel and four-channel YI devices have therefore been performed with a processing speed of ~ 25 Hz.

57

4.2.2   Measurement of different glucose concentrations

In section 4.1, the measurements performed with the two-channel IO YI, in which only a sensing window in the measuring channel is present, were shown. In order to improve the stability of the measurements, especially by reducing the effects of temperature fluctuations between two branches, another sensing window, identical to the one in the measuring arm, was realized in the reference arm.
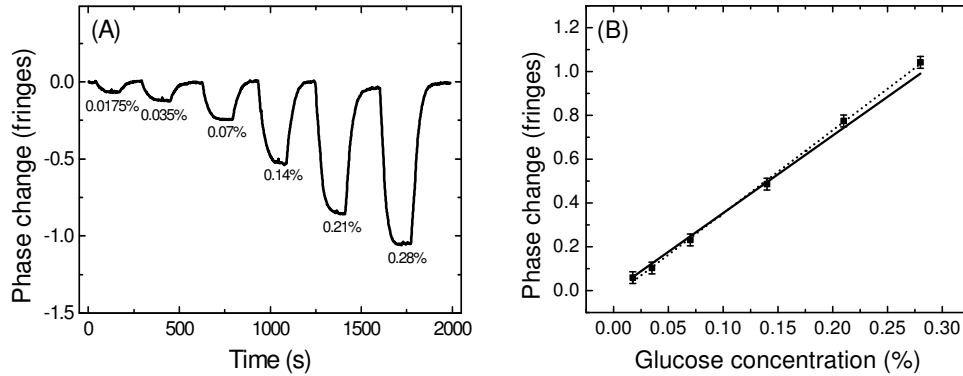

Figure 4.4 *(A) Response of the two-channel YI sensor to refractive index changes caused by applying six different glucose concentrations of 0.0175%, 0.035%, 0.07%, 0.14%, 0.21%, and 0.28% (by weight) intermitted by pure water to the measuring channel of the device. (B) Phase change vs. the glucose concentration: calculated (—), measured (■), linear fit (·····).*

The performance of the realized two-channel YI sensor with two sensing windows (sensor structure 5.2, page 47) was tested by applying solutions of glucose in water, inducing in that way well-defined refractive index changes between measuring and reference channel of the device. In Figure 4.4.A, the response of the sensor to different glucose concentrations applied in the sensing window of the measuring arm, is shown. First pure water was flown simultaneously over both sensing windows, and after several minutes, the flow in the measuring window was changed from water to 0.0175% (by weight) solution of glucose in pure water. When the signal stabilized, water was introduced and flown over the measuring window. This procedure was repeated for five other glucose concentrations, respectively 0.035%, 0.07%, 0.14%, 0.21%, and 0.28% (by weight). The induced refractive index changes, calculated from [1], vary from ~

2.4 x 10^{-5} to ~ 3.8 x 10^{-4}, whereas the corresponding phase changes vary from ~ 0.062 x 2π to ~ 0.991 x 2π.

In Figure 4.4.B, the measured and expected phase changes as a function of the glucose concentration are plotted, including a linear fit of the measured data. Both the calculated and measured refractive index changes and corresponding phase changes for six glucose concentrations used for the measurements are presented in Table 4.1.

According to Figure 4.4.B, the experimental plot (slope ~ 3.78 x 10^{-2} x 2$\pi \cdot$ ml/g) is in good accordance with the expected one (slope ~ 3.54 x 10^{-2} x 2$\pi \cdot$ ml/g). Compared to the glucose measurements realized with the two-channel YI, which has only one sensing window, there is a better accordance between the results obtained and the expected ones.

Table 4.1 *Expected and measured refractive index changes and corresponding phase changes for six different solutions of glucose in pure water with concentration of 0.0175%, 0.035%, 0.07%, 0.14%, 0.21%, and 0.28% (by weight).*

Glucose concentration (%)	Expected refractive index change (x 10^{-4})	Expected phase change (fringes)	Measured refractive index change (x 10^{-4})	Measured phase change (fringes)
0.0175	0.24	0.062	0.23	0.059
0.0350	0.48	0.123	0.40	0.102
0.0700	0.95	0.248	0.89	0.231
0.1400	1.90	0.495	1.86	0.485
0.2100	2.85	0.743	2.97	0.774
0.2800	3.80	0.991	3.99	1.041

59

4.3 Four-channel IO YI sensor

4.3.1 Preliminary measurements

The four-channel YI sensor (sensor structure 4, page 45) was tested by applying solutions of glucose in water to induce well-defined refractive index changes at the channels of the device. First, pure water was flown simultaneously over all four sensing windows. At a certain moment, the flow was changed from water to 0.28% (by weight) glucose solution in channel 1, and after about five minutes, water was flown again into channel 1. The refractive index change induced in channel 1 was ~ 3.8×10^{-4}. This refractive index change corresponds to a phase change of ~ $0.44 \times 2\pi$, considering the sensing window length of 4 mm. A second measurement was done by introducing a phase change in channel 4 of the YI by intermittently applying 0.28% (by weight) glucose solution and pure water. Results of both measurements are given in Table 4.2.

Table 4.2 *Measured phase changes for each pair of channels in the four-channel YI when a phase change of ~ $0.44 \times 2\pi$ is introduced in channel 1 and next in channel 4. See text for further details.*

Phase change	Phase change introduced in channel 1			Phase change introduced in channel 4		
	Expected (2π)	Measured (2π)	Error (2π)	Expected (2π)	Measured (2π)	Error (2π)
$\Delta\varphi_{12}$	0.44	0.396	-0.044	0	-0.038	-0.038
$\Delta\varphi_{13}$	0.44	0.422	-0.018	0	-0.020	-0.020
$\Delta\varphi_{14}$	0.44	0.421	-0.019	-0.44	-0.433	0.007
$\Delta\varphi_{23}$	0	0.033	0.033	0	0.010	0.010
$\Delta\varphi_{34}$	0	0.003	0.003	-0.44	-0.397	0.043
$\Delta\varphi_{24}$	0	-0.002	-0.002	-0.44	-0.393	0.047

Compared to the measurement when a phase change is introduced in channel 1, there is a negative phase change. This result is in accordance with expectations because the shift of the individual interference patterns along the CCD camera surface, when a phase change is introduced in channel 4, is opposite in direction when compared to the case when a phase change is introduced in channel 1. According to the working principle of the multichannel YI (see section 2.2.2), when a phase change is introduced in one of the channels only, the same phase

change is expected for all channel pairs that include this channel. In the experiment performed, because a phase change was introduced in channel 1, the same phase change was expected between channels 1 and 2, 1 and 3, and 1 and 4. The measurement confirms the phase change between those channel pairs where channel 1 is included, as presented in Table 4.2. The same holds when a phase change was introduced in channel 4.

From Table 4.2 one can see that, e.g. in case a phase change was introduced in channel 1, a phase difference between the measured and introduced phase change is observed for all channel pairs that involve channel 1. This error will be referred to as the Phase Error (PE). Furthermore, it is observed that also for those channel pairs that do not include channel 1 (23, 34 and 24) a phase change was recorded. Because this phase error is caused by a phase change of a channel not involved in the given pair of channels, this error will be referred to as the Cross Talk (CT).

The observed PE and CT, being $0.047 \times 2\pi$ at maximum, may be caused by experimental errors such as drift, misalignment, or leakage of the four flow chambers, but also by the errors introduced by the phase extraction algorithm. The latter is expected from the analysis presented in chapter 2, and is a problem well recognized in literature [3-4]. That both effects are present is well illustrated by an experiment in which the phase change is gradually increased from 0 to $2 \times 2\pi$ in channel 1, see Figure 4.5.A. At phase changes of an integer number of fringes the PE and CT are caused only by experimental errors.
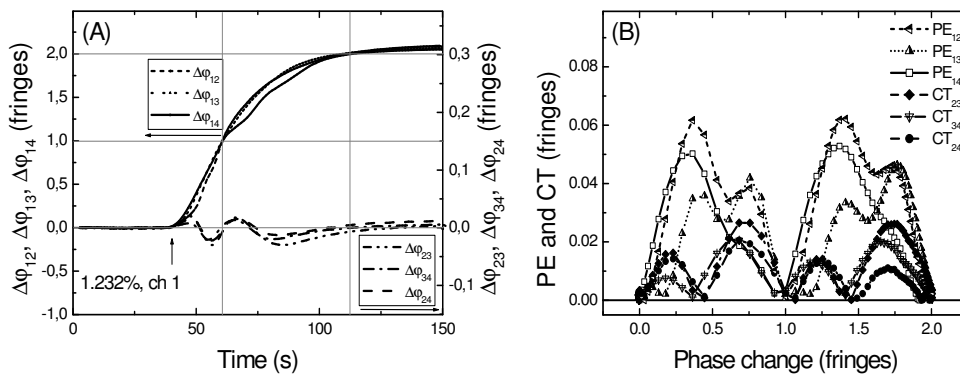

Figure 4.5 *(A) Time-response of the four-channel YI sensor to a phase change of $2 \times 2\pi$ introduced in channel 1 by flowing 1.232% (by weight) glucose solution. (B) Measured PE (PE_{1i}, i = 2,3,4) and CT (CT_{ij}, i,j ≠ 1) vs. the phase change introduced in channel 1.*

In Figure 4.5.B, the PE and CT vs. the phase change introduced in channel 1 are presented; as expected phase change between channels 1 and 2, 1 and 3, and 1 and 4 is taken the average between $\Delta\varphi_{12}$, $\Delta\varphi_{13}$, and $\Delta\varphi_{14}$, and, for the other channel pairs, the expected phase change is zero. It is observed that the PE and CT are nearly zero (~ 0.005 x 2π) for phase changes of 2π and 2 x 2π, being in good accordance with calculations shown in section 2.3.1.

The shape of measured curves, presented in Figure 4.5.B, is corresponding well with the calculated ones shown in Figure 2.8, giving a clear indication that indeed the PE and CT are reduced to ~ 0 when the introduced phase change at the channels is an integer number of fringes, regardless of the spatial frequency matching condition. Furthermore, this is a clear indication that experimental errors are small only, and the deviations observed in Figure 4.5.B, including the ones reported in Table 4.2, are largely due to the data analysis algorithm, as it is concluded from the calculations presented in chapter 2. An exact comparison between measured and calculated curves for the PE and CT is difficult due to the uncertainty in the chip - CCD camera distance L and the strong influence of this parameter on the exact behavior.

In the next section, the different error reduction schemes discussed in section 2.3.2 will be experimentally implemented.

4.3.2   Application of various techniques to reduce the PE and CT

Calculations have shown that the PE and CT observed in the four-channel YI can be reduced if the spatial frequencies of individual interference patterns and those determined from the CCD camera match. For a chosen wavelength of the used light source and for a given set of distances between output parallel channels, the matching condition depends on the distance of the CCD camera to the chip endface L, see Eq. (2.4). In order to be able to reach a matching condition, the camera should be positioned at one of the 'matching' distances as defined in section 2.3. However, the value of L is difficult to be accurately measured due to construction of the camera. For the YI with output distances $d_{12} = 60$ µm, $d_{23} = 80$ µm, and $d_{34} = 100$ µm, the CCD camera was roughly adjusted at a distance somewhat smaller than the 'matching' distance of 45.97 mm, and this distance was increased using ~ 100 µm steps. The PE and CT measured as a function of L, when 0.28% (by weight) glucose solution was flown into channel 1, are shown in Table 4.3. Corresponding phase change can be calculated to be ~ 0.44 x 2π. A minimum in the PE and CT at the distance of L ~ 45.1 mm is observed, the minimum not being zero indicating that no complete matching has been reached.

A reason might be that the distances between output channels of the device deviate from the designed ones during the manufacturing process, where a tolerance of ~ 0.1 µm is present.

Table 4.3 *Measured PE (PE$_{1i}$, i = 2,3,4) and CT (CT$_{ij}$, i,j ≠ 1) in the four-channel YI for different distances of the CCD camera from the chip endface (only some intermediate distances are shown).*

PE and CT (2π)	Distance of the CCD camera from the chip endface (mm)				
	44.1	44.5	45.1	45.7	46.2
PE$_{12}$	0.011	-0.013	-0.011	0.027	0.002
PE$_{13}$	-0.023	-0.019	-0.015	-0.029	-0.037
PE$_{14}$	-0.046	-0.048	-0.018	0.011	0.001
CT$_{23}$	-0.048	-0.051	0.003	0.008	0.011
CT$_{34}$	-0.029	-0.044	-0.019	-0.034	-0.049
CT$_{24}$	-0.024	-0.010	0.012	0.015	0.043

Another reason may be that adjusting of the 'matching' distance is very critical, requiring a higher accuracy of the step with which the camera distance is changed. Moreover, for the calculations the channel outputs are approximated as point sources, whereas in reality they have a certain dimension, being 2 μm in this particular case, which causes a spread in spatial frequencies.

Next, different error reduction techniques, which were implemented in the signal analysis software, as described in section 2.3.2, have been tested. To this end, a phase change of 1.5 x 2π was introduced in channel one (0.924% glucose solution). This value of the phase change was chosen because calculations (see section 2.3.1) and experimental results (see section 4.3.1) indicate that the PE and CT values are around their maximum.

Different windows [5-6], like Hanning, Hamming, Blackman, etc., were applied to the original recorded data of the sum interference pattern. The best result was achieved by using the Hamming window, which reduces the PE and CT by a factor of ~ 4 and ~ 1.4, respectively. Applying the technique that increases the frequency resolution, when the number of data points is increased from 512 to 1024, the PE and CT are reduced by a factor of ~ 1.2 and ~ 1.6, respectively. If both techniques are applied simultaneously to the original data, the PE and CT can be reduced by a factor of ~ 3.9 and ~ 1.6, respectively.

In order to apply the matching technique, which aims at the removal of the mismatching effect, the position of each individual spatial frequency in the frequency spectrum is initially estimated. Then the truncation is done such that an integer number of fringes is contained in each individual interference pattern.

Table 4.4 *Measured PE and CT in the four-channel YI when the reduction schemes of windowing, an increase of spatial frequency resolution, and matching are applied separately and in combination with each other.*

PE and CT	No technique	Applied technique				
		Windowing technique	Increasing frequency resolution	Windowing & increase of frequency resolution	Matching of spatial frequencies	Windowing & matching technique
Reduction factor of the PE	1	4	1.2	3.9	1.9	3.5
Reduction factor of the CT	1	1.4	1.6	1.6	2.4	3.5

Applying this technique, the PE and CT can be reduced by a factor of ~ 1.9 and ~ 2.4, respectively, by using 503 original data points out of 512. If the original interference signal is initially resampled to a larger number of data points before the truncation step is applied, the PE and CT appear to be less reduced, as can be ascribed to the error that is introduced by the interpolation process. A better result is achieved by using simultaneously both the matching technique and the Hamming window, which can decrease both the PE and CT by a factor of ~ 3.5. A summary of the PE and CT that result in the four-channel YI when different techniques have been implemented is presented in Table 4.4.

4.3.3 Simultaneous measurement of three different glucose concentrations

In this section, an experiment that shows the possibility to measure different channels simultaneously will be described.

In Figure 4.6.A, the response of the sensor is shown when a phase change of 2π is introduced in channel 1 and 3 and a phase change of $2 \times 2\pi$ is introduced in channel 2 simultaneously, using 0.616% and 1.232% (by weight) glucose solutions. Pure water was continuously flown to channel 4. After a stable signal was reached, the solutions were exchanged for pure water, at first in channel 2, next in channels 3 and 1, as shown in Figure 4.6.A. From the measured values, $\Delta\varphi_{12}$, $\Delta\varphi_{23}$, and $\Delta\varphi_{14}$, the phase change introduced in the channels, $\Delta\phi_1$, $\Delta\phi_2$, and $\Delta\phi_3$ can be determined, e.g. $\Delta\phi_1 = \Delta\varphi_{14} + \Delta\phi_4$, etc. Note that $\Delta\phi_4 = 0$, because no

phase change was introduced in channel 4. The time-dependence of the phase changes are shown in Figure 4.6.B.
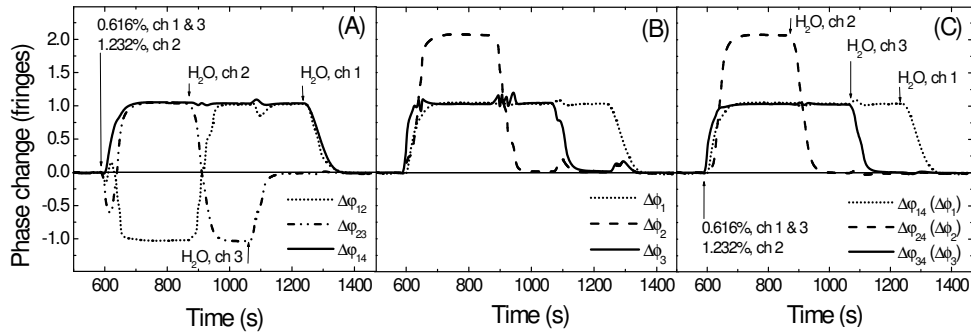
Figure 4.6 *(A) Measured phase changes $\Delta\varphi_{12}$, $\Delta\varphi_{23}$, and $\Delta\varphi_{14}$ as a function of time in the four-channel YI when a phase change of 2π is introduced in channel 1 and 3 and a phase change of $2 \times 2\pi$ in channel 2 simultaneously. (B) Phase changes that occur in channel 1, 2, and 3 ($\Delta\phi_1$, $\Delta\phi_2$, and $\Delta\phi_3$), calculated from measured phase changes $\Delta\varphi_{12}$, $\Delta\varphi_{23}$, and $\Delta\varphi_{14}$. (C) Measured phase changes $\Delta\varphi_{14}$, $\Delta\varphi_{24}$, and $\Delta\varphi_{34}$, which correspond to phase changes occurring in channel 1, 2, and 3, respectively.*

The obtained phase changes nicely correspond to the introduced ones, in that way demonstrating one of the multipurpose features of the multichannel device with which, three different glucose concentrations were measured simultaneously and independently from each other. Alternatively, these channel phase changes can also be determined by using the measured phase changes $\Delta\varphi_{14}$, $\Delta\varphi_{24}$, and $\Delta\varphi_{34}$, as shown in Figure 4.6.C. Results obtained by both ways nicely correspond, highlighting the consistency of the realized device. Fluctuations in the phase signal observed in Figure 4.6 (B and C) are caused by the PE and CT that are present when phase changes introduced in the channels are different from an integer number of fringes (see sections 2.3.1 and 4.3.1).

Figure 4.7 shows the phase difference measured between channels of each pair when no phase change is introduced in any of the channels. The phase resolution ($S/N = 1$) for each pair of channels, as determined from these measurements, is ~ $1 \times 10^{-4} \times 2\pi$, which corresponds to a refractive index resolution of ~ 8.5×10^{-8} (sensing window length of 4 mm) at a bandwidth of 1 Hz.

In Figure 4.8, the measured phase changes $\Delta\varphi_{12}$, $\Delta\varphi_{13}$, and $\Delta\varphi_{14}$ are plotted when glucose concentrations, corresponding with phase changes of 2π and $2 \times 2\pi$, were introduced in channel 1. These values are chosen because at an integer number of fringes, the phase errors are expected to be small.

65
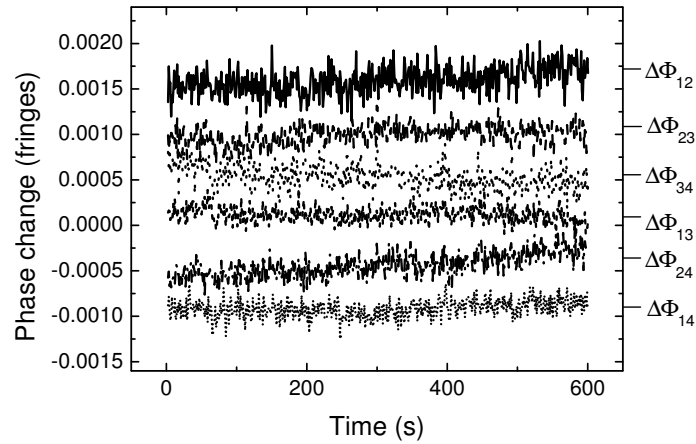
Figure 4.7 *Phase changes measured between two channels of each channel pair in the four-channel YI when no phase change is introduced at the channels. A shift of phase plots along vertical axis is applied to distinguish them from each other.*

The measured phase change for each pair can be nicely fitted to straight lines, which are very close to each other. From the data, a sensitivity coefficient of the phase change vs. refractive index change of $\sim 1.22 \times 10^3 \times 2\pi$ can be derived, being in good accordance with the calculated one of $\sim 1.20 \times 10^3 \times 2\pi$.
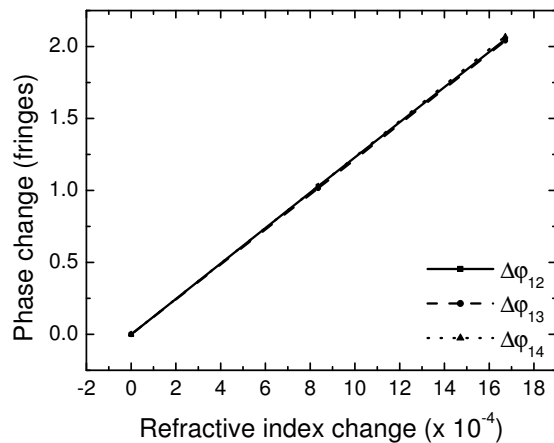

Figure 4.8 *Measured phase changes $\Delta\varphi_{12}$, $\Delta\varphi_{13}$, and $\Delta\varphi_{14}$ vs. the refractive index change when glucose solutions, which correspond to phase changes of 2π and $2 \times 2\pi$, were introduced in channel 1.*

4.4 Discussion and conclusions

Initial measurements performed with the two-channel IO YI sensor have shown a phase resolution of ~ 1 x 10^{-4} x 2π (processing speed of ~ 0.5 Hz), which corresponds to a refractive index resolution of ~ 2 x 10^{-8}, considering a sensing window length of 20 mm. The long-term phase stability was ~ 1 x 10^{-3} x $2\pi \cdot h^{-1}$, corresponding to a refractive index change of ~ 2 x 10^{-7} h^{-1}. This device shows a high refractive index resolution that is comparable with that of the phase-modulated Mach-Zehnder interferometer [7]. It shows a long-term stability comparable with that of the integrated optical YI developed by Brandenburg [8], and a higher resolution compared to the YI sensor realized by Cross et al. [9]. The stability of the two-channel YI device was further improved to ~ 5 x 10^{-4} x $2\pi \cdot h^{-1}$ by implementing windows in both measuring and reference branches; in this way, the environmental changes, as temperature drift, were further reduced. In addition, the processing speed of the interference signal was increased from ~ 0.5 Hz to ~ 25 Hz, which is also the frame rate of the CCD camera used to record the interference pattern. As expected, the phase resolution of the two-channel YI was improved by a factor of ~ 7 to ~ 1.5 x 10^{-5} x 2π (refractive index resolution of ~ 3 x 10^{-9}). This is the highest resolution ever achieved with an interferometric device [7-10].

The resolution achieved with these devices appears not to be limited by the digitation step (A/D converter) applied. This is a result of calculations that are performed by considering the experimental conditions. It is also found that the resolution that can be achieved does not depend on the number of the CCD camera pixels per interference fringe.

Next, it has been shown experimentally that the four-channel YI sensor device can be used to measure three different concentrations of an analyte, such as glucose, simultaneously and independently from each other. In a similar way, this device can be used to monitor three different binding events, e.g. three different immunoreactions, and/or to determine the non-specific binding interactions, as will be shown in chapter 5.

The phase resolution measured for different pairs of channels in the four-channel YI is ~ 1 x 10^{-4} x 2π, which corresponds to a refractive index resolution of ~ 8.5 x 10^{-8}, considering a sensing window length of 4 mm. The long-term stability of the phase change measured for different pairs of channels is ~ 5 x 10^{-4} x $2\pi \cdot h^{-1}$. The measured sensitivity coefficient of the phase change vs. refractive index change, which resulted to be ~ 1.22 x 10^{3} x 2π, is in good accordance with the calculated one of ~ 1.20 x 10^{3} x 2π. The four-channel YI device shows a phase resolution that is ~ 7 smaller compared to the two-channel YI for the same bandwidth.

Initial measurements have shown a good agreement between the response of the four-channel YI sensor and the theoretically calculated one. Corresponding differences in phase changes, the phase errors (PE), were ~ 0.05 x 2π at

maximum, whereas the cross-talk (CT) between different pairs of channels has reached a maximum of ~ 0.035 x 2π, being in good accordance with the calculations presented in section 2.3. Different techniques, such as Hamming window, increase of the spatial frequency resolution, and resampling technique were used to reduce the PE and CT in the four-channel YI. By implementing these techniques separately and in combination with each other, the PE and CT could be reduced by a factor of ~ 3.5.

The experimentally obtained PE and CT reductions were smaller than indicated by the calculations (~ 5). The reason can be found in the presence of spurious fringes in the real interference pattern and/or a nonlinear response of the detector [3-4], which are not present in the calculations. In addition, one has to consider the influence of experimental errors such as drift, misalignment, or any leakage of the flow chambers, which again are not included in calculations. Reminding the experimental errors to be ~ 0.005 x 2π, as concluded in section 4.3.1, the error still caused by the analysis, after the reduction schemes have been applied (~ 0.014 x 2π), is only a factor of ~ 3 more than the experimental error. Note that for phase changes around 0.5 x 2π, the errors are < 3% in the four-channel YI and < 1.5% in the two-channel YI sensor. Considering different immunosensing applications [11], in which the phase changes can be in the order of several fringes, the relative PE and CT will be smaller than 1% in the worst case of phase changes around (N + 0.5) x 2π. For phase changes that approach the device resolution, it appears that the PE and CT are also decreasing.

References

[1]   R.C. Weast, *Handbook of Chemistry and Physics*, 65th ed. (CRC Press, Boca Raton, Fla., 1984-1985), pp. D-234.

[2]   Slab simulation software, C2V, Enschede, The Netherlands.

[3]   S. Nakadate, Phase detection of equidistant fringes for highly sensitive optical sensing. I. Principle and error analysis, J. Opt. Soc. Am. A 5, 1258-1264 (1988).

[4]   M. Kujawinska and J. Wojciak, High accuracy Fourier Transform fringe pattern analysis, Optics and Lasers in Engineering 14, 325-339 (1991).

[5]   F.J. Harris, On the use of windows for harmonic analysis with the discrete Fourier transform, in *Proceedings of IEEE 66* (Institute of Electrical and Electronics Engineers, New York, 1978), pp. 51-83.

[6]   A.H. Nuttall, Some windows with very good sidelobe behavior, *IEEE Transactions on Acoustics, Speech, and Signal Processing 29*, 84-91 (1981).

[7]   R.G. Heideman and P.V. Lambeck, Remote opto-chemical sensing with extreme sensitivity: design, fabrication and performance of a pigtailed integrated optical phase-modulated Mach-Zehnder interferometer system, Sensors and Actuators B 61, 100-127 (1999).

[8]   A. Brandenburg, Differential refractometry by an integrated-optical Young interferometer, Sensors and Actuators B 38-39, 266-271 (1997).

[9]   G.H. Cross, Y. Ren, and N.J. Freeman, Young's fringes from vertically integrated slab waveguides: Applications to humidity sensing, Journal of Applied Physics 86, 6483-6488 (1999).

[10]   G.H. Cross, A.A. Reeves, S. Brand, J.F. Popplewell, L.L. Peel, M.J. Swann, and N.J. Freeman, A new quantitative optical sensor for protein characterization, Biosensors and Bioelectronics 19, 383-390 (2003).

[11]   R.G. Heideman, R.P.H. Kooyman, and J. Greve, Immunoreactivity of adsorbed anti human chorionic gonadotropin studied with an optical waveguide interferometric sensor, Biosensors and Bioelectronics 9, 33-43 (1994).

CHAPTER FIVE

MULTICHANNEL DETECTION OF
VIRUSES AND PROTEINS

The use of a multichannel IO YI as an immunosensor will be reported. The four-channel IO YI immunosensor is used to monitor different analytes simultaneously and independently from each other, and to measure non-specific binding. Up to three different measuring channels are used to monitor proteins and viruses simultaneously and to measure different protein concentrations. The results are in good agreement with predictions for specific interaction with the sensing surface and show low non-specific binding. The experiments demonstrate that the sensor can be used to measure low concentrations of the human simplex virus. Extrapolation of the results shows that even a few virus particles on the sensor surface can be detected.[1]

5.1   Introduction

Various bio-chemical sensing techniques have been developed to perform one or several tasks in different areas of production and monitoring, as well as in the field of research, such as food analysis, health care, environmental monitoring, biotechnology and bioprocess control, life science research, etc. In the last couple of years, there has been a rapid development of highly sensitive optical devices. Such devices often require no label and need less complex sample preparations. Consequently, the costs of a test are low.

Especially integrated optical interference-based devices demonstrate a high resolution with respect to both refractive index changes [1-2] and analyte layer growth when these devices are used for immunosensing applications. The high resolution allows measurement of very small concentrations of analytes in sample solutions, e.g. glucose in a blood sample, etc. In addition, the high resolution can be used to directly measure small molecules, such as pesticides with $M \sim 250$ Da [3], etc.

We have developed an integrated optical immunosensor based on a Young interferometer [2, 4], which shows a very high resolution. The resolution of 10^{-8} refractive index units, corresponding to approximately a protein mass coverage of 30 fg/mm^2, is one of the highest resolutions ever achieved with an interferometric sensor [1, 5]. Compared to other non-labeling sensor techniques, e.g. surface plasmon resonance (SPR) sensors [6], the resolution is roughly 2 orders of magnitude larger.

So far, these types of sensors have been used mainly for the detection of proteins. In this paper, we explore the use of this sensor for the detection of viruses. In this study, we have chosen the Herpes Simplex Virus type 1 (HSV-1). This virus causes recurrent mucosal infections of the eye, mouth, and genital tract. Virus detection is normally realised by a time-consuming procedure that includes culturing and amplification [7]. Although the fast detection of HSV-1 is not clinical relevant, it is used here as a model virus. The principle of the sensor is such that given the proper receptor different, more relevant viruses as HIV, SARS, Hepatitis B and C can be readily detected. In addition, measurements aiming at the detection of proteins that are associated with virus particles, such as HEP G2 (associated with Hepatitis-B), p24 (associated with HIV) are performed.

Furthermore, the current sensor allows determining various analytes simultaneously. We demonstrate this property of the sensor by monitoring simultaneously multiple immunoreactions.

73

5.2   Methods and materials

5.2.1   Theory

In an immunosensor the core-cover interface of an optical waveguide structure is coated with a chemo-optical transducer receptor layer, which can selectively bind to a certain type of analyte molecule present in the cover medium, see Figure 5.1. The receptor-analyte reaction obeys the law of mass action, which states that the rate of a reaction is proportional to the concentration of the reactants. At the equilibrium, the rate of formation of the receptor-analyte complex is equal to the rate of breaking, and the equilibrium constant, K, can be written as

$$K = k_f / k_b = [Re\,An]/[Re] \cdot [An] \tag{5.1}$$

where k_f and k_b are the formation and breaking rate constants and [Re], [An], and [$ReAn$] are respectively the concentration of receptor, analyte, and receptor-analyte complex.
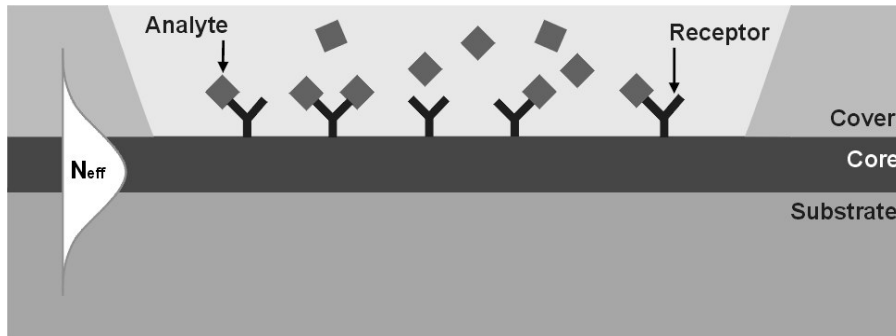

Figure 5.1 *Schematic presentation of a binding event between analyte and receptor molecules taking place at the core-cover interface of a three-layer waveguide structure within the evanescent region of a guided mode; N_{eff} is the effective refractive index of the guided mode.*

The thickness of the layer grown on the sensor surface due to the binding of analyte molecules to the receptor, Δd_l, depends on the receptor density, Γ_0, and the volume of the analyte molecules, V, and it can be written as

$$\Delta d_l \approx \Delta F \cdot \Gamma_0 \cdot V \tag{5.2}$$

where ΔF is the fraction of receptor molecules that have bound an analyte molecule. The maximum fraction of receptor molecules bound to an analyte molecule as a function of concentration of the analyte molecules, C, can be described by the Langmuir isotherm [8]

$$\Delta F_{max} = \frac{KC}{1+KC} \tag{5.3}$$

where K is the equilibrium constant for binding of the analyte molecules to the receptor molecules.

Assuming a linear dependence between refractive index change and mass density of a protein $dn/dC \sim 0.188$ ml/g [9] and taking the refractive index of the protein $n_p \sim 1.45$ [10], the mass coverage change of the protein, $\Delta m/A$, can be calculated as [11]

$$\frac{\Delta m}{A} \left(\frac{ng}{mm^2} \right) \approx 0.6 \cdot \Delta d_l (nm) \tag{5.4}$$

where Δm is the mass change at the surface and A is the surface area. In an interferometric sensor, such as the YI, the thickness of the protein layer grown on the sensor surface can be calculated as

$$\Delta d_l = \frac{\lambda}{l} \left(\frac{\partial N_{eff}}{\partial d_l} \right)^{-1} \cdot \Delta\varphi \tag{5.5}$$

where l is the length of the sensing window, $\partial N_{eff}/\partial d_l$ is the sensitivity coefficient of the effective refractive index of the waveguide with respect to the thickness of the layer grown on the sensor surface, and $\Delta\varphi$ is the phase change caused by layer formation. Last two equations will be used for estimation of the mass coverage of a receptor adsorbed on the sensor surface and the thickness of the analyte layer bound to receptor layer.

The ratio between the number of bound analytes, N_{An}, and the number of receptors adsorbed, N_{Re}, can be derived to be

$$\frac{N_{An}}{N_{Re}} \approx \frac{M_{Re}}{M_{An}} \cdot \frac{\Delta\varphi_{An}}{\Delta\varphi_{Re}} \tag{5.6}$$

where M_{An} and M_{Re} are the molecular weight of analyte and receptor, respectively, whereas $\Delta\varphi_{An}$ and $\Delta\varphi_{Re}$ are the phase changes that result from binding of analyte and receptor, respectively. Evaluation of this quantity yields

information on the quality of the adhered receptor layer, e.g. maximum $N_{An}/N_{Re} = 2$ (receptor can bind maximum 2 analytes).

5.2.2 Materials

The protein A (pA), anti human serum albumine (αHSA, $M \sim 150$ kD), and human serum albumin (HSA, $M \sim 65$ kD) were provided by Paradocs bv (Tiel, The Netherlands). The Herpes Simplex Virus type 1 (HSV-1) and HSV-1 gG Monoclonal Antibody were bought from Virusys Corporation (Marriottsville, MD, USA). The anti human chorionic gonadotropin (αhCG, $M \sim 150$ kD), human chorionic gonadotropin (hCG, $M \sim 40$ kD), bovine serum albumine (BSA, $M \sim 50$ kD), surface protein of HIV capside (p24, $M \sim 24$ kD), monoclonal antibody of class IgG against p24: a-p24-9B (39B, $M \sim 150$ kD), synthetic surface protein of Hepatitis-B virus generated in Hep-G2 cell-line (HEP G2, $M \sim 25$ kD), monoclonal antibody of class IgG against Hepatitis-B surface antigen (46A, $M \sim 150$ kD) were provided by bioMerieux bv (Boxtel, The Netherlands).
The following buffers were used: Phosphate Buffered Saline (PBS, $pH = 7.35$) for αHSA, HSA, HSV-1 gG monoclonal antibody, HSV-1, αhCG, and hCG; phosphate buffer (PB, $pH = 8$) for 39B; NaH_2PO_3 ($pH = 7.5$) for p24; phosphate buffer ($pH = 7.6$) for 46A and HEP G2.

5.2.3 Sensitivity control

The sensitivity of the sensor was first checked by measuring the phase change caused by a refractive index change between a phosphate buffered saline (PBS) solution and di-ionized (DI) water. First, PBS buffer solution was flown in all four sensing windows; after flowing the buffer solution for several minutes, the flow in channel 1 was changed to DI-water. When a stable signal was present, the flow in channel 1 was changed back to PBS solution. The phase changes measured between channel 1 and 2, 1 and 3, and 1 and 4, are in good accordance with the expected one of $\sim 2.22 \times 2\pi$, differing by a maximum of $\sim 0.03 \times 2\pi$, which is within the accuracy of the phase error, see section 4.3. The phase change expected is calculated considering a sensing window length of 4 mm and a refractive index change of $\sim 1.8 \times 10^{-3}$ between PBS solution and DI-water, as measured with an Abbe refractometer.

5.3   Multichannel immunosensing and virus detection

5.3.1   Monitoring anti-human serum albumine – human serum albumine immunoreaction

In this section, use of the IO YI as an immunosensor will be shown. The sensor is used to monitor the anti-human serum albumine – human serum albumine (αHSA - HSA) immunoraction. Figure 5.2 shows the phase change measured between channels 1 and 4 of the four-channel YI when the PBS buffer solution has been continuously flown in channels 2, 3, and 4, while in channel 1 the following steps were applied: first, a PBS buffer solution was flown for ~ 10 minutes. Then the flow was changed to a solution of protein A (pA) prepared in PBS with a concentration of 200 μg/ml. A pA-modified sensing surface is implemented in order to promote the binding and to ensure proper orientation of antibodies for further antigen binding [12-13]. After an equilibrium in the signal was achieved in ~ 10 minutes, indicating the maximum amount of the pA adsorbed, the PBS buffer solution was flown in channel 1 in order to get rid of the bulk refractive index effect. Physical adsorption of pA resulted in a phase change of ~ 0.5 x 2π, which is equivalent to a mass coverage of ~ 0.12 mg/m^2, see Eq. (5.4) and (5.5).
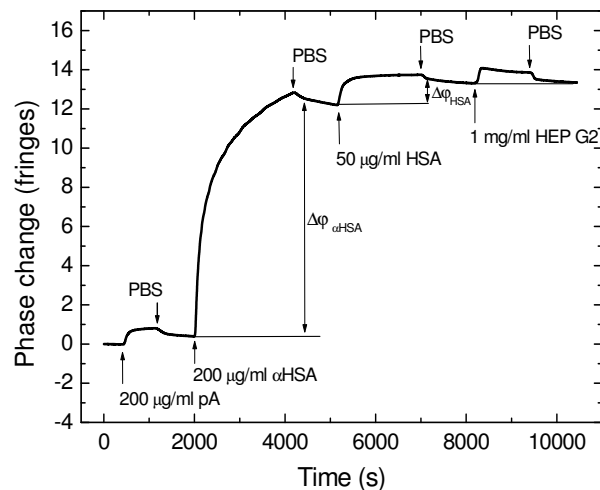

Figure 5.2 *Time-response between channels 1 and 4 in the four-channel YI sensor when the αHSA - HSA immunoreaction is taking place in channel 1 and PBS buffer solution is continuously flown in channel 4.*

77

Next, when a stable base line was achieved in ~ 13 minutes, a concentration of 200 μg/ml solution of αHSA in PBS was flown in channel 1 for ~ 30 minutes, and the flow was changed back to PBS buffer solution to correct for the bulk effect of αHSA. Binding of αHSA resulted in a phase change of ~ 12 x 2π, which corresponds to a mass coverage of ~ 3.1 mg/m^2. Next, after the buffer solution was flown for ~ 10 minutes until a stable signal was achieved, a solution of 50 μg/ml HSA prepared in PBS was applied. Finally, the flow in channel 1 was changed back to PBS solution and the phase change due to antigen layer formation is extracted. Binding of HSA caused a phase change of ~ 1.3 x 2π. The thickness of the bound HSA layer to αHSA molecules is found to be ~ 0.6 nm, see Eq. (5.5), assuming that there is only specific binding and a homogeneous layer is formed. The average number of HSA antigen molecules bound per one αHSA antibody molecule is low (~ 0.25), see Eq. (5.6), indicating that there may be still antibody molecules available for binding. A larger binding in that case can be achieved by increasing the concentration of HSA antigen solutions, until the saturation level is reached, meaning that nearly all the available binding sites in the αHSA layer are occupied by an antigen. If the low number of 0.25 is due to improper orientation of αHSA molecules, then little can be done.

In addition, the specificity of the αHSA - HSA immunoreaction was checked by flowing in channel 1 a high concentration (1 mg/ml) of HEP G2 antigen solution prepared in PBS. After the flow was changed back to buffer solution, no response was observed, indicating that there is no binding of HEP G2. This clearly demonstrates the specificity of αHSA - HSA interaction.

5.3.2   Detection of viruses

Here, the feasibility to use the IO YI sensor for virus detection will be shown. In Figure 5.3, the phase change measured between channels 2 and 4 in the four-channel YI when interaction between HSV-1 gG monoclonal antibody and HSV-1 is taking place in channel 2 and PBS buffer solution is continuously flown in channel 4, is presented. To perform such a test, the sensing surface was treated in the same way as for the measurement of the αHSA - HSA immunoreaction, i.e. by adsorbing protein A (not shown), which will improve the antibody adsorption and its proper orientation for antigen binding. After adsorption of pA in channel 2, a 20 μg/ml HSV-1 gG monoclonal antibody solution prepared in PBS was flown through channel 2 for ~ 30 minutes. Next, PBS was flown in channel 2 for getting rid of the bulk effect followed by application of HSV-1 solution in PBS (concentration not known). Finally, after ~ 30 minutes, PBS was flown again in channel 2. The specificity of this interaction was checked by flowing in channel 2 a 50 μg/ml HSA (not shown in the graph). No response was observed, clearly demonstrating for the specificity of HSV-1 gG – HSV-1 interaction. This test clearly indicates the possibility to use the YI sensor for virus detection. The

adsorption/binding rates of HSV-1 gG antibody and HSV-1 are estimated to be ~ $2 \times 10^{-3} \times 2\pi \cdot s^{-1}$ and HSV-1 is ~$3.6 \times 10^{-4} \times 2\pi \cdot s^{-1}$ respectively, as estimated from the initial slopes in Figure 5.3. This difference may be found in the large size of virus particles (120-200 nm vs. tens of nanometer for HSV-1 antibody), which needs more time to arrive at the sensor surface.
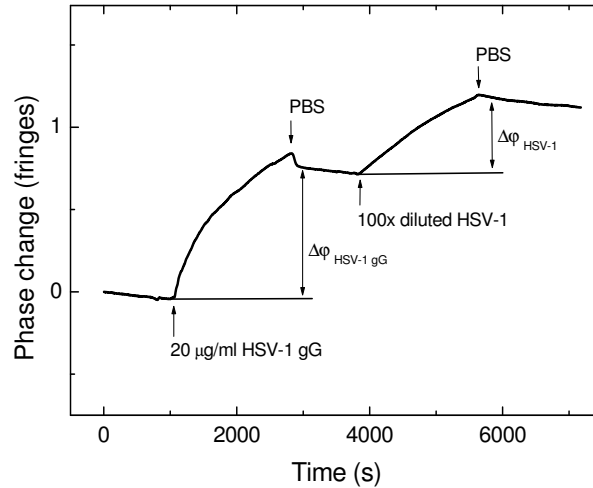

Figure 5.3 *Time-response between channels 2 and 4 in the four-channel YI sensor when interaction between HSV-1 gG monoclonal antibody and HSV-1 is taking place in channel 2 and PBS buffer solution is continuously flown in channel 4.*

Figure 5.4 shows the measurement of HEP G2 protein, which is associated with Hepatitis-B virus. Antibody against this protein (46A) was immobilized by physical adsorption and a postcoating step, using bovine serum albumine (BSA) solution in PBS, was implemented to prevent non-specific adhesion. After binding of HEP G2, the specificity was checked by flowing a solution of p24 and no response was measured, see Figure 5.4.

79
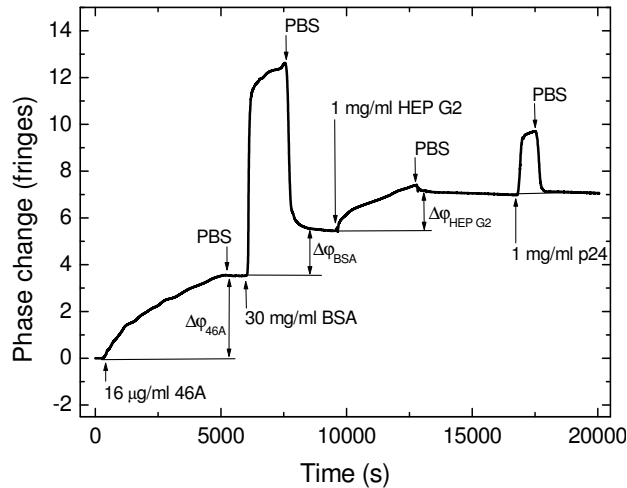
Figure 5.4 *Time-response between channels 1 and 4 in the four-channel YI sensor when interaction between 46A and HEP G2 is taking place in channel 1 and PBS buffer solution is continuously flown in channel 4.*

5.3.3   Simultaneous detection of proteins and viruses

Having demonstrated the possibility to use the IO YI as an immunosensor, in this section the multipurpose feature of the sensor will be shown by monitoring more than one analyte simultaneously. These tests will be performed by immobilizing different receptor layers in different measuring channels.

In Figure 5.5, the phase changes measured for two different channels are plotted. In channel 1, αHSA was immobilized and in channel 2, we immobilized HSV-1 gG monoclonal antibody using pA as an intermediate step similar to the measurements described in section 5.3.1. Next, a 50 μg/ml HSA solution was simultaneously applied in channels 1 and 2 and in ~ 30 minutes, the flow was changed back to PBS buffer for both channels. The observed binding curves are shown in Figure 5.5 (graph A1 and A2 respectively). Figure 5.5 clearly indicates a specific binding of HSA, causing a phase change of ~ 0.61 x 2π. Simultaneously, no response was measured in the HSV-1 gG channel, i.e. no interaction takes place between HSV-1 gG monoclonal antibody and HSA, as expected.

Having achieved once again a stable base line, a solution of HSV-1 in PBS was flown in both channels, see B1 and B2 in Figure 5.5. According to Figure 5.5, there is a phase change of ~ 0.44 x 2π caused by the specific binding of HSV-1 to HSV-1 gG monoclonal antibody in channel 2, and no phase change occurs in channel 1, demonstrating the specific interaction between αHSA and HSA.
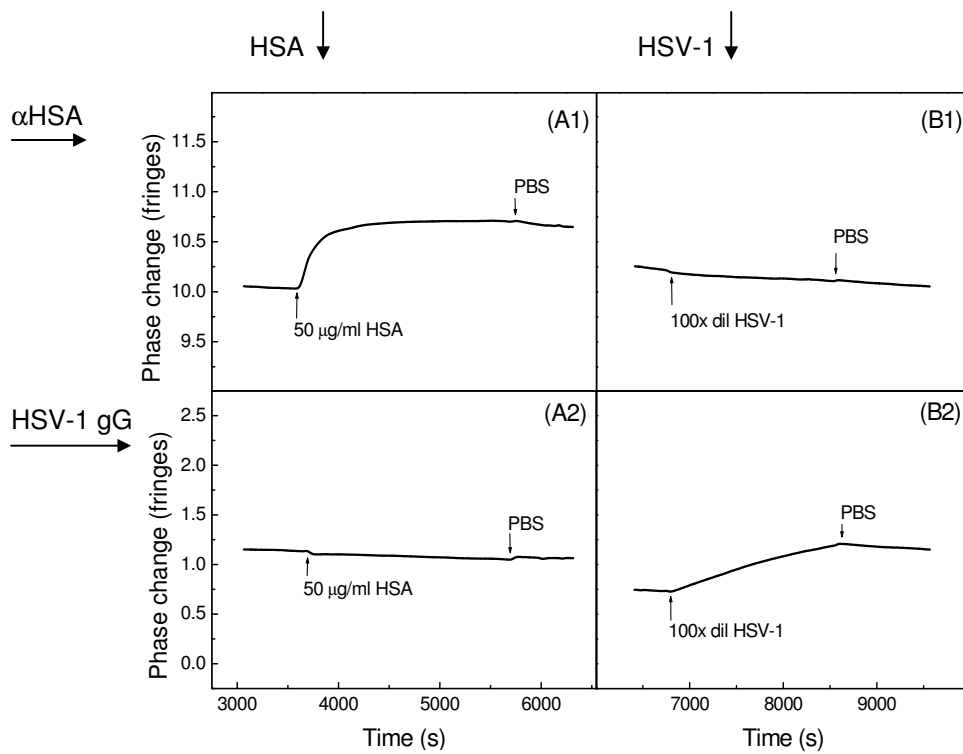
Figure 5.5 *Phase changes measured between channels 1 and 4 and 2 and 4 in the four-channel YI sensor when HSA solution was first flown in channel 1 and 2 simultaneously and after washing with PBS, HSV-1 solution was flown in channels 1 and 2 simultaneously; PBS was continuously flown in channel 4. The four graphs show the following interactions: (A1) αHSA – HSA, (A2) HSV-1 gG monoclonal antibody – HSA, (B1) αHSA – HSV-1, and (B2) HSV-1 gG monoclonal antibody – HSV-1.*

Figure 5.6 presents simultaneous measurement of three different antigens (hCG, p24, and HEP G2), by physically adsorbing in channels 1, 2, and 3 the corresponding antibodies αhCG, 39B, and 46A, respectively, and postcoating with BSA. Interchange of antigen solutions between measuring channels 1, 2, and 3

did not show any binding, demonstrating that αhCG – hCG, 39B – p24, and 46A – HEP G2 interactions are specific.
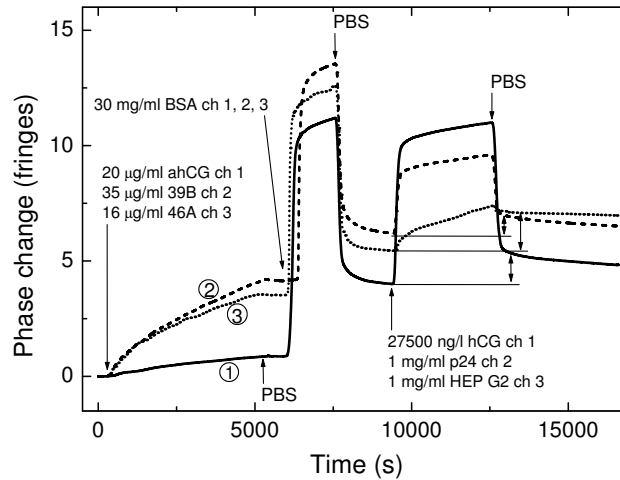
Figure 5.6 *Phase changes measured between channels 1 and 4, 2 and 4, and 3 and 4 in the four-channel YI sensor when αhCG – hCG (solid line), 39B – p24 (dashed line), and 46A – HEP G2 (dotted line) interactions are simultaneously taking place in channels 1, 2, and 3, respectively; PBS buffer solution is continuously flown in channel 4.*

A remark should be made on the large phase changes that result when antigen solutions were flown to the sensing windows, as well as when they were washed. These changes are the result of different buffer solutions in which these antigens were prepared, all having different refractive indices. These effects obviously hamper accurate quantitative analysis of the antigen binding curves.

5.3.4   Simultaneous measurement of different HSA concentrations

Another prospective of the four-channel YI sensor is to measure different concentrations of a given analyte simultaneously. This feature will be demonstrated experimentally by measuring simultaneously different concentrations of HSA, based on which the Langmuir binding curve (see Eq. (5.3)) will be generated. For that purpose, three measuring channels, i.e. channel 1, 2, and 3, were simultaneously coated using a concentration of 200 μg/ml αHSA prepared in PBS (PBS buffer solution was continuously flown in channel 4). Next step consists of simultaneously applying three different concentrations of HSA, i.e. 500 ng/ml, 1 μg/ml, and 5 μg/ml in measuring channel 1, 2, and 3,

respectively. This step was repeated by applying concentrations of 25 µg/ml, 50 µg/ml, and 100 µg/ml, in measuring channel 1, 2, and 3 simultaneously, followed by another set of concentrations (250 µg/ml, 500 µg/ml, and 1 mg/ml). After each set of concentrations has been applied, PBS buffer solution was simultaneously flown in the measuring channels to get rid of the bulk refractive index of HSA solutions applied. Finally, after coating channel 4 using 200 µg/ml αHSA solution, concentrations of 100 ng/ml and 250 ng/ml HSA were applied successively (PBS was flown in all other channels). The phase changes measured for the different HSA concentrations are plotted in Figure 5.7.

The experimentally measured data are fitted with the Langmuir isotherm [8]. According to these measurements, it results that when the concentration of HSA approaches ~ 1 mg/ml (1.5×10^{-5} M), a saturation level is reached, meaning that the antigen molecules already occupy all available binding sites. The total phase change measured due to HSA binding was ~ $1.13 \times 2\pi$, corresponding to a layer thickness of ~ 0.5 nm. The equilibrium constant is estimated to be ~ 3×10^{7} M^{-1}, as extracted from a fitted Langmuir curve shown in Figure 5.7, being in line with previous results [14].
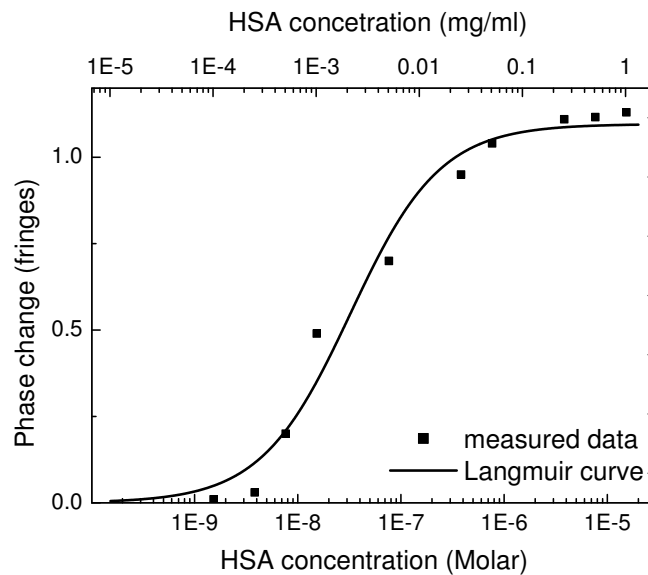

Figure 5.7 *Phase change measured in the four-channel YI for different concentrations of HSA solution. Solid line represents the Langmuir curve fitted to the experimental data.*

5.4   Discussion of the results

Surface treatment/specificity. A pA-modified sensing surface is efficiently used to immobilize antibodies at the Si_3N_4 surface with a surface coverage of ~ 3 mg/m^2 corresponding to values found in literature [12-13]. However, the ratio between the number of bound antigens and the number of antibodies (~ 0.25) is lower than can be expected since theoretically two antigens can bind to one antibody. It should be noted however that the used antigen concentrations are below the saturation value. The use of higher concentrations of HSA yielded slightly better results (ratio ~ 0.3) indicating that there is still room for improvement. In addition, physical adsorption is used for immobilization of antibodies as an alternative to a pA-modified surface. In that case, postcoating with BSA after antibody adsorption is applied to prevent non-specific binding of antigen. The results achieved with this method were less effective concerning the antibody immobilization (~ 1.6 mg/m^2) and specificity. In addition, a signal drift after BSA adsorption was observed, which most likely is due to desorption of BSA from the surface.

In general, it was observed that after the binding step of proteins to the interface a gradual change of the phase is present (see e.g. Figure 5.2 after the αHSA adsorption step). This effect can be explained by desorption of bound molecules not firmly attached. Given the time span used in these experiments, the desorption did not seriously hamper the detection of analytes.

A remark should be made about the analysis of interactions in section 5.3. Here, equilibrium equations as described in section 5.2.1 are used, although interactions in Figure 5.2 and 5.3 do not reach a complete equilibrium state. However, knowing that we are close to equilibrium state, we use approximate values to estimate these interactions.

Virus detection. An estimation of the number of HSV-1 particles that have been detected can be made since the size (120 – 200 nm) and the refractive index (~ 1.41 [15]) of the virus are known. This results in a phase change of ~ 1.1 x 10^{-4} x 2π for the binding of a single virus particle (calculated by assuming that the virus particle occupies the same volume in the evanescent region as a homogeneous layer with the same refractive index). This means that, according to Figure 5.3, during the course of the measurements ~ 4000 virus particles were detected with a rate of 2 viruses/second. From these estimations and the realization that the phase resolution of the four-channel YI device is ~ 1 x 10^{-4} x 2π (see section 4.3), it can be concluded that the detection limit of the sensor is very close to a single HSV-1 particle.

From Figure 5.3 it follows that a long time interval is required to detect the total number of HSV-1 particles bound. However, this does not necessarily limit the speed of virus detection. Since the binding follows zero order kinetics, in principle

one is able to estimate the concentration of the applied virus suspension by only measuring the response of the sensor in the first few minutes.

General. The results obtained in this chapter clearly demonstrate the feasibility to detect low numbers of virus particles using an integrated optical YI. Moreover, it demonstrates the possibility to simultaneously detect different types of analytes (in this case virus particles and proteins), as well as different concentrations of the same analyte, as shown for HSA. In addition, monitoring of proteins associated with HIV and Hepatitis virus indicates an additional way for virus detection.

5.5 Conclusions

In this chapter, the use of the four-channel IO YI device for detection of Human Simplex Virus type 1 particles is demonstrated as a first step towards the detection of more relevant viruses such as HIV, SARS, Hepatitis B and C, etc. It is estimated that the resolution of the four-channel YI device can approach detection of a single virus particle. Furthermore, proteins associated with HIV and Hepatitis-B virus are monitored.

The feasibility to use such a device as an immunosensor is shown by monitoring αHSA - HSA immunoreaction. The specificity of this interaction was checked by flowing a high concentration of HEP G2 solution whereupon no response was measured, clearly indicating the specificity of the αHSA - HSA interaction.

The four-channel YI device is used to monitor more than one analyte simultaneously. Monitoring of αHSA - HSA and HSV-1 gG monoclonal antibody – HSV-1 interactions in channels 1 and 2 simultaneously and independently from each other shows the multipurpose feature of such a device. In the same way, αhCG - hCG, 46A – p24, and 39B – HEP G2 interactions are simultaneously performed in channels 1, 2, and 3. In addition, this device is used to simultaneously measure three different concentrations of HSA. From last measurement, the Langmuir curve is derived and the equilibrium constant is estimated.

Using specific antibody coatings in the different channels, it is possible to detect these analytes specifically. This holds both for proteins as well as for the virus particles. However, in order to be useful in the detection of analytes in a clinical setting, the sensor should also be tested with more complex samples, e.g. a virus suspended in serum. The same holds for proteins associated with HIV and Hepatitis virus.

Combination of the extreme sensitivity with a high sample throughput, brought by the multichannel operation, makes the four-channel IO YI sensor very attractive for different interesting applications in areas such as health care, food analysis, environmental monitoring, etc.

References

[1] R.G. Heideman and P.V. Lambeck, Remote opto-chemical sensing with extreme sensitivity: design, fabrication and performance of a pigtailed integrated optical phase-modulated Mach-Zehnder interferometer system, Sensors and Actuators B 61, 100-127 (1999).

[2] A. Ymeti, J.S. Kanger, R. Wijn, P.V. Lambeck, and J. Greve, Development of a multichannel integrated interferometer immunosensor, Sensors and Actuators B 83, 1-7 (2002).

[3] E.F. Schipper, R.P.H. Kooyman, R.G. Heideman, and J. Greve, Feasibility of optical waveguide immunosensors for pesticide detection; Physical aspects, Sensors and Actuators B 24, 90-93 (1995).

[4] A. Ymeti, J.S. Kanger, J. Greve, P.V. Lambeck, R. Wijn, and R.G. Heideman, Realization of a multichannel integrated Young interferometer chemical sensor, Applied Optics 42, 5649-5660 (2003).

[5] A. Brandenburg, Differential refractometry by an integrated-optical Young interferometer, Sensors and Actuators B 38-39, 266-271 (1997).

[6] C.E.H. Berger, T.A.M. Beumer, R.P.H. Kooyman, and J. Greve, Surface plasmon resonance multisensing, Anal. Chem. 70, 703-706 (1998).

[7] A.C. Minson, Alphaherpesviruses: herpes simplex and varicella zoster virus infections. In *Topley and Wilson's microbiology and microbial infenctions,* Vol. 1, Edn. 9 (eds Mahy, B. & Collier, L.) 325-339 (Arnold, London; 1998).

[8] J.D. Antrade, *Principles of protein adsorption. In surface and interfacial aspects of biomedical polymers*, vol 2 (Plenum Press, New York, 1985).

[9] J.A. de Feijter, J. Benjamins, and F.A de Veer, Ellipsometry as a tool to study the adsorption behavior of synthetic and biopolymers at the air-water interface, Biopolymers 17, 1759-1772 (1978).

[10] R.G.C. Oudshoorn, R.P.H. Kooyman, and J. Greve, Refractive index and thickness of an adsorbing protein as reporters of monolayer formation, Thin Solid Films 285, 836-840 (1996).

[11] E.F. Schipper, Waveguide immunosensing of small molecules, Ph.D. Thesis, University of Twente, The Netherlands, 1997.

[12] K. Owaku and M. Goto, Optical Immunosensing for IgG, Sensors and Actuators B 13-14, 723-724 (1993).

[13] L. Bin, M.R. Smyth, and R. O'Kennedy, Oriented immobilization of antibodies and its applications in Immunoassays and Immunosensors, The Analyst 121, 29R-32R (1996).

[14] R.G. Heideman, R.P.H. Kooyman, and J. Greve, Immunoreactivity of adsorbed anti human chorionic gonadotropin studied with an optical waveguide interferometric sensor, Biosens. Bioelectron. 9, 33-43 (1994).

[15] W.M. Balch, J. Vaughn, J. Novotny, D.T. Drapeau, R. Vaillancourt, J. Lapierre, and A. Ashe, Limnol. Oceanogr. 45(2), 492–498 (2000).

CHAPTER SIX

DRIFT CORRECTION
IN THE MULTICHANNEL IO YI
FOR SENSING APPLICATIONS

In this chapter it will be demonstrated that in a sensor based on a multichannel YI, the phase information obtained for different pairs of channels can be used to correct the long-term instability (drift) due to temperature differences between measuring and reference channels, drift in the alignment of the set-up, etc. Experimental tests show that by using such a drift-correction method, the phase change due to the drift can be reduced ~ 10 times as compared to the situation when no correction is applied. This means in practice that the total measuring time may be extended 10 times still allowing for the same total drift.[1]

---

[1] To be published as:

A. Ymeti, J.S. Kanger, J. Greve, P.V. Lambeck, R. Wijn, and R.G. Heideman, Drift correction in a multichannel integrated optical Young interferometer for sensing applications, to be submitted.

6.1   Introduction

Integrated optical sensors, especially interferometric ones, such as the YI [1-2] the MZI [3], etc., are becoming increasingly sensitive thanks to optimization and improvement of the waveguide structure parameters. These sensors show an extremely high refractive index resolution [2-3] being in the order of ~ 10^{-8}, which is equivalent to a protein mass coverage of ~ 30 fg/mm^2. Using such sensitive sensors it is possible to measure very low concentrations of an analyte in solution when it is applied in the measuring window of the interferometer device. However, monitoring of a binding event, such as an immunoreaction, requires a long time. In that case, the resolution of these devices is limited by the drift, which may be caused by temperature differences between reference and measuring channels, drift in the alignment of the set-up, etc. Although the measuring and reference channels are usually positioned relatively close to each other, a temperature drift cannot be completely avoided. The same holds for drift in the alignment of the set-up. As a consequence, the long-term stability (hours) of these devices, e.g. with respect to a refractive index change, may be up to one order of magnitude smaller [1-3] as compared to the short-term stability (minutes). Especially in the case of monitoring low analyte concentrations and/or low surface coverage of molecules that require a high resolution, the drift strongly hampers high resolution and extremely accurate measurements.

Here, a method will be presented to reduce the drift. A multichannel IO YI device (schematically presented in Figure 2.4), which was fabricated in SiON technology [4-6], has been used to experimentally test such a method. The design and fabrication of such a device are described in detail in chapter 3.

If a given phase change is introduced by a change in refractive index in one of the channels, e.g. channel 2, the phase change occurs for all channel pairs that involve channel 2 [2, 7], as concluded in chapter 2 and experimentally shown in chapter 4. In addition, temperature differences between channels, drift in the alignment of the set-up, etc., introduce extra phase changes for each pair of channels. The phase change information measured for all pairs of channels can be used to determine the refractive index change introduced in channel 2, and in the same time, to correct for the contribution due to temperature differences between channels, drift in the alignment of the set-up, etc.

89

6.2 Description of the method

The correction method is based on the assumption that the ratio of the phase deviations for each two pairs of channels due to the drift remains constant during a measurement, which may take several minutes to one hour. Based on this assumption and considering only channels 1, 2, and 3 of the four-channel YI sensor, the following relations can be derived

$$\frac{\Delta\Phi_{12}^{drift}}{\Delta\Phi_{13}^{drift}} = C_{12,13}$$

$$\frac{\Delta\Phi_{23}^{drift}}{\Delta\Phi_{13}^{drift}} = C_{23,13}$$

(6.1)

where $C_{12,13}$ and $C_{23,13}$ are constants and $\Delta\Phi_{12}^{drift}$, $\Delta\Phi_{23}^{drift}$, and $\Delta\Phi_{13}^{drift}$ are the phase changes caused by the drift between channels 1 and 2, 2 and 3, and 1 and 3, respectively. On the other hand, when a refractive index change (signal) is introduced in channel 2, the phase changes measured between channels $\Delta\Phi_{12}^{meas}$, $\Delta\Phi_{23}^{meas}$, and $\Delta\Phi_{13}^{meas}$ can be written as

$$\Delta\Phi_{12}^{meas} = \Delta\Phi_{12}^{signal} + \Delta\Phi_{12}^{drift}$$

$$\Delta\Phi_{23}^{meas} = \Delta\Phi_{23}^{signal} + \Delta\Phi_{23}^{drift}$$

$$\Delta\Phi_{13}^{meas} = \Delta\Phi_{13}^{drift}$$

(6.2)

where $\Delta\Phi_{12}^{signal}$ and $\Delta\Phi_{23}^{signal}$ are respectively the phase changes between channel 1 and 2, and 2 and 3 due to the refractive index change introduced in channel 2. Combining Eq. (6.1) and Eq. (6.2), one can determine the drift-corrected phase changes $\Delta\Phi_{12}^{signal}$ and $\Delta\Phi_{23}^{signal}$ introduced by the refractive index change in channel 2.

6.3   Results

Figure 6.1.A shows the phase change between channels 1 and 2, $\Delta\Phi_{12}^{meas}$, 2 and 3, $\Delta\Phi_{23}^{meas}$, and 1 and 3, $\Delta\Phi_{13}^{meas}$, in the multichannel YI, as measured in one hour. No refractive index change was introduced at any of the channels; pure water was continuously flown onto the sensing window of each channel to approach the conditions of a real measurement.
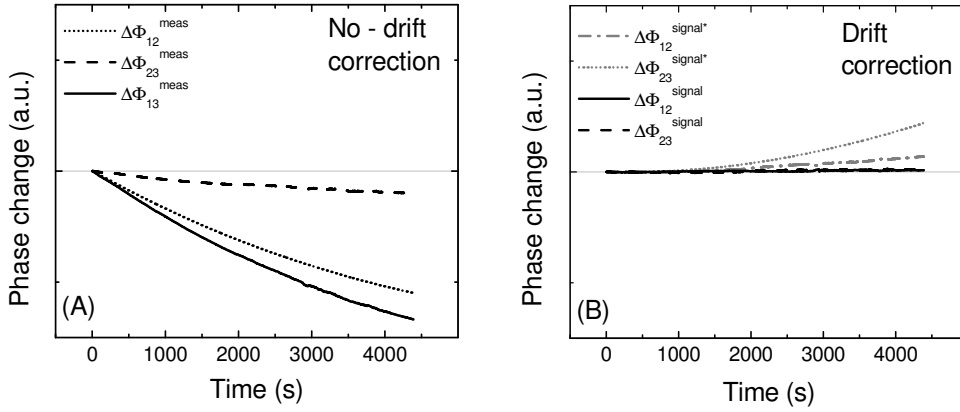

Figure 6.1 *(A) Phase changes $\Delta\Phi_{12}^{meas}$, $\Delta\Phi_{23}^{meas}$, and $\Delta\Phi_{13}^{meas}$ observed in the multichannel IO YI when no refractive index change is introduced in the channels; pure water is continuously flown onto the sensing window of each channel. (B) Drift-corrected phase change between channels 1 and 3 and channels 2 and 3 determined from $\Delta\Phi_{13}^{meas}$: $\Delta\Phi_{12}^{signal}$ and $\Delta\Phi_{23}^{signal}$ were obtained using drift correction method; $\Delta\Phi_{12}^{signal*}$ and $\Delta\Phi_{23}^{signal*}$ were obtained assuming a linear change of the phase due to the drift; vertical scale in both graphs is the same.*

Since no refractive index change and/or binding event was taking place in any of the channels, the phase changes that result for each channel pair are caused only by influence of the factors such as change in temperature difference between channels, etc. From the measurements, $C_{12,13}$ and $C_{23,13}$ were determined by rationing the corresponding phase graphs followed by averaging over the first 10 minutes. Using Eq. (6.1) and Eq. (6.2), the signals $\Delta\Phi_{12}^{signal}$ and $\Delta\Phi_{23}^{signal}$ were calculated (in this particular case both signals should be equal to zero). In Figure

6.1.B, the drift-corrected phase changes, $\Delta\Phi_{12}^{signal}$ and $\Delta\Phi_{23}^{signal}$, are shown. These graphs clearly indicate that this method works over long time scales. In the same graph are also shown phase changes that were corrected by using an alternative technique: considering a drift-induced linear change of the phase difference for each channel pair, and correcting afterwards the phase changes measured with the calculated ones based on the linear behavior that was determined during an initial time interval of several minutes. According to Figure 6.1.B, it is clear that the latter correction method gives a much poorer result. These promising results are related with the fact that the phase changes simultaneously measured for different pairs of channels in the multichannel YI are correlated with each other such that their ratio remains constant in time, as confirmed by the measurements.

As a further test, the drift-correction method was applied to a measurement in which a refractive index change was introduced in one of the channels. In Figure 6.2.A, the response of the sensor to a phase change of ~ 1.5 x 2π introduced by flowing in channel 2 a 0.924% (by weight) solution of glucose in water [8] is presented. Pure water was continuously flown into channel 1 and 3. In the same graph, the drift-corrected phase changes between channels 1 and 2, $\Delta\Phi_{12}^{signal}$,

and 2 and 3, $\Delta\Phi_{23}^{signal}$, obtained by using the drift-correction method, are shown.

The phase change measured between channels 1 and 3 is caused by the presence of the drift, $\Delta\Phi_{13}^{drift}$ only, because no refractive index change was introduced in channel 1 or 3. The ratios $C_{12,13}$ and $C_{23,13}$ were determined based on the phase changes measured before the refractive index change was introduced in channel 2.

According to Figure 6.2.A, the phase change due to the drift, still present after correction, is ~ 10 times smaller compared to a situation when no correction is applied for $\Delta\Phi_{12}$ and $\Delta\Phi_{23}$. Figure 6.2.B shows the sum of the phase changes for channel pairs 12 and 23 prior to and after application of the drift-correction method. The sum of $\Delta\Phi_{12}^{signal}$ and $\Delta\Phi_{23}^{signal}$ results to be nearly zero after the correction is applied, as expected for the multichannel YI device (see chapter 2 and 4). Fluctuations in the phase change signal in Figure 6.2.B are caused by the presence of the phase error and cross-talk when the phase change introduced in the channels is different from an integer number of fringes, as indicated in chapters 2 and 4.
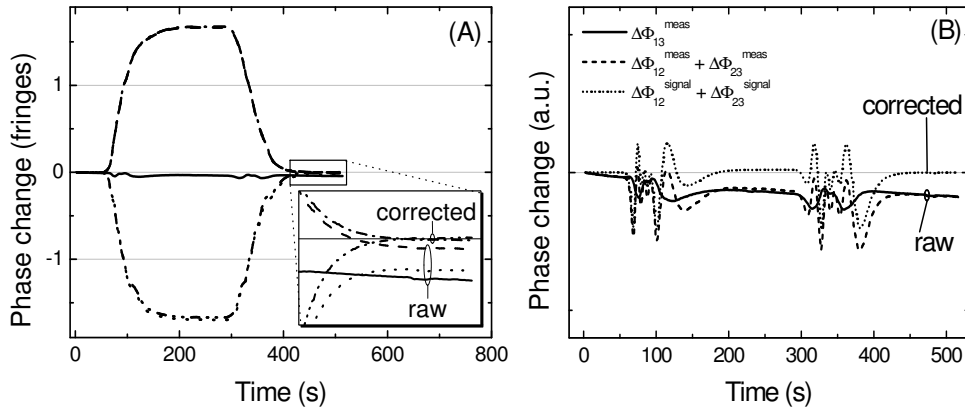
Figure 6.2 *(A) The response of the multichannel IO YI sensor to a phase change of 1.5 x 2π introduced by flowing in channel 2 for ~ 300 s a 0.924% (by weight) glucose solution; $\Delta\Phi_{12}^{signal}$ (dash-dot-dot line) and $\Delta\Phi_{23}^{signal}$ (dash-dot line) are the drift-corrected phase changes based on $\Delta\Phi_{12}^{meas}$ (dot line), $\Delta\Phi_{23}^{meas}$ (dash line), and $\Delta\Phi_{13}^{meas}$ (solid line); the inset presents in detail the phase baselines prior and after the correction. (B) Sum of phase changes $\Delta\Phi_{12}$ and $\Delta\Phi_{23}$ prior to (dash line) and after (dot line) application of the drift-correction method.*

This improvement was also obtained when the refractive index change was introduced in channel 1 or 3 (not shown). These experimental results clearly indicate that in a multichannel IO YI sensor, the drift can be strongly reduced.

6.4 Conclusions

This chapter shows that in a multichannel integrated optical YI it is possible to correct for phase changes due to the temperature differences between measuring and reference channels, and other sources. This drift in the phase decreases by a factor of ~ 10 when the new drift-correction method is applied. Implementation of this correction technique is possible because of the unique properties of the multichannel integrated YI, designed such that the phase change for each possible channel pair can be measured.

93

References

[1]   A. Brandenburg, Differential refractometry by an integrated-optical Young interferometer, Sensors and Actuators B 38-39, 266-271 (1997).

[2]   A. Ymeti, J.S. Kanger, R. Wijn, P.V. Lambeck, and J. Greve, Development of a multichannel integrated interferometer immunosensor, Sensors and Actuators B 83, 1-7 (2002).

[3]   R.G. Heideman and P.V. Lambeck, Remote opto-chemical sensing with extreme sensitivity: design, fabrication and performance of a pigtailed integrated optical phase-modulated Mach-Zehnder interferometer system, Sensors and Actuators B 61, 100-127 (1999).

[4]   K. Wörhoff, P.V. Lambeck, N. Albers, O.F.J Noordman, N.F. van Hulst, and T.J.A. Popma, Optimization of LPCVD Silicon onxynitride growth to large refractive index homogeneity and layer thickness uniformity, Proc. SPIE 3099, 257-268 (1996).

[5]   K. Wörhoff, A. Driessen, P.V. Lambeck, L.T.H. Hilderink, P.W.C. Linders, and T.J.A. Popma, Plasma enhanced chemical vapour deposition of silicon oxynitride optimized for application in integrated optics, Sensors and Actuators B 74, 9-12 (1999).

[6]   K. Wörhoff, L.T.H. Hilderink, A. Driessen, and P.V. Lambeck, Silicon oxynitride - A versatile material for integrated optics applications, Journal of the Electrochemical Society 149 (8): F85-F91 (2002).

[7]   A. Ymeti, J.S. Kanger, J. Greve, P.V. Lambeck, R. Wijn, and R.G. Heideman, Realization of a multichannel integrated Young interferometer chemical sensor, Applied Optics 42, 5649-5660 (2003).

[8]   R.C. Weast, *Handbook of Chemistry and Physics*, 65th ed. (CRC Press, Boca Raton, Fla., 1984-1985), pp. D-234.

CHAPTER SEVEN

INTEGRATION OF MICROFLUIDICS WITH A FOUR-CHANNEL IO YI IMMUNOSENSOR

This chapter describes an optical sensing hybrid system obtained by bonding a microfluidic system to an IO four-channel YI chip. The microfluidic system is structured in such a way that after bonding to the IO chip each microchannel addresses one sensing window in the four-channel YI sensor. Experimental tests show that the implementation of the microfluidics reduces the response time of the sensor by a factor of ~ 20 as compared to a bulky cuvette. As a result, in an immunoreaction a better discrimination between the refractive index change of the sample solution and the layer formation can be made, resulting into higher accuracy and offering the prospect of being able to use the kinetics of the immunoreaction. [1]

7.1   Introduction

There is a high need for highly sensitive multichannel sensors which are required to measure various types of analytes for different areas of applications, as e.g. health care, food industry, etc. Interference-based IO sensors such as the MZI [1] and the YI [2-5] are among the most sensitive devices reported, being able to detect refractive index changes as small as ~ 10^{-8} [1, 3, 5]. This corresponds to a protein concentration of ~ 5.3 x 10^{-8} g/ml (assuming $\partial n/\partial c$ ~ 0.188 ml/g [6]). The high sensitivity, combined with a fast and accurate measurement, makes these devices very attractive, e.g. for point-of-care testing and medical screening.

In order to perform a measurement with an interferometric device, it is necessary to bring the sample solutions to the sensing windows of these devices. Often for that purpose, bulky cuvette systems are used [1-3]. These cuvettes can be made from different materials such as Teflon [1], Perspex [3], etc., and are mounted on the IO chip in various ways, e.g. by pressing or gluing them to the sensor. A drawback of these cuvette systems is the large response time, up to several minutes, due to mixing between sample solutions that are successively applied to the sensing window and/or slow replacement of surface layer, being both mainly due to the relatively large volume of the cuvette flow chambers (~ 6 µl [3]). In addition, relatively large volumes of the samples to be monitored are needed.

Microfluidics [7] has been successfully implemented in various sensing platforms, e.g. in a surface plasmon resonance sensor [8], evanescent wave absorption based sensing [9], etc. The use of microfluidics for sensor applications has several advantages: (i) it strongly reduces the mixing time between sample solutions resulting in a fast response of the sensor, (ii) it enables the use of small sample volumes, (iii) it can readily be integrated with the sensor, resulting in a compact sensing system.

In this paper, we report about the integration of microfluidics and an interferometric sensor into a four-channel IO YI sensor developed recently in our laboratory [3, 5] and demonstrate its usefulness in immunosensing applications. Using microfluidics, the effect of changes in solution on the refractive index can be well separated from those due to layer formation in an immunoreaction, resulting in a better-controlled experiment and a more accurate result. In addition, exposure of the active sensor area to a contaminated environment will be avoided.

In section 7.2, we describe the design and fabrication of the microfluidics and optical chips into one single integrated device. In section 7.3, we will show experimental results illustrating the advantages of these sensors. Conclusions of this work will be presented in section 7.4.

7.2 Design and fabrication

The layout of the microfluidic system and the optical chip in mutual alignment is shown in Figure 7.1.
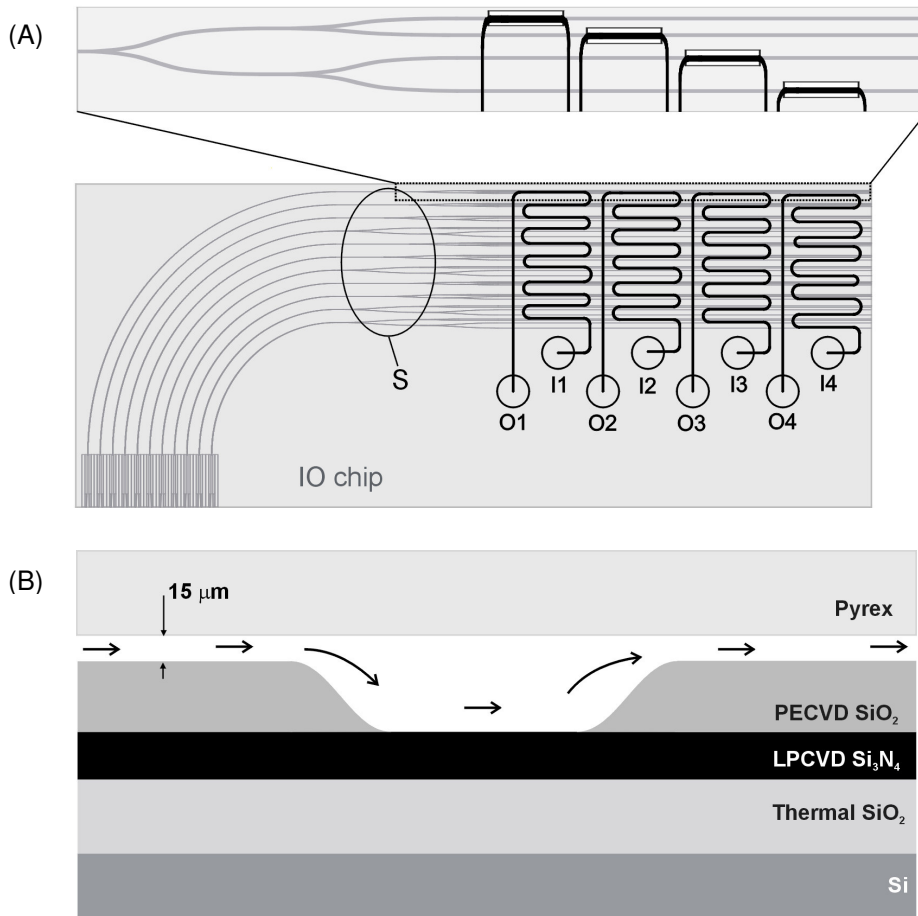
Figure 7.1 *Top-view (A) and cross-section along one of sensing windows (B) of the microfluidic system aligned on a four-channel IO YI chip. The optical chip contains configurations of sensor structure 1, 2, and 3, as defined in chapter 3, which have different distances between their output channels, resulting in a different length of splitting function, manifested by different starting positions of the first Y-junction (see S in A). Ii and Oi indicate the input and output respectively of channel i, addressing the ith bundle of sensing windows. Dimensions of the microfluidic sensing system are 63 mm x 24 mm.*

The optical chip contains 11 four-channel YI structures positioned parallel to each other. A detailed description of the design and fabrication of this four-channel IO YI chip is given in chapter 3. Note that the interaction length of each sensor is 4 mm. The layout of the microfluidic system is adapted to the layout of the optical chip. The microfluidic system is a glass plate (Pyrex wafer with a thickness of ~ 525 μm) in which four meander-like microchannels have been implemented. The channels are ~ 200 μm wide, ~ 15 μm deep, and ~ 90 mm long. Each channel passes a bundle of 11 sensing windows, each being part of a different YI structure in the optical chip. In the glass plate, holes with diameter Ø ~ 2.5 mm are drilled for connection of the channels with the outside world. The distance between two holes (center-to-center) is chosen ~ 3.5 mm.

The channel structure was realized by means of wet etching technique using a 5% hydrochloric fluoride (HF) solution. The holes were realized by powderblasting. For attaching the microfluidic channel system to the optical YI chip, we first tested anodic bonding. For that purpose, we performed test experiments, which involve Silicon wafers provided with the same $SiO_2/Si_3N_4/SiON$ layer stack as our samples [5]. Because the results of these anodic bonding experiments were not satisfactory, it was investigated to glue the optical chip to the microfluidic chip. For this, an UV-curable glue was applied in such a way that no glue is present inside the fluidic channels and on the sensing windows. The glue consists of pure isobornyl acrylate to which dimethoxyfenylacetophenone (DMPA) was added (3.84% w/v). For a detailed description of the gluing procedure, we refer to Schlautmann et al. [8].

Figure 7.2 shows two close-view micrographs of the microfluidic channels.
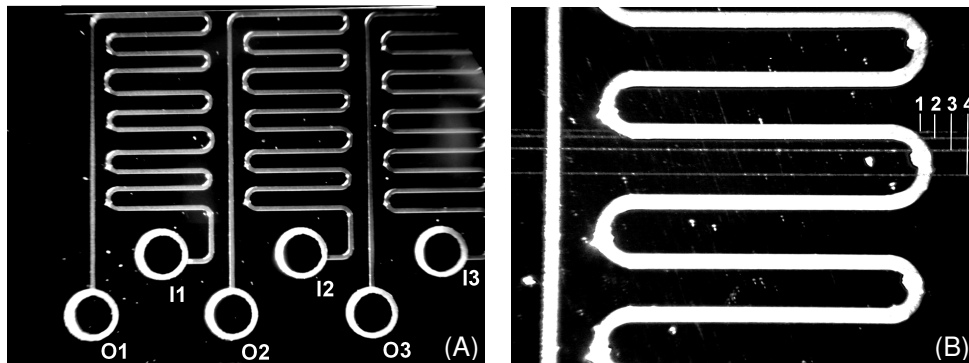
Figure 7.2 *(A) Close-view micrograph of microfluidic channel 1, 2, and 3; (B) close-view micrograph showing the light propagating through the four waveguide channels and the microfluidic channel 2 addressing the sensing window of the waveguide channel 2.*

99

7.3 Experimental results

Figure 7.3 shows the response of the microfluidic sensing system to a phase change of 0.5 x 2π introduced in measuring channel 1 of the fifth YI structure from the top (see Figure 7.1.A) by replacing demi-water by a 0.308% (by weight) glucose solution [10]. The same figure also shows the response of the sensor in case our bulky cuvette is used [5], as well as the response using this cuvette when an air bubble is introduced as a plug in between both two flowing liquids in order to prevent their mixing.

From Figure 7.3, it can be concluded that the time interval required to obtain a stable base line after introducing the glucose solution, is decreased from ~ 100 s in case of the normal cuvette to ~ 4 s in case the microfluidic system is used. In addition, the required sample volume (~ 1 μl) is roughly three orders of magnitude smaller compared to the volume required in case of the normal cuvette (~ 1 ml) for the same flow speed of ~ 3 cm/s. For different flow speeds, the absolute volume required will be different.

The microfluidic sensing system has also been applied to monitor the anti-human serum albumine – human serum albumine (αHSA - HSA) immunoreaction. Figure 7.4 presents the phase changes that occur upon binding of HSA to αHSA immobilized onto the measuring channel.
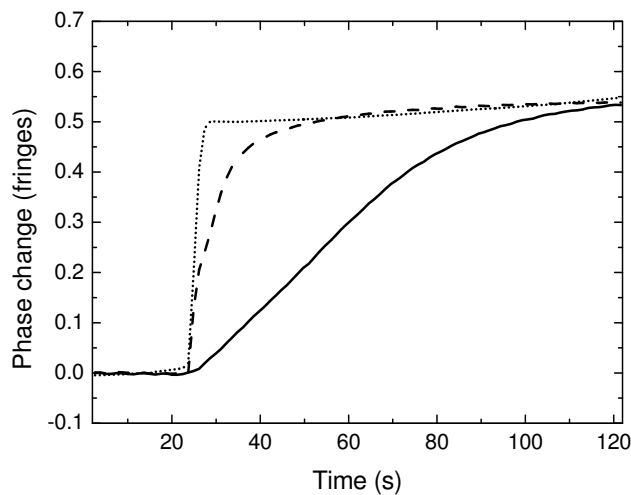

Figure 7.3 *The response of the YI sensing system to a π - phase-change introduced by substituting the demi-water in measuring channel 1 of the fifth YI structure from the top (see Figure 7.1.A) by a 0.308% (by weight) glucose solution using a bulky cuvette (solid line), a bulky cuvette with an air bubble (dashed line), and the microfluidic system (dotted line).*

The sensing protocol for this immunoreaction consists of three steps. Firstly, adsorption of protein A (pA) on the sensor surface by flowing a 200 µg/ml solution of pA in phosphate buffered saline (PBS, pH = 7.35) through the channel.
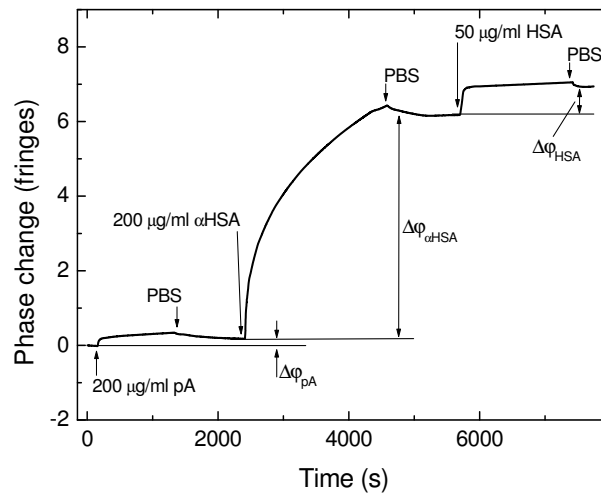
Figure 7.4 *Phase change measured using the microfluidic sensing system when αHSA - HSA interaction is taking place in the measuring channel.*

Application of the pA allows proper orientation of the antibody molecules for antigen binding [11-12]. Secondly, the antibody was bound to the pA-modified surface by flowing a 200 µg/ml solution of αHSA prepared in PBS through the channel. Finally, a 50 µg/ml solution of HSA in PBS was applied to allow binding of HSA molecules. After each step, a washing with PBS was performed in order to remove loosely bound protein molecules and to get rid of the bulk refractive index effect. The phase changes caused by αHSA adsorption (~ 6 x 2π) and binding of HSA (~ 0.8 x 2π) are in line with earlier results, see chapter 5 and [13]. This experiment demonstrates the feasibility to use the YI sensor in combination with a microfluidic cuvette for immunosensing applications.

The reduction of response time can also be observed by analyzing the process during addition of PBS after the third step in more detail, see Figure 7.5.
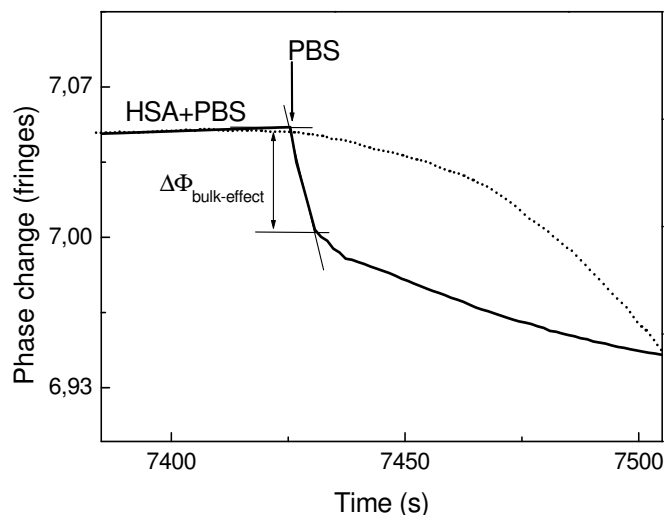
***Figure 7.5*** *Time-responses measured with a bulky cuvette (dotted line) and microfluidic system (solid line) when the HSA solution in the measuring channel was substituted by a PBS buffer solution at the indicated time (arrow). $\Delta\Phi_{bulk\text{-}effect}$ indicates the phase change due to the difference in bulk refractive index between HSA solution and PBS solution.*

The curve obtained with the microfluidics shows a fast phase drop (~ 5 s) followed by a slower decrease. The initial drop is due to the difference in refractive indices between HSA solution and PBS (referred to as the bulk effect). The slower decrease presumably arises from a gradual desorption of proteins from the sensor surface. Using bulky cuvettes, bulk effects extend over much longer times (see Figure 7.5). This normally hampers quantitative determination of reaction rates from data obtained for an immunoreaction because the value of the bulk effect cannot easily be extracted from the data if the time response of the sensor is comparable with the time scale of the bioreaction. However, with the use of microfluidics it is now possible to accurately determine the phase change of the bulk effect, making these types of sensors even more accurate.

Application of the microfluidic system appears not to influence the short-term phase resolution, being ~ 7 x 10^{-5} x 2π and ~ 1 x 10^{-4} x 2π [5] for the sensing system with, respectively without the microfluidic system. Taking into account the value of interaction length (4 mm), this corresponds to a refractive index resolution of ~ 6 x 10^{-8}, which is equivalent to a protein mass coverage resolution of ~ 20 fg/mm^2.

7.4   Conclusions

A microfluidic system was designed, fabricated, and mounted to a four-channel IO YI sensor chip. The microfluidic system consists of a Pyrex wafer in which four microchannels with cross-sectional dimensions of 200 μm x 15 μm have been implemented, each of them addressing a set of 11 sensing windows one in each of the four-channel YI structures realized on top of a Silicon chip. The microfluidic system was bonded to the optical YI chip by means of a gluing technique.

It is shown that the response time needed to achieve a stable signal at replacing demi-water by a glucose solution corresponding to a π – phase change is ~ 4 s, implying a drastically reduced value when compared to that achieved by using a bulky cuvette (~ 100 s). The improved result can be due to a strong reduction of mixing between both sample solutions and/or a faster replacement of surface layer because of a turbulent flow that may occur. Further investigation is needed to better explain this process. In addition, the volume of the sample solution required to perform an immuno-test is two to three orders of magnitude smaller than that using a bulky cuvette-based system. The monitoring of the αHSA - HSA immunoreaction shows that by using a microfluidic system, a better discrimination between bulk effects, due to refractive index difference of both solutions, and the layer formation, can be made. This expectedly will result into higher accuracy and offers the prospect of investigating or using the kinetics of the immunoreaction.

The combination of the microfluidic system with the highly sensitive multichannel YI sensor is a very attractive system, which can be effectively used in medical screening, food analysis, etc., as a new lab-on-a-chip configuration.

Acknowledgements

103

References

[1]   R.G. Heideman and P.V. Lambeck, Remote opto-chemical sensing with extreme sensitivity: design, fabrication and performance of a pigtailed integrated optical phase-modulated Mach-Zehnder interferometer system, Sensors and Actuators B 61, 100-127 (1999).

[2]   A. Brandenburg, Differential refractometry by an integrated-optical Young interferometer, Sensors and Actuators B 38-39, 266-271 (1997).

[3]   A. Ymeti, J.S. Kanger, R. Wijn, P.V. Lambeck, and J. Greve, Development of a multichannel integrated interferometer immunosensor, Sensors and Actuators B 83, 1-7 (2002).

[4]   G.H. Cross, A.A. Reeves, S. Brand, J.F. Popplewell, L.L. Peel, M.J. Swann, and N.J. Freeman, A new quantitative optical sensor for protein characterization, Biosensors and Bioelectronics 19, 383-390 (2003).

[5]   A. Ymeti, J.S. Kanger, J. Greve, P.V. Lambeck, R. Wijn, and R.G. Heideman, Realization of a multichannel integrated Young interferometer chemical sensor, Applied Optics 42, 5649-5660 (2003).

[6]   J.A. de Feijter, J. Benjamins, and F.A. de Veer, Ellipsometry as a tool to study the adsorption behavior of synthetic and biopolymers at the air-water interface, Biopolymers 17, 1759-1772 (1978).

[7]   J.M. Ramsey and A. van den Berg, *Micro Total Analysis Systems* (Kluwer, Dordrecht, 2001).

[8]   S. Schlautman, G.A.J. Besselink, R. Prabhu, and R.B.M Schasfoort, Fabrication of a microfluidic chip by UV bonding at room temperature for integration of temperature sensitive layers, Journal of Micromechanics and Microengineering 13, 81-84 (2003).

[9]   G. Pandraud, T.M. Koster, C. Gui, M. Dijkstra, A. van den Berg, and P.V. Lambeck, Evanescent wave sensing: new features for detection in small volumes, Sensors and Actuators A 85, 158-162 (2000).

[10]   R.C. Weast, *Handbook of Chemistry and Physics*, 65th ed. (CRC Press, Boca Raton, Fla., 1984-1985), pp. D-234.

[11]   K. Owaku and M. Goto, Optical Immunosensing for IgG, Sensors and Actuators B 13-14, 723-724 (1993).

[12]   L. Bin, M.R. Smyth, and R. O'Kennedy, Oriented immobilization of antibodies and its applications in immunoassays and immunosensors, The Analyst 121, 29R-32R (1996).

[13]   R.G. Heideman, R.P.H. Kooyman, and J. Greve, Performance of a highly sensitive optical waveguide Mach-Zehnder interferometer immunosensor, Sensors and Actuators B 10, 209-217 (1993).

CHAPTER EIGHT

MULTIPLE WAVELENGTH APPROACH

In this chapter, a new approach that aims at the improvement of the accuracy of the phase change signal measured in an interference-based sensor will be presented. This approach consists of simultaneously using three different wavelengths to separate different contributions that take place in an interferometric sensor, such as refractive index change, thickness variation of an adsorbed layer, and temperature change. In this context, analytical expressions that describe the dependence of the (effective) refractive index change on the temperature change in the sensor system, and on the change of the concentration of a given sample to be monitored, are derived. A good accordance is found between the results achieved by using the new derived relations and the data available from experimental measurements. By overcoming the problem of the temperature influence, often encountered in interferometric sensors, the results obtained by using this approach should be more accurate, potentially leading to a higher resolution and increased stability. [1]

8.1   Introduction

Use of the chemo-optical interference-based sensors in different areas of production and monitoring is becoming important because of their high resolution, good stability, reusability, high level of integration, etc. In an interference-based sensor such as the MZI [1], the YI [2], differential interferometer [3], etc., the phase change signal measured can be caused by a refractive index change and/or a thickness change of a bound layer, both taking place in the sensing window of the measuring arm of the sensor. It often occurs that these two contributions take place simultaneously, e.g in an immunoreaction where a binding event between analyte molecules and a specific receptor layer results in an increase of the refractive index and formation of a new layer. As a result, the measured phase change will be a sum of the individual contributions, i.e. the refractive index change and the layer formation. In addition, the influence of various factors such as temperature changes introduce an extra phase change. In order to reduce such an influence, the reference and measuring branches are usually positioned close to each other to compensate for possible temperature changes. However, this influence cannot be completely avoided, especially at short time intervals after the immunosensing process occurs. In order to account for temperature differences, it is desirable to determine this phase change. Interferometric sensors that separate the refractive index change from the thickness change of a bound layer have been developed, e.g. based on the use of both TE and TM polarization [4].

We propose in this paper, for the first time to our knowledge, a method to calculate simultaneously and separately from each other three different phase change contributions caused by the bulk refractive index change, the thickness change of a bound layer, and the temperature change. This approach consists of simultaneously using three different wavelengths, and because of the dispersion effect, three different phase changes can be measured simultaneously and independently from each other. Consequently, a system of three independent equations can be written based on which three unknowns, i.e. the refractive index change, the thickness change of a bound layer, and the temperature change, can be determined.

In section 8.2, a theoretical description of an interference-based sensor will be presented. Section 8.3 describes the principle of the multiple wavelength approach, including the derivation of two relations that explicitly express the refractive index of a given material as a function of its temperature and concentration. A discussion about this approach will be given in section 8.4, and in section 8.5, a summary of this work will follow.

107

8.2   Theoretical description of an interference-based sensor

In an interference-based sensor, e.g. the MZI [1], or the YI [2], the phase change measured between the reference and measuring arms is in general caused by a change of the effective refractive index of a guided mode, N_{eff}, and/or a change of the length of the sensing window, l, which is realized on top of the measuring and reference arms, as shown schematically in Figure 8.1 for a two-channel YI sensor [2].

In the first order approximation, this phase change can be written as

$$\Delta\Phi = \frac{2\pi}{\lambda}\left(l\Delta N_{eff} + N_{eff}\Delta l\right)$$

(8.1)

where λ is the vacuum wavelength of the light source used.
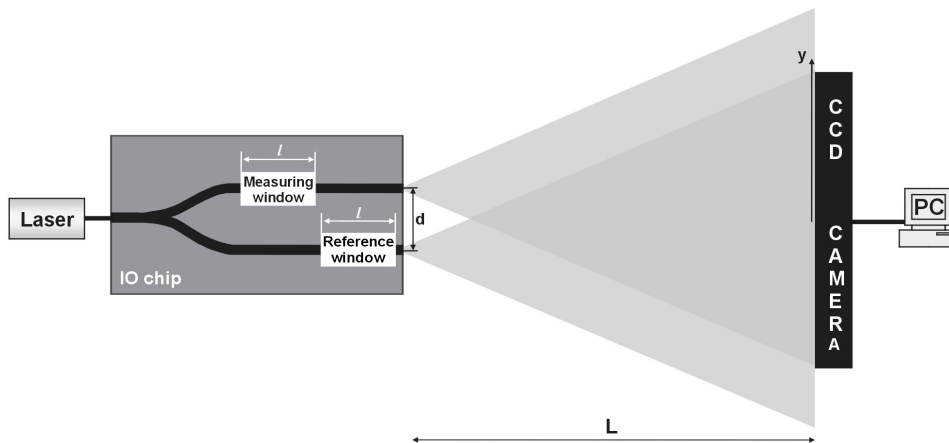
Figure 8.1 *Schematic layout of a two-channel IO YI sensor in which sensing windows are implemented on top of the measuring and reference channels; l, d, and L indicate the length of the sensing windows, distance between two channels, and chip endface - CCD camera distance, respectively.*

Each window has a layer with the same thickness and refractive index, but, while on the measuring window a receptor antibody layer is immobilized, on the reference window a non-active layer (the so-called 'dead layer') is immobilized.

108

This implementation is very helpful in getting rid of all the undesired influences when measuring accurately the contribution of the specific binding event.

The effective refractive index of a guided mode that propagates through a three-layer waveguide structure by probing the core-cover interface where an immunoreaction is taking place (see Figure 8.2) can change due to a change in the concentration of the cover medium, C, change in the thickness of the new layer, d_l, and a change in the temperature, T; whereas, the length of the sensing window can change due to a change in temperature occurring in the sensing system. As a result, for N_{eff} and l the following functional relations can be written

$$N_{eff} = N_{eff}(C, d_l, T)$$
$$l = l(T)$$

(8.2)

Combining Eq. (8.1) and (8.2), the following relations can be derived:

$$\frac{\partial \Phi}{\partial C} = \frac{2\pi}{\lambda} l \frac{\partial N_{eff}}{\partial C}$$

$$\frac{\partial \Phi}{\partial d_l} = \frac{2\pi}{\lambda} l \frac{\partial N_{eff}}{\partial d_l}$$

$$\frac{\partial \Phi}{\partial T} = \frac{2\pi}{\lambda} \left(l \frac{\partial N_{eff}}{\partial T} + N_{eff} \frac{\partial l}{\partial T} \right)$$

(8.3)

where $\partial N_{eff}/\partial C$, $\partial N_{eff}/\partial d_l$, and $\partial N_{eff}/\partial T$ are called the sensitivity coefficient of the effective refractive index with respect to the change of the concentration of the cover medium, thickness of the new layer formed, and temperature, respectively; $\partial l/\partial T$ is the sensitivity coefficient of l with respect to the change of T. $\partial N_{eff}/\partial d_l$ is already derived by Tiefenthaler et al. [5], whereas $\partial N_{eff}/\partial C$, $\partial N_{eff}/\partial T$, and $\partial l/\partial T$ can be derived as the following:

$$\frac{\partial N_{eff}}{\partial C} = \frac{\partial N_{eff}}{\partial n_C} \frac{\partial n_C}{\partial C}$$

$$\frac{\partial N_{eff}}{\partial T} = \frac{\partial N_{eff}}{\partial n_F} \frac{\partial n_F}{\partial T} + \frac{\partial N_{eff}}{\partial n_C} \frac{\partial n_C}{\partial T} + \frac{\partial N_{eff}}{\partial n_S} \frac{\partial n_S}{\partial T} + \frac{\partial N_{eff}}{\partial d_F} \frac{\partial d_F}{\partial T}$$

$$\frac{\partial l}{\partial T} = \alpha \cdot l \cdot \Delta T$$

(8.4)

where $\partial N_{eff}/\partial n_C$, $\partial N_{eff}/\partial n_F$, $\partial N_{eff}/\partial n_S$, $\partial N_{eff}/\partial d_F$ are the sensitivity coefficients of N_{eff} with respect to the change of n_C, n_F, n_S, and d_F, respectively, and α is the 'weighted' thermal linear expansion coefficient of the waveguide structure.

$\partial N_{eff}/\partial n_C$, $\partial N_{eff}/\partial n_F$, and $\partial N_{eff}/\partial d_F$ are already derived by Tienfenthaler et al. [5]; $\partial N_{eff}/\partial n_S$ can be derived in similar way as $\partial N_{eff}/\partial n_C$ due to the spatial symmetry between the cover and the substrate layer. In Eq. (8.4), $\partial n_C/\partial C$ will be called the sensitivity coefficient of the refractive index of the cover with respect to the concentration change, whereas $\partial n_C/\partial T$, $\partial n_F/\partial T$, and $\partial n_S/\partial T$ will be called the sensitivity coefficient of the refractive index of respectively cover, core, and substrate with respect to the change of the temperature. Finally, $\partial d_F/\partial T$ can be derived as $\partial d_F/\partial T = \alpha \cdot d_F \cdot \Delta T$ based on the thermal expansion phenomenon.

Cover layer	n_C
Bound layer	n_p
Core layer N_{eff}	n_F
Substrate layer	n_S
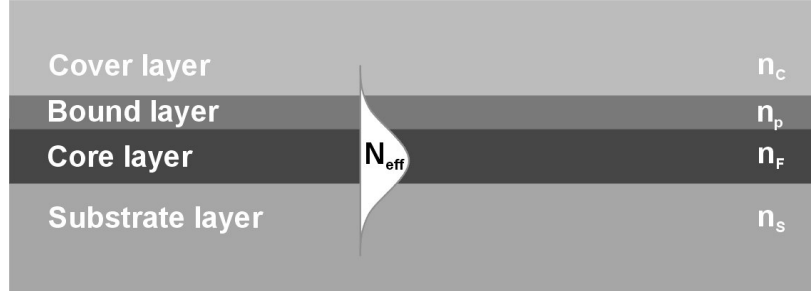
Figure 8.2 *Schematic cross-section of a three-layer waveguide structure in which a bound layer formed at the core - cover interface is probed by a guided mode propagating through this structure; n_p indicates the refractive index of the bound protein layer, n_i, for i = C, F, S, indicates the refractive index of layer i of the waveguide structure.*

Combining Eq. (8.1), (8.3), and (8.4), the final expression of the phase change between the reference and the measuring channel in an interference-based sensor can be written as

$$\Delta\Phi = \frac{2\pi l}{\lambda}\left\{\left[\alpha N_{eff} + \frac{\partial N_{eff}}{\partial T}\right]\Delta T + \frac{\partial N_{eff}}{\partial C}\Delta C + \frac{\partial N_{eff}}{\partial d_l}\Delta d_l\right\} \qquad (8.5)$$

where $\left[\alpha N_{eff} + \dfrac{\partial N_{eff}}{\partial T}\right]$ is called the 'total temperature drift' term. In Eq. (8.5), ΔT, ΔC, and Δd_l are the unknowns to be determined simultaneously and independently in order to separate different contributions from one another. By using three different wavelengths simultaneously, a system of three independent equations can be written, and by solving the system of three equations, three unknowns ΔT, ΔC, and Δd_l can be determined.

110

8.3   Multiple Wavelength Approach (MWA)

If three different wavelengths, e.g. red, yellow and blue colors, will be used simultaneously in an interference-based sensor, then based on Eq. (8.5) a system of three equations can be written as

$$
\begin{cases}
\Delta\Phi^{r} = \dfrac{2\pi l}{\lambda^{r}}\left\{\left[\alpha N_{eff}{}^{r} + \left(\dfrac{\partial N_{eff}}{\partial T}\right)_{r}\right]\Delta T + \left(\dfrac{\partial N_{eff}}{\partial C}\right)_{r}\Delta C + \left(\dfrac{\partial N_{eff}}{\partial d_{l}}\right)_{r}\Delta d_{l}\right\} \\[3mm]
\Delta\Phi^{y} = \dfrac{2\pi l}{\lambda^{y}}\left\{\left[\alpha N_{eff}{}^{y} + \left(\dfrac{\partial N_{eff}}{\partial T}\right)_{y}\right]\Delta T + \left(\dfrac{\partial N_{eff}}{\partial C}\right)_{y}\Delta C + \left(\dfrac{\partial N_{eff}}{\partial d_{l}}\right)_{y}\Delta d_{l}\right\} \\[3mm]
\Delta\Phi^{b} = \dfrac{2\pi l}{\lambda^{b}}\left\{\left[\alpha N_{eff}{}^{b} + \left(\dfrac{\partial N_{eff}}{\partial T}\right)_{b}\right]\Delta T + \left(\dfrac{\partial N_{eff}}{\partial C}\right)_{b}\Delta C + \left(\dfrac{\partial N_{eff}}{\partial d_{l}}\right)_{b}\Delta d_{l}\right\}
\end{cases} \quad (8.6)
$$

where $\Delta\Phi^{r}$, $\Delta\Phi^{y}$ and $\Delta\Phi^{b}$ are the phase changes measured for red, yellow and blue color, respectively. A simpler mathematical presentation of the system of equations (8.6) can be obtained by introducing the following notations:

$$
\begin{aligned}
&\left[\alpha N_{eff}{}^{r} + \left(\frac{\partial N_{eff}}{\partial T}\right)_{r}\right] \equiv D^{r}; \quad \left(\frac{\partial N_{eff}}{\partial C}\right)_{r} \equiv R^{r}; \quad \left(\frac{\partial N_{eff}}{\partial d_{l}}\right)_{r} \equiv Th^{r}; \\[2mm]
&\left[\alpha N_{eff}{}^{y} + \left(\frac{\partial N_{eff}}{\partial T}\right)_{y}\right] \equiv D^{y}; \quad \left(\frac{\partial N_{eff}}{\partial C}\right)_{y} \equiv R^{y}; \quad \left(\frac{\partial N_{eff}}{\partial d_{l}}\right)_{y} \equiv Th^{y}; \\[2mm]
&\left[\alpha N_{eff}{}^{b} + \left(\frac{\partial N_{eff}}{\partial T}\right)_{b}\right] \equiv D^{b}; \quad \left(\frac{\partial N_{eff}}{\partial C}\right)_{b} \equiv R^{b}; \quad \left(\frac{\partial N_{eff}}{\partial d_{l}}\right)_{b} \equiv Th^{b};
\end{aligned} \quad (8.7)
$$

Using the matrix formalism, Eq. (8.7) can be rewritten in the following compact form

$$
\begin{bmatrix}
\Delta\Phi^{r} \\
\Delta\Phi^{y} \\
\Delta\Phi^{b}
\end{bmatrix} =
\begin{bmatrix}
D^{r} & R^{r} & Th^{r} \\
D^{y} & R^{y} & Th^{y} \\
D^{b} & R^{b} & Th^{b}
\end{bmatrix} \cdot
\begin{bmatrix}
\Delta T \\
\Delta C \\
\Delta d_{l}
\end{bmatrix} \quad (8.8)
$$

or:

$$
\overrightarrow{\Delta\Phi} = \overleftrightarrow{SC} \cdot \vec{P} \quad (8.9)
$$

111

where $\overrightarrow{\Delta\Phi}$, $\overrightarrow{SC}$, and $\vec{P}$ are called as the 'phase changes vector', the 'sensitivity coefficients matrix' and the 'unknown parameters vector', respectively.

By solving Eq. (8.9), one can determine the unknown parameters matrix as

$$\vec{P} = \overrightarrow{SC^{-1}} \cdot \overrightarrow{\Delta\Phi} \tag{8.10}$$

where $\overrightarrow{SC^{-1}}$ is the inverse matrix of $\overrightarrow{SC}$.

In order to solve Eq. (8.8), the sensitivity coefficients matrix $\overrightarrow{SC}$ should be known and for that purpose, the explicit expressions of the sensitivity coefficients of the refractive index with respect to the change of the temperature and concentration should be derived or experimentally determined.

8.3.1 Temperature-based sensitivity coefficient

In this section, an analytical expression, which describes the dependence of the (effective) refractive index change from the change of the temperature in a three-layer waveguide structure, will be derived.

We start from the general dispersion equation that relates the refractive index n of a given material with the properties of such a material [6], i.e.

$$\frac{n^2 - 1}{n^2 + 2} = \frac{Nq_e}{3\varepsilon_0 m_e} \sum_j \frac{f_j}{\omega_{oj}{}^2 - \omega^2 + i\dot{\gamma}_j\omega} = kN \tag{8.11}$$

where N represents the number of the molecules of such a material per unit volume and k denotes

$$k \equiv \frac{q_e}{3\varepsilon_0 m_e} \sum_j \frac{f_j}{\omega_{oj}{}^2 - \omega^2 + i\dot{\gamma}_j\omega} \tag{8.12}$$

All other parameters that appear in Eq. (8.11) are constants depending on the properties of the material.

Let us assume that the material has a refractive index n_0 and volume V_0 at a given temperature T_0, and N_0 is the number of molecules per unit volume at this temperature. The total number of the molecules contained in the volume V_0, N', can be written as

$$N' = N_0 L_0{}^3 \tag{8.13}$$

assuming a cubic volume of the material with a side length of L_0 at the temperature T_0.

Considering the situation at a temperature $T \neq T_0$, due to the thermal expansion phenomenon, the volume will change from V_0 to V and the number of molecules per unit volume becomes

$$N = \frac{N'}{V} = \frac{N'}{L_0{}^3 \left[1 + \alpha(T - T_0)\right]^3} \cong N_0 (1 - 3\alpha\Delta T) \qquad (8.14)$$

where α is the linear expansion coefficient of the material and $\Delta T = T - T_0$. Eq. (8.14) is derived based on the Newton's Binomial Theorem by considering that α^2, $\alpha^3 << \alpha$ for $\alpha << 1$.

Using Eq. (8.11) and (8.14), the refractive index of the given material at temperature T can be written as

$$\frac{n^2 - 1}{n^2 + 2} = kN_0 (1 - 3\alpha\Delta T) \qquad (8.15)$$

After performing some further mathematical calculations, Eq. (8.15) can be transformed to

$$n = n_0 - \frac{9}{2} \frac{\alpha k N_0}{(1 - kN_0) \cdot \left(1 + kN_0 - 2k^2 N_0{}^2\right)^{1/2}} \Delta T \qquad (8.16)$$

On the other hand, in similarity with Eq. (8.11), the dispersion relation at the temperature T_0 can be written as $kN_0 = (n_0{}^2 - 1)/(n_0{}^2 + 2)$. Finally, the relation expressing the refractive index n as a function of the temperature T can be derived as

$$n = n_0 \cdot \left\{ 1 - \frac{1}{2} \cdot \left[\frac{\left(n_0{}^2 - 1\right) \cdot \left(n_0{}^2 + 2\right)}{n_0{}^2} \right] \cdot \alpha \cdot \Delta T \right\} \qquad (8.17)$$

From Eq. (8.17), the relation that describes the explicit dependency of the sensitivity coefficient of the refractive index from the temperature change can be derived, i.e.

$$\frac{\partial n}{\partial T} = \left(-\frac{1}{2} \right) \cdot \left[\frac{\left(n^2 - 1\right) \cdot \left(n^2 + 2\right)}{n} \right] \cdot \alpha \qquad (8.18)$$

113

Derivation of Eq. (8.18) gives the possibility to calculate the temperature-based sensitivity coefficient $\partial N_{eff}/\partial T$ because:

1. Coefficients $\partial n_i/\partial T$, ($i = C$, F, C) can be easily derived from Eq. (8.18) as

$$\frac{\partial n_i}{\partial T} = \left(-\frac{1}{2}\right) \cdot \left[\frac{\left(n_i^2 - 1\right) \cdot \left(n_i^2 + 2\right)}{n_i}\right] \cdot \alpha_i \tag{8.19}$$

where α_i is the linear expansion coefficient for layer i.

2. The sensitivity coefficients $\partial N_{eff}/\partial n_F$, $\partial N_{eff}/\partial n_C$ and $\partial N_{eff}/\partial d_F$ have been already derived by Tiefenthaler et al. [5]; $\partial N_{eff}/\partial n_s$ can be derived in the same way as $\partial N_{eff}/\partial n_C$, because of the spatial symmetry between the cover and the substrate layer in a three-layer waveguide structure (see Figure 8.2). In case of the TE polarization, these coefficients have the following explicit form

$$\frac{\partial N_{eff}}{\partial n_F} = \left(\frac{n_F}{N_{eff}}\right)\left(\frac{1}{d_F + Y_{OC} + Y_{OS}}\right)\left(d_F + \sum_{J=C,S}\left(\frac{N_{eff}^2 - n_j^2}{n_F^2 - n_j^2}\right)Y_{O,J}\right)$$

$$\frac{\partial N_{eff}}{\partial n_C} = \left(\frac{n_C}{N_{eff}}\right)\left(\frac{n_F^2 - N_{eff}^2}{n_F^2 - n_C^2}\right)\left(\frac{Y_{OC}}{d_F + Y_{OC} + Y_{OS}}\right)$$

$$\frac{\partial N_{eff}}{\partial n_S} = \left(\frac{n_S}{N_{eff}}\right)\left(\frac{n_F^2 - N_{eff}^2}{n_F^2 - n_S^2}\right)\left(\frac{Y_{OS}}{d_F + Y_{OC} + Y_{OS}}\right)$$

$$\frac{\partial N_{eff}}{\partial d_F} = \left(\frac{n_F^2 - N_{eff}^2}{N_{eff}}\right) \cdot \left(\frac{1}{d_F + Y_{OC} + Y_{OS}}\right) \tag{8.20}$$

where Y_{OC} and Y_{OS} are the penetration depths on the cover and substrate layer respectively.

8.3.2   Concentration-based sensitivity coefficient

In this section, the explicit expression of $\partial N_{eff}/\partial C$ will be derived in terms of the waveguide parameters and mass concentration of the cover medium. For that purpose, first the sensitivity coefficient of the refractive index of a given material with respect to the mass concentration will be analytically derived.

Let us define the mass concentration of a given medium as the mass of all the molecules of this medium per unit volume. If N is the number of molecules per unit volume and m_0 is the mass of one molecule, then the concentration will be

$$C = Nm_0 \tag{8.21}$$

114

The general dispersion relation, given in Eq. (8.11), can be written in terms of mass concentration C as

$$\frac{n^2 - 1}{n^2 + 2} = k' C \qquad (8.22)$$

where $k' = k/m_0$. Eq. (8.22) can be written as a function of the refractive index, n, and the concentration, C, in the following functional form:

$$\frac{n^2 - 1}{n^2 + 2} - k'C = 0 \equiv f[C, n(C)] \qquad (8.23)$$

By differentiating implicitly Eq. (8.23), the partial derivative of the refractive index with respect to the concentration will be given as

$$\frac{\partial n}{\partial C} = -\frac{\partial f/\partial C}{\partial f/\partial n} = \frac{\left(n^2 - 1\right) \cdot \left(n^2 + 2\right)}{6Cn} \qquad (8.24)$$

A finite change of the refractive index, Δn, can be calculated by integrating the last equation, i.e.

$$\Delta n \equiv n_1 - n_0 = \frac{\left({n_0}^2 - 1\right) \cdot \left({n_0}^2 + 2\right)}{6n_0} ln\left(\frac{C_1}{C_0}\right) \qquad (8.25)$$

where n_0 and n_1 are the refractive indices corresponding to concentrations C_0 and C_1, respectively.

Based on Eq. (8.4) and Eq. (8.24), the concentration-based sensitivity coefficient $\partial N_{eff}/\partial C$ can be written as

$$\frac{\partial N_{eff}}{\partial C} = \frac{\partial N_{eff}}{\partial n_C} \frac{\left({n_C}^2 - 1\right) \cdot \left({n_C}^2 + 2\right)}{6Cn_C} \qquad (8.26)$$

115

8.4 Discussion

The refractive index of a given medium can be calculated as a function of its temperature and concentration using Eq. (8.17) and (8.25). The results achieved according to these two equations are compared with the ones obtained using experimental data from the Handbook of Chemistry and Physics [7].

Figure 8.3 shows the refractive index of pure water for different temperatures calculated by using Eq. (8.17). In the same Figure, that dependency based on the experimental data taken from the Handbook of Chemistry and Physics is plotted. According to Figure 8.3, the results obtained from calculations are in good agreement with experimentally achieved results.
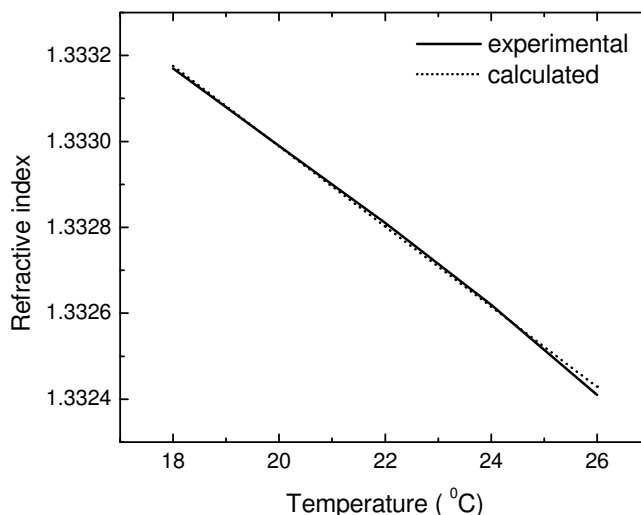
Figure 8.3 *Refractive index of pure water vs. the temperature: solid line is constructed based on the experimental data taken from the Handbook of Chemistry and Physics, dotted line represents the data obtained from calculations using Eq. (8.17).*

Next, the refractive index of glucose solution with different concentrations, calculated from Eq. (8.25), is compared with the experimentally achieved results (data taken from the Handbook of Chemistry and Physics). The curve obtained from calculations (slope ~ 1.42×10^{-5} ml/g) agrees well with the one constructed based on experimental data (slope ~1.47×10^{-5} ml/g), as shown in Figure 8.4.

In both cases, a calibration may be applied to correct for the difference between expected and measured curves.

116

Derivation of relations (8.17) and (8.25) allows for calculation of $\partial N_{eff}/\partial T$ and $\partial N_{eff}/\partial C$, making possible determination of the sensitivity coefficients matrix, $\overrightarrow{SC}$. To this end, using Eq. (8.10), three different unknowns, i.e. ΔT, ΔC, and Δd_l can be calculated separately and individually from each other.
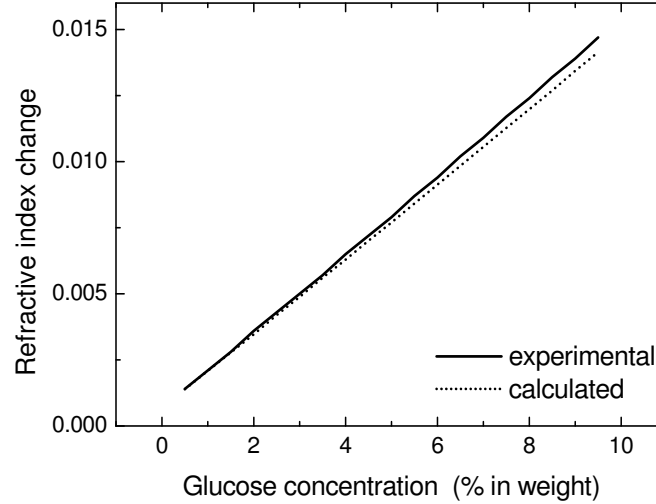
Figure 8.4 *Refractive index change of a glucose solution versus its concentration: solid line represents experimental data taken from the Handbook of Chemistry and Physics; dotted line shows the data achieved by using Eq. (8.25).*

The determinant of $\overrightarrow{SC}$, which for a given wavelength depends on the parameters of the waveguide structure, should be different from zero to allow calculation of the inverse matrix, $\overrightarrow{SC^{-1}}$, necessary to solve Eq. (8.10). In addition, to achieve a high sensitivity towards ΔT, ΔC, and Δd_l, the determinant of $\overrightarrow{SC}$ should be maximal, such that a given phase change measured for each wavelength can correspond to smaller values for these parameters.

In order to estimate the resolution that can be achieved for ΔT, ΔC, and Δd_l, e.g. in case of our sensor, the influence of some other effects, such as laser fluctuations, vibrations, etc., should also be taken into consideration. If the time scale on which these factors take place is different from those of the signal and temperature drift, then a filtering could be applied in the frequency domain in order to reduce these effects and improve accuracy of the drift correction

algorithm. For that purpose, experimental tests should be performed in order to determine the frequency distribution of these disturbing effects.

8.5 Summary

In this chapter, a theoretical approach for discrimination of three different contributions in the phase change measured in an interference-based sensor, being the refractive index change, thickness of a bound layer, and the temperature change, is derived. The new approach consists of simultaneous use of three different wavelengths, resulting in a system of three equations (one for each wavelength), from which three different contributions can be separately and independently calculated.

In order to solve the system of three equations, sensitivity coefficients that relate change of the effective refractive index of guided modes with the concentration change of the cover medium, thickness change of the bound layer, and the temperature change, should be known. For that purpose, we have theoretically derived two new analytical expressions: the first expresses the refractive index change of a given medium versus the temperature change, and the second one can be used to derive the refractive index change as a function of the concentration change. These two expressions are derived based on the general dispersion relation. The results achieved using new derived relations are in good agreement with experimental data taken from the Handbook of Chemistry and Physics.

Implementation of the multiple wavelength approach can result in an increase of the accuracy of the phase change measured in an interferometric sensor by subtracting the contribution of the temperature change, improving in that way the long-term stability of these sensors potentially leading to higher resolution.

References

[1]   R.G. Heideman and P.V. Lambeck, Remote opto-chemical sensing with extreme sensitivity: design, fabrication and performance of a pigtailed integrated optical phase-modulated Mach-Zehnder interferometer system, Sensors and Actuators B 61, 100-127 (1999).

[2]   A. Ymeti, J.S. Kanger, R. Wijn, P.V. Lambeck, and J. Greve, Development of a multichannel integrated interferometer immunosensor, Sensors and Actuators B 83, 1-7 (2002).

[3]   C. Stamm and W. Lukosz, Integrated optical difference interferometer as immunosensor, Sensors and Actuators B 31, 266-271 (1996).

[4]   G.H. Cross, A.A. Reeves, S. Brand, J.F. Popplewell, L.L. Peel, M.J. Swann, and N.J. Freeman, A new quantitative optical sensor for protein characterization, Biosensors and Bioelectronics 19, 383-390 (2003).

[5]   K. Tiefenthaler and W. Lukosz, Sensitivity of grating couplers as integrated-optical chemical sensors, J. Opt. Soc. Am. B 6, 209-220, (1989).

[6]   E. Hecht, *Optics* (Addison Wesley, Reading, Mass., 1998).

[7]   R.C. Weast, *Handbook of Chemistry and Physics*, 65th ed. (CRC Press, Boca Raton, Fla., 1984-1985), pp. D-234.

CHAPTER NINE

DISCUSSION AND CONCLUSIONS

In this chapter, the performance and applications of the multichannel IO YI sensor as described in this thesis will be discussed. First, a summary of the achieved results will be given. Next, a comparison between the multichannel YI sensor and other interferometric sensors, as well as other techniques, will be presented. New aspects of the multichannel YI sensor will be discussed, including applications for virus detection, integration with microfluidics, drift-correction, etc. To this end, an outlook concerning further improvement of the performance of this type of sensors will be presented.

9.1 Summary of the results achieved in this thesis

In this thesis, we presented the development of highly sensitive multichannel IO YI sensing systems. The working principle of a two-channel IO YI is expanded to a multichannel device by introducing a manifold of output parallel channels at well-defined distances from each other such that the distance between channels of each pair, functioning as a two-channel YI, is unique. The first design of the multichannel YI has four output parallel channels where the phase change for each pair of channels can be monitored simultaneously and independently from the other channel pairs.

We have presented a thorough theoretical analysis, optimization of the design, realization, and experimental characterization of the four-channel IO YI sensing system. The realization of such a system was done using SiON technology, which is well developed at the MESA$^+$ Institute for Nanotechnology.

Table 9.1 *A summary of the main properties for the two-channel and the four-channel YI sensing systems.*

		Multichannel IO YI sensing system	
		2 channels	4 channels
Resolution*	$\Delta\varphi$ [2π]	1.5×10^{-5}	7×10^{-5}
	Δn	3×10^{-9}	6×10^{-8}
	$\Delta m/A$ [fg/mm^2]	1	20
Drift [$2\pi \cdot h^{-1}$]		5×10^{-4}	5×10^{-4}
Interaction length [mm]		20	4
Phase error [%]		< 1.5	< 3
Cross talk [%]		-	< 3
Response time	Bulky cuvette [s]	100	100
	Microfluidics [s]	5	5

* The resolution is defined as the standard deviation of the signal at a bandwidth of 1 Hz (corresponding to a $S/N = 1$).

Some of the main properties of the multichannel IO YI sensing systems described in this thesis are summarized in Table 9.1. Note that the response time is defined with respect to a fluid change.

The resolution we find is limited by one or more disturbing factors mentioned in section 3.5, e.g. noise in the CCD camera, the slab light, temperature changes, etc. Futures experiments should focus on identifying and evaluating these noise sources.

We have experimentally shown that the four-channel YI sensor can be used to simultaneously and nearly independently (cross-talk < 3%) measure different analytes or different concentrations of one analyte. In principle, a multichannel YI that has N channels can measure $N - 1$ different analytes or different concentrations of one analyte.

The multichannel YI sensor has been successfully used for detection of Human Herpes Simplex virus, as a preliminary step for detection of more relevant viruses such as HIV, SARS, Hepatitis B and C, etc. Estimations show that the resolution of the four-channel YI sensor can afford detection of a single virus particle. Moreover, monitoring of proteins associated with virus particles, such as Hepatitis-B and HIV, was performed. In that way, we have demonstrated that the YI sensor can be efficiently used for medical screening.

It is demonstrated that in a multichannel IO YI it is possible to correct appreciably for the phase changes due to drift. These are mainly due to time dependent variation of temperature differences between measuring and reference channels. The drift in the phase was decreased by a factor of ~ 10 when the new drift-correction method was applied. Implementation of this correction technique is possible because of the unique properties of the multichannel integrated YI sensing system, designed such that the phase change for each possible channel pair can be simultaneously measured.

Furthermore, a microfluidic system was designed, fabricated, and bonded to a four-channel IO YI optical chip. It is experimentally shown that the implementation of the microfluidics reduces the response time of the sensor by a factor of ~ 20 (to ~ 5 s) as compared to a bulky cuvette. In addition, the volume of the sample solution required to perform an immuno-test was much smaller (factor of ~ 1000) than that used in the original bulky cuvette-based system. The monitoring of the anti-human serum albumine – human serum albumine immunoreraction demonstrates that by using such a microfluidic system, a better discrimination between the bulk effects caused by the refractive index difference of solutions and the layer formation can be made, resulting into a higher accuracy and offering the prospect of being able to utilize the kinetics of the immunoreaction.

124

In addition, a novel approach, consisting of simultaneous use of three different wavelengths for discrimination of three different contributions in the phase change measured in an interference-based sensor, i.e. the refractive index change, thickness of a bound layer, and temperature change, is derived. Two new analytical relations that express the refractive index change of a given medium as a function of the temperature change and concentration change were derived. The results obtained from new derived relations are in good accordance with experimental data taken from the Handbook of Chemistry and Physics. Implementation of the multiple wavelength approach can potentially lead to a higher resolution for the interference-based sensors.

9.2 Discussion

Here, the performance of the multichannel IO YI sensing system will be compared with that of other IO interferometric sensors, as well as other available optical sensors. This evaluation will be focused on parameters such as resolution, stability, accuracy, throughput, response time, as well as variety of applications that can be performed.

Table 9.2 shows a comparison between the multichannel YI sensing systems presented in this thesis and other IO YI sensors and phase-modulated MZI, including the commercially available YI-based sensor from Farfield Sensors. The comparison is also made with the commercially available SPR-based sensors from BIACORE and IBIS Technologies bv.

The multichannel IO YI sensing system we have developed shows a comparable refractive index resolution with that of other IO YI sensor systems that have been realized so far [1-4], including the commercially available YI-based sensor from Farfield Sensors [5]. It shows a higher mass coverage resolution (factor of ~ 10), due to optimized waveguide structure and better technology we use; it also shows a better stability, which can be further improved up to one order of magnitude using the drift-correction method. Moreover, our sensor can simultaneously monitor up to 3 different analytes versus the one that other YI devices can do.

Compared to other interferometric sensors, our sensor shows a refractive index and mass coverage resolution that are comparable with those of the IO phase-modulated MZI [6], including the stability, and higher resolution and better stability than the differential interferometer [7-8] and the Fabry-Perot interferometer [9] (not shown in Table 9.2).

Note that the two-channel YI sensor shows a refractive index and mass coverage resolution that are at least one order of magnitude better than the four-channel YI and other interferometric sensors. This is the highest resolution ever achieved with an interferometric sensor [1-9].

Our sensor is one of the first interferometric sensing systems where microfluidics is applied, resulting in a very short response time related to changes of liquids (a few seconds) and low sample volume (several microliters), which in combination with the on-line monitoring, can lead to a fast screening for different medical applications.

Table 9.2 *Comparison of the IO YI sensing systems with other interferometric and optical devices.*

		Resolution			Drift $[2\pi \cdot h^{-1}]$	Interaction length [mm]	Relative error [%]	No. of channels	Response time [s]
		$\Delta\varphi$ $[2\pi]$	Δn	$\Delta m/A$ $[fg/mm^2]$					
YI (this thesis)	2-ch	1.5×10^{-5}	3.0×10^{-9}	1	5×10^{-4}	20	< 1.5	2	5
	4-ch	7.0×10^{-5}	6.0×10^{-8}	20	5×10^{-4}	4	< 3.0	4	5
YI (Brandenburg [2-3])		5.6×10^{-4}	7.0×10^{-7}	250	7×10^{-3} (?)	12	?	2	200
YI (Cross et al. [4] Farfield sensors [5])		8.7×10^{-5}	3.6×10^{-7}	300	?	?	0.1(?)	2	85
Phase-modulated MZI [6]		1.0×10^{-4}	5.0×10^{-8}	30	3×10^{-4}	4	?	2	?
BIACORE [13]		-	1.0×10^{-6} (?)	1000	-	-	?	4	?
IBIS II [14]		-	7.5×10^{-6}	7500	-	-	< 1.5	2	-

Presence of viruses is mainly detected by a time-consuming procedure that includes culturing and amplification [10]. Recently, detection of herpes simplex

virus has been performed by using rupture event scanning technique, which is based on measuring adhesion forces between a surface and small particles [11]. The multichannel IO YI sensor was also successfully used as a first interferometric sensor for detection of virus particles in several minutes, being relevant for fast screening purposes. In addition, monitoring of proteins that are associated with virus particles demonstrates an additional prospective of the sensor in the field of medical screening.

Compared to other optical sensors, such as SPR-based sensors, the multichannel YI shows a resolution that is roughly higher by two orders of magnitude [12], including the commercially available sensors from BIACORE [13] and IBIS Technologies bv [14]. On the other hand, it should be mentioned that the SPR-based sensors show an advantage related to the prospect of the number of analytes that can be monitored [12], while the present SPR sensor from BIACORE can also monitor up to three different analytes simultaneously. Nevertheless, by using new multichannel approaches (see chapter 10), the interference-based sensors can further improve their throughput.

In a broader perspective, the multichannel IO YI sensor can also be compared with the ELISA, which is a commercially available standard label-based technique. In a previous project in Biophysical Techniques Group [15], it was shown that the resolution of the planar waveguide MZI was sufficient to detect atrazine concentrations as little as 100 ng/L [16], a value comparable with that of the ELISA [17]. Our sensor shows a resolution that is at least one order of magnitude better than that of the planar waveguide MZI, indicating that it may be able to detect at least this concentration. Furthermore, the multichannel operation developed during this project, leading to a high throughput, makes the IO YI sensor more competitive with these types of techniques.

Here, besides the advantage that no labeling and skilled personnel is necessary, the multichannel IO YI sensor offers several advanced aspects, such as real-time monitoring of macromolecular interactions, which can hardly be performed with label-based techniques. Some potential applications that result from this feature include affinity measurements and binding kinetics, concentration determinations, etc.

Moreover, by sensing optically, electromagnetic interference and the danger of explosion can be avoided, e.g. when interferometric sensors are used to monitor different industrial processes. All basic functions of a sensing structure can be realized simultaneously, and even several of these structures can be realized in a single wafer. This indicates the economical aspect of the integrated optical sensor devices in general and interferometric ones in particular, including the multichannel IO YI sensing system.

9.3 Outlook

Here, some aspects aiming at the improvement of the performance of the multichannel IO YI sensing system and possible applications will be discussed.

To give an impression of the possibilities that offer the YI sensing system, we will show a calculation about the possible resolution of this system. We consider a 2 mw light source, which emits roughly 2 x 10^{16} photons/s and calculate the shot noise limited resolution. For simplicity, we assume that only one fringe of the interference pattern is generated. In that case, there will be 2 x 10^{16} photons per interference fringe or ~ 10^{16} photons per half interference fringe. If these photons can be detected with a shot-noise limited detector, the signal-to-noise ratio can be as high as 10^8. This means that a shift of 10^{-8} fringes (corresponding to a signal change of 10^8 photons) can be detected with a *S/N* ratio ~ 1. Compared to the current resolution of the YI sensing system (~ 10^{-5} fringes), this is an improvement by three orders of magnitude. This means on the other hand that by choosing a shorter interaction length (micrometers) at the present resolution the chip area can be very small, which further favors development of multisensing array systems.

This estimation indicates that by getting rid of the different disturbing factors that limit the current resolution of the sensing system, considerable improvement may be reached. For that purpose, disturbing factors such as temperature effects, vibrations of the set-up, contaminations, fluctuations in the density of the sample liquids, as well as the noise from the CCD camera and light source, technological imperfections, etc., should be reduced as much as possible. Temperature effects can be suppressed by application of the drift-correction method (see chapter 6), and/or implementation of the multiple wavelength approach, as described in chapter 8; other ways such as controlling the temperature of the sensing system may give improvements as well. Performing the experiments in vacuum conditions and/or low temperatures, if this will be possible, may also suppress the temperature fluctuations, although the reaction rates for watery solutions become very low. For technological imperfections such as non-uniformity of the thickness and width of the channel waveguide, different length of the channels, as well as that of the sensing windows, deviations are constant, suggesting application of calibration to reduce their influence. Furthermore, a light source with high power and low noise level and a CCD camera that has low noise level are preferred.

Concerning the throughput of the YI sensing system, the number of channels in the YI can be further increased up to ~ 17 for the same set-up parameters (see chapter 3), apart from the chip design. However in that case, the resolution and the accuracy of the sensor is expected to be deteriorated, because a larger number of channels means an increase on the number of spatial frequencies, making the signal analysis more inaccurate. Using other configurations of the

multichannel YI, the number of analytes that can be simultaneously monitored may be even larger, especially in a 2D-array configuration, see the discussion in chapter 10.

To this end, it is also interesting to give an overview of different applications that can be performed with the multichannel IO YI sensor.

As presented in this thesis, this sensor is extremely sensitive and very fast. These two aspects are important for some applications, e.g. extreme sensitivity can be used to directly measure small molecules, such as pesticides (~ 200 Da) in milk or drinking water.

Being fast indicates the use of this sensor for medical screening, e.g. we have experimentally shown detection of herpes simplex virus, but in a similar way, detection of HIV, SARS, and Hepatitis virus, as well as bacteria and BSE may be done. An important element here will be the chemo-optical transduction layer, being strongly related to the chemistry of the sensing surface, which needs more attention and further investigations, depending on the specific application.

The results achieved in this thesis indicate the possibilities the multichannel IO YI sensing system can offer, as a new lab-on-a-chip configuration. Further improvements of the system can lead to a better performance, making this type of sensors more interesting and useful for a broader spectrum of applications in areas such as health care, food analysis, environment monitoring, bioprocess control, etc.

129

References

[1]   I.S. Duport, P. Benech, and R. Rimet, New integrated-optics interferometer in planar technology, Applied Optics 33, 5954–5958 (1994).

[2]   A. Brandenburg, Differential refractometry by an integrated-optical Young interferometer, Sensors and Actuators B 38-39, 266-271 (1997).

[3]   A. Bradenburg, R. Krauter, C. Kuenzel, M. Stefan, and H. Schulte, Interferometric sensor for detection of surface-bound bioreactions, Applied Optics 39, 6396-6405 (2000).

[4]   G.H. Cross, A.A. Reeves, S. Brand, J.F. Popplewell, L.L. Peel, M.J. Swann, and N.J. Freeman, A new quantitative optical sensor for protein characterization, Biosensors and Bioelectronics 19, 383-390 (2003).

[5]   Farfield Sensors Ltd, Salford, UK (www.farfield-sensors.co.uk).

[6]   R.G. Heideman and P.V. Lambeck, Remote opto-chemical sensing with extreme sensitivity: design, fabrication and performance of a pigtailed integrated optical phase-modulated Mach-Zehnder interferometer system, Sensors and Actuators B 61, 100-127 (1999).

[7]   C. Stamm and W. Lukosz, Integrated optical difference interferometer as immunosensor, Sensors and Actuators B 31, 266-271 (1996).

[8]   T. Koster and P.V. Lambeck, Fully integrated polarimeter, Sensors and Actuators B 82, 213-226 (2002).

[9]   E.R. Cox and B.E. Jones, Fiber optic color sensors based on Fabry-Perot interferometry, Proceedings of First international conference on optical fiber sensors, London, 1993.

[10]   A.C. Minson, Alphaherpesviruses: herpes simplex and varicella zoster virus infections. In *Topley and Wilson's microbiology and microbial infenctions,* Vol. 1, Edn. 9 (eds Mahy, B. & Collier, L.) 325-339 (Arnold, London; 1998).

[11]   M.A. Cooper, F.N. Dultsev, T. Minson, V.O. Ostanin, C. Abell, and D. Klenerman, Direct and sensitive detection of a human virus by rupture scanning event, Nature Biotechnology 19, 833-837 (2001).

[12]   C.E.H. Berger, T.A.M. Beumer, R.P.H. Kooyman, and J. Greve, Surface plasmon resonance multisensing, Anal. Chem. 70, 703-706 (1998).

[13]   BIACORE, Pharmacia Biosensor AB, Uppsala, Sweden (www.biacore.com).

[14]   IBIS II, IBIS Technologies bv, Hengelo, The Netherlands (www.ibis-spr.nl).

[15]   E.F. Schipper, Waveguide immunosensing of small molecules, Ph.D. Thesis, University of Twente, The Netherlands, 1997.

[16]   E.F. Schipper, A.J.H. Bergevoet, R.P.H. Kooyman, and J. Greve, New detection method for Atrazine pesticides with the optical waveguide Mach-Zehnder immunosensor, Analytica Chimica Acta 341, 171-176 (1997).

[17]   M. Wortberg, M. Goodrow, S.J. Gee, and B.D. Hammock, Immunoassay for simazine and atrazine with lower cross-reactivity for propazine, J. Agric. Food Chem. 44, 2210-19, (1996).

CHAPTER TEN

FURTHER DEVELOPMENT
OF THE MULTICHANNEL INTEGRATED
INTERFERENCE-BASED SENSORS

In this chapter, some new ideas for development of multichannel interferometric sensing systems will be presented. These ideas are mainly meant for new multichannel approaches, e.g. by using multimode interference couplers. Moreover, a new approach for a multichannel sensor that includes the use of a phase modulation and Fourier transformations will be described. In addition, an array-based interferometer approach will be shown.

10.1 Introduction

In this thesis, development of highly sensitive four-channel IO YI sensing systems, which can simultaneously monitor up to three different processes with a phase resolution of $\sim 7 \times 10^{-5} \times 2\pi$, is presented. The phase resolution obtained is among the highest phase resolutions ever achieved with an interferometric sensor; see chapter 9 and references [1-3]. To achieve a high sensitivity, parameters of the waveguide structure of these sensing systems have been optimized and the SiON technology [4-6], as one of the well-known technologies in integrated optics, is used for their realization. The multichannel function was implemented by using a network of optical Y-junctions channel waveguides.

It is interesting to discuss how for instance the resolution and stability of these sensors can be further improved. Ways to achieve these improvements are e.g. development of new technologies, or implementation of new operation principles, etc. The same discussion can be given for the number of processes that can be monitored with these types of sensors and what configurations might then be.

In the next sections, some new ideas for further development of multichannel interferometric sensing systems will be presented.

10.2 Time-modulated multichannel MZI

The layout of a new multichannel MZI is schematically shown in Figure 10.1. It consists of coupling the light into an input channel, splitting it to a certain number of parallel channels, which are combined again to one output channel. As a result of overlapping of more than two signals, the interference pattern will be a superposition of all individual interference patterns, one for each pair of channels. The sum interference pattern in that case can be recorded by a photo diode (PD).

A phase modulation can be used to introduce extra phase changes in the channels with different modulation frequencies. In that way, individual interference patterns with different frequencies will be obtained in the time domain. If one realizes a Fourier transform of the sum interference pattern at a given frequency, which is smaller than all modulation frequencies, the phase change for each pair of channels can be extracted. The modulation frequency for each channel should be different to allow selection of different peaks from the Fourier transform, similar to the algorithm used for the YI. As a result, the phase information for each pair of channels can be simultaneously obtained.

133
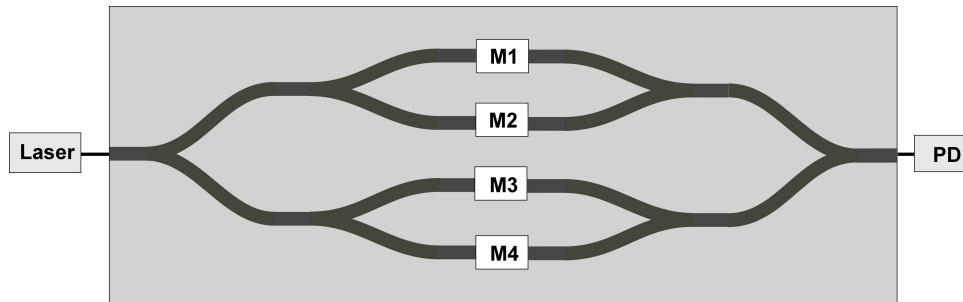
Figure 10.1 *Schematic layout of a multichannel MZI device: Mi is the phase modulation applied in channel i.*

Compared to the YI based sensor, where individual interference patterns are generated in the space domain and recorded with a CCD camera, here a PD can be used to record the interference patterns generated in the time domain. In the new configuration, the influence of the air medium between channel outputs and recording equipment is avoided, resulting in more stable measurements. In addition, a PD is used instead of the CCD camera, resulting in a cheaper sensing system. On the other hand, for the new configuration phase modulators have to be applied on each channel, including extra work for fabrication of the optical chip, and proper electronics for modulation function is required.

10.3   Array-based multichannel interferometer

A new multichannel interferometer system may be realized by arranging several channel waveguides in an array configuration as shown in Figure 10.2. A set of N parallel channels can be combined with another set of N parallel channels oriented perpendicular to the first set. The crossing areas between these two sets of parallel channels can be considered as sensing areas where different receptor layers can be immobilized. For each set of parallel channels, one of the channels can be used as a reference, e.g. channel N as shown in Figure 10.2. The readout principle can be a Young or a Mach-Zehnder interferometer based sensor.

Monitoring of binding events may be performed in two successive runs: in the first run binding events taking place in areas presented in black are monitored, and in the second run the events in the areas left are measured. For example if $N = 5$, there will be 8 events taking place in the first run and 8 other events in the second run. For each run, the number of independent equations that can be written will be equal with the number of events. In that way, the total number of events that can be monitored will be 16.
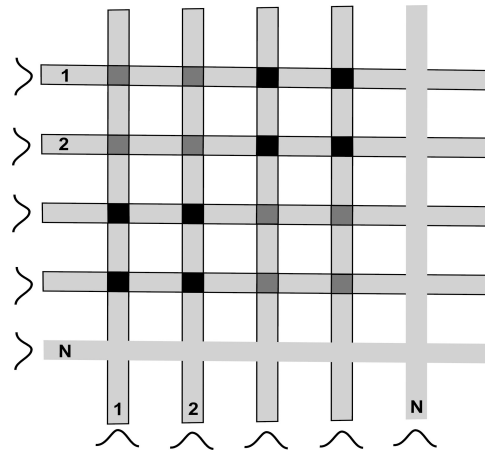
Figure 10.2 *Schematic presentation of an array-based multichannel interferometer system.*

An advantage of this configuration can be the monitoring of a large number of processes, although there are disadvantages as well, e.g. the light should be split to a large number of channels and the interaction length of sensing areas will be smaller as compared to current devices, resulting in a decrease of the sensitivity.

10.4 Multimode Interference (MMI)-based sensors

10.4.1 MMI couplers

Here, a short description about an MMI coupler will be given. A multimode interference coupler [7-8] consists of a number of single mode input and output channel waveguides and a central channel waveguide structure, which is single mode in vertical direction and multimode in lateral direction, see Figure 10.3. These modes overlap with each other and an interference pattern can be generated, e.g. at the endface of the MMI. Depending on the width and length of MMI central structure, the input light can be equally split to a number of output channels, or light from two or more input channels can be combined to a given output channel. The splitting/combining function can be performed in a relatively short distance (several hundreds of micrometers).

In the next sections, an MMI will be involved for designing of multichannel interferometric sensors. Note that ease of handling is one of the main aspects of an MMI-based sensor.

135
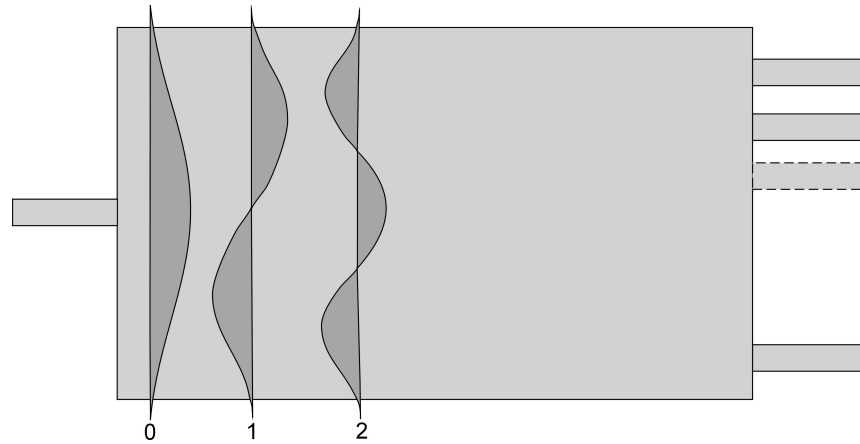
Figure 10.3 *Schematic top-view of a 1 x N MMI coupler; i indicates the order of excited modes.*

10.4.2   Multichannel YI

An MMI can be incorporated as the basic optical component in a multichannel YI sensor. In that case, a 1 x *N* MMI splitter can be used to equally split the input light to *N* output parallel channels, their number depending on the width and length of the MMI splitter, and a second MMI can be used to combine the light from the *N* channels in order to generate an interference pattern, see Figure 10.4.
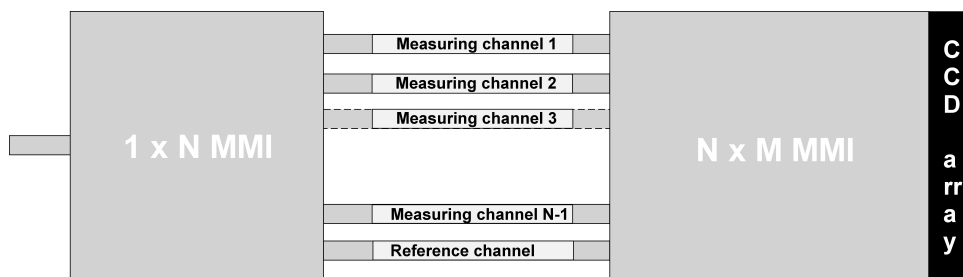

Figure 10.4 *Schematic layout of an MMI-based multichannel YI device: a 1 x N MMI splitter is used to equally split the input light to N output channels and a second MMI combiner is used to combine the light from the N channels.*

A CCD camera can be positioned at the endface of the MMI combiner to record the interference pattern generated. If one of the channels of 1 x *N* MMI is chosen as a reference channel and the other *N* - 1 as measuring channels, then in principle *N* - 1 binding events can be monitored simultaneously.

An advantage of this multichannel YI configuration compared to the current one is that the CCD camera is positioned at the endface of the second MMI and the influence of air medium that is present in the space gap between chip endface and the CCD camera will be avoided. This can lead to the improvement of the interference pattern stability, and furthermore, improvement of the resolution of these type of sensors. Another aspect of such a configuration is that splitting of the input light to a large number of channels can be realized in a relatively short distance, as compared e.g. to Y-splitters [7]. As a result, longer sensing windows can be implemented, which directly contributes to the increase of the sensitivity. A disadvantage of this configuration is that fabrication of an MMI structure is more critical than that of a Y-junction. In addition, mounting of the CCD camera at the endface of the MMI requires further investigations.

10.4.3   Multichannel MZI

In a similar way as for the YI, the MMI's can be used to realize a multichannel MZI sensor. In that case, a 1 x *N* MMI splits the input light to *N* output channels and an *N* x *M* MMI combines the light from two particular parallel channels to certain output channels where the interference intensity can be measured as in a normal MZI [9]. In Figure 10.5, a schematic layout of such a configuration is presented.
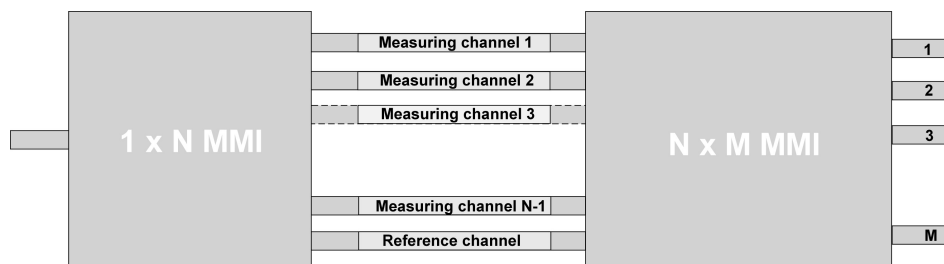

Figure 10.5 *Schematic layout of an MMI-based MZI multichannel sensor: a 1 x N MMI splitter is used to equally split the input light to N channels and an N x M MMI combiner is used to combine the light from the N channels to M output channels.*

137

In addition, it is possible that the light from two particular channels can be combined to a number of output channels, in which the phase of the signal is shifted from one to another [10]. This property can be used to measure the signal between two input channels always close to the high sensitivity regime without the need for implementation of a phase modulation, resulting in a simpler chip design and operation principle.

Compared to the MMI-based YI, the number of processes that can be monitored here might be smaller because for each measuring channel a reference channel is needed. On the other hand, mounting of the CCD camera at the endface of the MMI for the YI configuration requires further investigations.

10.4.4   2D-multisensing YI

If a binding event will take place on top of an MMI central structure within the evanescent field of the guided modes, then the propagation constant of these modes will be changed, resulting in a change of the phase of each mode, and further in a change of the interference pattern, which is related to the binding event. By measuring this change, the binding event can be derived.

The area of the MMI coupler can be divided in N x M regions, which have e.g. a width of W_{MMI}/N, and a length of L_{MMI}/M, where W_{MMI} and L_{MMI} indicate the width and length of the MMI central structure, respectively (see Figure 10.6). If each of these areas will be covered with a given receptor layer, which specifically binds to a given analyte, a certain phase change will result for each area, and the total phase change at the endface of the MMI will be the sum of all individual phase changes along each row.
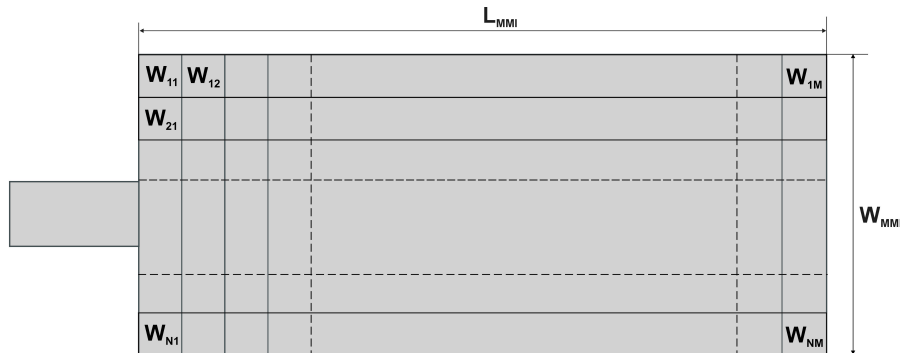

Figure 10.6 *Top-view of an MMI coupler divided in N x M sensing areas, which have a width of W_{MMI}/N and a length of L_{MMI}/M, where W_{MMI} and L_{MMI} are respectively the width and length of the MMI central structure; w_{ij} indicates the sensing window in ith row and jth column.*

138

A readout method, e.g. a Fourier analysis, has to be developed for analyzing the interference pattern recorded at the endface of the MMI structure. In addition, the scattered light from the top of the structure can be recorded. In that case, when binding events occur in the sensing areas, the intensity of the scattered light from these areas may change, which further may give an indication about the number of molecules bound or thickness of layer formed, etc. Analyzing the signal achieved from both methods, more information may be obtained for the binding event taking place on each sensing window.

An advantage of this configuration is that there is no need to divide the light into different channels, in that way diminishing radiation and propagation losses, but on the other hand there will be high scattering losses from sensing areas implemented on the top of the MMI. This configuration may result in an increase of the number of processes that can be monitored simultaneously compared to the present interferometric configurations. A drawback however might be analysis of a more complicated interference pattern.

Compared to configuration discussed in section 10.2, for the 2D-multisensing YI there is no need to split the light into different channels, but on the other hand, signal analysis is more complicated.

10.5   Summary

Some new approaches for development of multichannel interferometric sensing systems have been presented.

A new approach for development of a multichannel MZI by combining the channel outputs with each other and recording the interference pattern generated in the time domain by a PD, and analyzing it using an FFT algorithm, has been described. Furthermore, a new multichannel approach is presented, in which two sets of parallel channels perpendicular with each other are combined such that crossing areas between them can be considered as sensing areas where different binding events may take place.

New configurations of YI and MZI sensors may be realized by combining MMI splitters and combiners. For the YI, the new configuration can contribute on the improvement of stability and resolution, and for the MZI it offers the possibility to achieve high sensitivity without use of the modulation.

An MMI might be used for 2D-multisensing purposes as well. In that case, different binding events can be simultaneously studied by applying different receptor layers in sensing areas defined on the top of the MMI structure. This approach can allow monitoring of more processes compared to present configurations.

References

[1] A. Brandenburg, Differential refractometry by an integrated-optical Young interferometer, Sensors and Actuators B 38-39, 266-271 (1997).

[2] R.G. Heideman and P.V. Lambeck, Remote opto-chemical sensing with extreme sensitivity: design, fabrication and performance of a pigtailed integrated optical phase-modulated Mach-Zehnder interferometer system, Sensors and Actuators B 61, 100-127 (1999).

[3] G.H. Cross, A.A. Reeves, S. Brand, J.F. Popplewell, L.L. Peel, M.J. Swann, and N.J. Freeman, A new quantitative optical sensor for protein characterization, Biosensors and Bioelectronics 19, 383-390 (2003).

[4] K. Wörhoff, P.V. Lambeck, N. Albers, O.F.J Noordman, N.F. van Hulst, and T.J.A. Popma, Optimization of LPCVD Silicon onxynitride growth to large refractive index homogeneity and layer thickness uniformity, Proc. SPIE 3099, 257-268 (1996).

[5] K. Wörhoff, A. Driessen, P.V. Lambeck, L.T.H. Hilderink, P.W.C. Linders, and T.J.A. Popma, Plasma enhanced chemical vapour deposition of silicon oxynitride optimized for application in integrated optics, Sensors and Actuators B 74, 9-12 (1999).

[6] K. Wörhoff, L.T.H. Hilderink, A. Driessen, and P.V. Lambeck, Silicon oxynitride - A versatile material for integrated optics applications, Journal of the Electrochemical Society 149 (8): F85-F91 (2002).

[7] L.B. Soldano and E.C.M Pennings, Optical multimode interference devices based on self-imaging – principles and applications, Journal of Lightwave Technology 13, 615-627 (1995).

[8] L. Soldano, Multimode interference couplers: design and applications, Ph.D. Thesis, Delft University of Technology, The Netherlands, 1994.

[9] R.G. Heideman, R.P.H. Kooyman, and J. Greve, Performance of a highly optical waveguide Mach-Zehnder interferometer immunosensor, Sensors and Actuators B 10, 209-217 (1993).

[10] M. Bachmann, P.A. Besse, and H. Melchior, General self-imaging properties in N x N multimode interference couplers including phase relations, Applied Optics 33, 3905-3911 (1994).

Summary

In food industry, health care, etc., there is a high need for bio-chemical sensing systems that are sensitive, accurate, selective, and multipurpose. These sensing systems can be used for detection of an analyte concentration in a given sample solution such as pesticides in milk, virus particles such as HIV and SARS in a blood sample, etc. Integrated optical (IO) interference-based sensors offer a good possibility for realization of such sensing systems, being extremely sensitive and offering the prospect for development of multichannel configurations. In this thesis, we describe the design, realization, and characterization of a highly sensitive multichannel IO Young interferometer (YI) immunosensor.

In Chapter 2, a theoretical analysis of the multichannel YI sensor is presented. The principle of a two-channel YI is expanded to a multichannel device by choosing different distances between output channels such that each pair of channels functions as a two-channel YI with a unique distance between its two arms. Calculations show that phase errors of ~ 10% of the phase signal are caused by a mismatch between spatial frequencies of the individual interference patterns and those determined by the pixel distances of the CCD camera used to measure the interference pattern, originating from the Fast Fourier Transform (FFT) algorithm used for signal analysis. A scheme is proposed to reduce this error by a factor of 5.

In Chapter 3, the multichannel IO YI sensing system is designed based on a number of requirements related to the performance such as high resolution, simultaneous readout of all channels, etc., and according to some boundary conditions, e.g. realization of the IO readout system in the Silicon-oxynitride technology. Analysis of the disturbing factors such as temperature difference between channels has introduced some more requirements for the design of the sensor system. The final design of the multichannel IO YI sensor is presented and the process flow for realization of the optical chip is described

Experimental characterization of the multichannel YI sensor devices is presented in Chapter 4. Different glucose concentrations are measured and a good accordance is found with theory. The two-channel YI, which is realized as a first step towards development of the multichannel sensor, shows a phase resolution of ~ 1.5 x 10^{-5} x 2π (refractive index resolution of ~ 3 x 10^{-9}). Next, it is shown experimentally that the four-channel YI sensor can measure three different concentrations of an analyte, such as glucose, simultaneously and independently from each other. Application of different schemes has reduced the phase errors to ~ 3% of the phase signal. We found that the phase resolution for different pairs of channels is ~ 1 x 10^{-4} x 2π, corresponding to a refractive index resolution of ~ 8.5 x 10^{-8}, and the long-term stability is ~ 5 x 10^{-4} x $2\pi \cdot h^{-1}$.

In Chapter 5, the use of the multichannel IO YI as an immunosensor is reported. A pA-modified sensing surface, which promotes proper antibody orientation, is efficiently used to immobilize antibodies at the Si_3N_4 surface, resulting in a

141

surface coverage of ~ 3 mg/m^2. Next, the YI sensor has been successfully used for detection of Human Herpes Simplex virus. We found that the resolution of the YI sensor can approach detection of a single virus particle. Three different measuring channels are used to monitor proteins and viruses simultaneously and to measure different protein concentrations. The results are in good agreement with predictions for specific interaction and show low non-specific binding.

A new method for correction of the drift in the multichannel YI sensor is demonstrated in Chapter 6. The phase information obtained for different channel pairs is used to correct the drift mainly due to temperature differences between measuring and reference channels. This method is experimentally tested by applying it for sensing applications. We found that the drift in the phase can be decreased by one order of magnitude when the new method is applied. Implementation of this technique is possible because the phase change for each channel pair in the multichannel YI sensor can be simultaneously measured.

In Chapter 7, the development of a microfluidic sensing system obtained by bonding a microfluidic system to an IO four-channel YI chip is presented. The microfluidic system is structured in such a way that after bonding to the IO chip each microchannel addresses one sensing window in the four-channel YI sensor. It is found that the implementation of the microfluidics reduces the response time of the sensor by a factor of ~ 20 as compared to a bulky cuvette and the volume of the sample solution required is three orders of magnitude smaller. Because of this, a better discrimination between the refractive index change of the sample solution and the layer formation can be made in an immunoreaction, resulting into a higher accuracy and offering the prospect for using the kinetics of the immunoreaction.

In Chapter 8, a novel approach, consisting of simultaneous use of three different wavelengths for discrimination of the refractive index change, thickness of a bound layer, and temperature change, is presented.

In Chapter 9, some conclusions that concern the development of the multichannel IO YI sensor and its use for different applications are discussed. A comparison between the multichannel YI sensor and other interferometric sensors, as well as other techniques, is made. This Chapter concludes with an outlook concerning further improvement of the performance of the IO YI sensing system.

Some new approaches for future development of the multichannel interference-based sensors are presented in Chapter 10. Here, attention is paid to the improvement of the resolution and multichannel operation of these sensors. Advantages and shortcomings of the new configurations are discussed.

Samenvatting

In de voedingsmiddelen industrie, de gezondheidszorg, etc., bestaat een grote noodzaak voor biochemische sensoren die gevoelig, nauwkeurig, en breed inzetbaar zijn. Deze sensoren kunnen gebruikt worden voor de detectie van concentraties van bepaalde stoffen in een preparaat zoals pesticiden in melk, virus deeltjes zoals HIV en SARS in bloed, etc. Geïntegreerde optisch (IO) interferometrische sensoren bieden een goede mogelijkheid om dergelijke sensoren te realiseren vanwege het feit dat ze een extreem hoge gevoeligheid hebben en omdat het mogelijk is multikanaals configuraties te ontwikkelen. In dit proefschrift beschrijven we het ontwerp, de realisatie en de karakterisatie van een zeer gevoelige multikanaals IO Young interferometer (YI) immuun sensor.

In hoofdstuk 2 wordt een theoretische analyse van de multikanaals YI sensor gepresenteerd. Het principe van een tweekanaals YI wordt uitgebreid naar een multikanaals apparaat waarbij verschillende afstanden tussen de interferometer armen gekozen worden dusdanig dat iedere combinatie van twee armen een tweekanaals YI vormt met een unieke afstand tussen de twee armen. Berekeningen tonen aan dat fasefouten van ongeveer 10% van het fase signaal veroorzaakt wordt door het gebruik van een Fast Fourier Transform (FFT) algoritme, die gebruikt wordt voor de signaal analyse, in combinatie met een 'mismatch' van de ruimtelijke frequenties van het interferentie patroon met die van de ruimtelijke frequenties die bepaald worden door pixel afstanden van de CCD camera die gebruikt wordt om het interferentie patroon te meten. Een procedure wordt voorgesteld die de fasefout reduceert met een factor 5.

In hoofdstuk 3, wordt de multikanaals YI ontworpen uitgaande van een aantal criteria ten aanzien van prestaties zoals gevoeligheid, mogelijkheid tot tegelijkertijd uitlezen van de verschillende kanalen en een aantal randvoorwaarden zoals het gebruik van silicium-oxynitride technolgie voor het vervaardigen van het IO deel van de sensor. Een analyse van storende factoren zoals temperatuur verschillen tussen de kanalen resulteren in additionele voorwaarden ten aanzien van het ontwerp. Het uiteindelijke ontwerp van de meerkanaals IO YI wordt gepresenteerd. Daarnaast wordt een overzicht gegeven van het fabricage proces van het IO deel van de sensor.

Hoofdstuk 4 beschrijft de experimentele karakterisatie van de multikanaals YI sensor. Verschillende glucose concentraties zijn gemeten en een goede overeenkomst met de theorie is gevonden. De tweekanaals YI, die gerealiseerd is als opstap naar een meerkanaals sensor, heeft een fase resolutie van $\sim 1.5 \times 10^{-5} \times 2\pi$ (overeenkomend met een brekingsindex verandering van 3×10^{-9}). Vervolgens is aangetoond dat de vierkanaals sensor gebruikt kan worden om drie verschillende glucose concentraties simultaan en onafhankelijk te bepalen. Het toepassen van de fasefout reductie methoden reduceert deze fout tot $\sim 3\%$ van het fase signaal. De fase resolutie voor de verschillende paren van kanalen is $\sim 1 \times 10^{-4} \times 2\pi$, wat overeenkomt met een brekingsindex resolutie van $\sim 8.5 \times 10^{-8}$. Op langere tijdschaal is de stabiliteit $\sim 5 \times 10^{-4} \times 2\pi \cdot h^{-1}$.

In hoofdstuk 5 wordt het gebruik van de multikanaals IO YI als immuun sensor beschreven. Een middels pA gemodificeerd sensor oppervlak, hetgeen een

143

goede oriëntatie van een antilichaam stimuleert, is succesvol gebruikt voor het immobiliseren van antilichamen op het Si_3N_4 oppervlak. De gevonden oppervlakte dichtheden zijn ~ 3 mg/m^2. Vervolgens is de sensor met succes gebruikt voor de detectie van het Humane Herpes Simplex virus. De door ons gevonden resolutie benaderd die van de detectie van een enkel virus deeltje. Het gelijktijdig gebruik van de drie verschillende kanalen is gebruikt voor het simultaan detecteren van eiwitten en virus deeltjes en het bepalen van verschillende concentraties van eiwitten in een enkele meting. De behaalde resultaten komen goed overeen met de verwachtingen en vertonen slechts een lage niet-specifieke binding.

Een nieuwe methode voor het corrigeren van drift in een multikanaals YI sensor wordt beschreven in hoofdstuk 6. De fase informatie die verkregen wordt van de verschillende kanalen is gebruikt om te corrigeren voor de drift die hoofdzakelijk door temperatuur verschillen tussen de kanalen veroorzaakt wordt. De methode is experimenteel getest en een drift reductie van een factor 10 kan gehaald worden.

In hoofdstuk 7 wordt de ontwikkeling van YI sensor met een geïntegreerde microfluidisch flowsysteem beschreven. Het microfluidische systeem is zo gestructureerd dat na bonding met de IO chip ieder microkanaal een sensor kanaal adresseert. Implementatie van de microfluidica reduceert de reactie tijd van de sensor 20 maal vergeleken met een bulk cuvet. Het benodigde volume van de te meten vloeistof is 3 orders minder. Hierdoor kan een beter onderscheid gemaakt worden tussen een verandering van brekingsindex van de meetvloeistof en een laagdikte verandering tijdens een immuun reactie hetgeen nauwkeurigere metingen mogelijk maakt en uitzicht biedt op het gebruik van kinetiek van de immuun reactie.

In hoofdstuk 8 een nieuwe methode, gebaseerd op het gebruik van drie verschillende golflengten, wordt beschreven. Deze methode moet het mogelijk maken om onderscheid te maken tussen faseverschillen ten gevolge van brekingsindex verandering van de meetvloeistof, laagdikte veranderingen en temperatuur verschillen.

In hoofdstuk 9 de conclusies betreffende de ontwikkeling en toepassingen van de multikanaals IO YI sensor worden besproken. Er wordt een vergelijk gemaakt tussen de multikanaals YI sensor en andere interferometer sensoren waarbij tevens de vergelijking met andere gebruikte technieken gemaakt wordt. Dit hoofdstuk eindigt met een vooruitblik op verdere ontwikkelingen die mogelijk zijn om de prestaties van de IO YI sensor te verbeteren.

Nieuwe sensor principes/ideeën voor toekomstige ontwikkelingen op het gebied van interferometer sensoren worden besproken in hoofdstuk 10. Er wordt aandacht besteed aan het verbeteren van resolutie en het verhogen van het aantal kanalen van dergelijke sensoren. Zowel voor- als nadelen van de sensoren worden behandeld.

144

Acknowledgments

Here, I would like to take this opportunity to thank all those people who have worked and cooperated with me during my research project in the BFT group.

First of all, I would like to thank prof. Jan Greve for giving me the possibility to work on this project, for his enormous support, fruitful discussions, and charismatic supervising during all these years.

In particular, I would like to express my deepest gratitude to my daily supervisor, dr. Hans Kanger, for his continuous encouragement, kind and tactful supervising, and good will to discuss everything about the project and generate new ideas.

A special thank goes to dr. Rob Kooyman who was my first supervisor here in Twente; discussions with him about the project were always very helpful.

I cordially acknowledge Aufried Lenferink for his technical support, especially with the labview programs, and Kirsten van Leijenhorst for assistance in chemical lab.

I would like to express my sincere gratitude to the office manager of the BFT, Sylvia Winters, who always offers an unconditional support; knowing all the answers you are looking for and making you feel comfortable. Special thanks go to Frans Germes for his kind assistance, and of course for the great coffee.

Many thanks go to all members of SMD group: Anthony de Vries, Alma Dudia, Mathilde de Dood, Erik Schreuder, Lily, Martijn van Raaij, Martijn Vervoorn, and Tycho Scholtens for their constructive discussion during the group meetings.

I would also like to thank prof. Paul Lambeck, dr. Rene Heideman, and ing. Robert Wijn for sharing their expertise in integrated optics, for motivating discussions and fruitful collaboration. I am grateful to Tom Beumer, Thijs Wink, and Stefan van Hövell for their support with immunosensing experiments, and Geert Besselink and Richard Schasfoort for their assistance with microfluidics.

Many thanks go to staff members of the MESA$^+$ for their help in the cleanroom. I would like to acknowledge Diana Jurconi who contributed in this project during her exchange program in our group.

My sincere greetings to all PhD students who have been working during these years at the BFT group: P. Kosters, M. Bennink, A. Tibbe, A. Petoukhova, A. Serov, R. Kolkman, E. Krioukov, Y. Aksenov, I. Segers-Nolten, M. Pilatou, N. Uzunbajakava, D. Nikova, R. Kassies, S. Bahatyrova, A. Kharine, J. Huisstede, etc., for their assistance and great atmosphere.

I should like to acknowledge here the hospitality of the Dutch people. Ik ben dankbaar en ik wil iedereen van harte bedanken!

Many thanks go to my high school teacher of physics, Astrit Shatro, for his stimulating lectures. I would like to thank Pellumb Berberi for his continuous support and optimism about this project.

I am very grateful to my parents, my sister, and my brother for their encouragement, enthusiasm, and unconditional love. I would also like to thank my mother-in-law for her continuous interest on my research.

Finally, I am infinitely thankful to Alma for her endless patience, enormous support, and continuous encouragement during my work, and above all, for being always there for me.

Aurel Ymeti

Curriculum vitae

Aurel Ymeti was born in Skrapar, Albania, on December 11, 1972. He received the high school diploma in Poliçan, Skrapar, in 1991. From 1991 to 1996, he studied physics at the Faculty of Natural Sciences, University of Tirana, Tirana, Albania. After receiving the MSc degree in July 1996, he was appointed as a teaching assistant in the Department of Physics at the Polytechnic University of Tirana, Tirana, Albania. In 1997 he went to the University of Siegen, Siegen, Germany, to follow an international graduate program in physics. Since 1999, he has been working as a PhD in the Biophysical Techniques Group (BFT) at the University of Twente, Enschede, The Netherlands, under the supervision of prof.dr. J. Greve. His research work deals with development of multichannel integrated optical interferometric immunosensors. The results of the research are described in this thesis.

PUBLICATIONS

I. Journal contributions

1. A. Ymeti, J.S. Kanger, R. Wijn, P.V. Lambeck, and J. Greve, Development of a multichannel integrated interferometer immunosensor, Sensors and Actuators B 83, 1-7 (2002).

2. A. Ymeti, J.S. Kanger, J. Greve, P.V. Lambeck, R. Wijn, and R.G. Heideman, Realization of a multichannel integrated Young interferometer chemical sensor, Applied Optics 42, 5649-5660 (2003).

3. A. Ymeti, J.S. Kanger, J. Greve, G.A.J. Besselink, P.V. Lambeck, R. Wijn, and R.G. Heideman, Integration of microfluidics with a four-channel integrated optical Young interferometer immunosensor, submitted.

4. A. Ymeti, J.S. Kanger, J. Greve, P.V. Lambeck, T. Wink, S.W.F.M. van Hövell, T.A.M. Beumer, R. Wijn, and R.G. Heideman, Sensitive detection of a human virus and proteins using a multichannel integrated Young interferometer sensor, to be submitted.

5. A. Ymeti, J.S. Kanger, J. Greve, P.V. Lambeck, R. Wijn, and R.G. Heideman, Drift correction in a multichannel integrated optical Young interferometer for sensing applications, to be submitted.

6. A. Ymeti, J.S. Kanger, J. Greve, P.V. Lambeck, R. Wijn, and R.G. Heideman, A theoretical approach for discrimination of the refractive index change, thickness of an adsorbed layer, and temperature change in an interferometric sensor using multiple wavelengths, in preparation.

II. Conference contributions

1. A. Ymeti, J.S. Kanger, R. Wijn, P.V. Lambeck, and J. Greve, Building of a highly sensitive two-channel integrated optical Young interferometer as the first step towards constructing an integrated multichannel interferometer immunosensor, Oral presentation and Proceedings of the Sensor Technology Conference 2001, Enschede, The Netherlands, May 14-15, 2001, 31-36. [isbn: 0-7923-7012-0]

147

2. A. Ymeti, J.S. Kanger, R. Wijn, P.V. Lambeck, and J. Greve, Development of a multichannel integrated interferometer immunosensor, Poster presentation and Proceedings of the 11th International Conference on Solid-State Sensors and Actuators, Transducers '01 and Eurosensors XV, Munich, Germany, June 10-14, 2001, 354-357. [isbn: 3-540-42150-5]

3. A. Ymeti, J.S. Kanger, J. Greve, P.V. Lambeck, R. Wijn, and R.G. Heideman, Construction of a four-channel integrated optical Young interferometer, Oral presentation at the 9th International Meeting on Chemical Sensors, Boston, USA, July 7-10, 2002.

4. A. Ymeti, J.S. Kanger, J. Greve, P.V. Lambeck, R. Wijn, and R.G. Heideman, Realization and characterization of a four-channel integrated optical Young interferometer, Poster presentation and Proceedings of the 12th International Conference on Solid-State Sensors, Actuators and Microsystems, Boston, USA, June 8-12, 2003, 1192-1196. [isbn: 0-7803-7731-1]

III. Workshop contributions

1. A. Ymeti, J.S. Kanger, R. Wijn, P.V. Lambeck, and J. Greve, Building of a highly sensitive integrated optical Young interferometer: towards a multichannel immunosensor, Poster presentation at the Workshop "Biomimetics - How does the nature do materials science?", d'Amelander Kap – Ameland, The Netherlands, May 28 - June 01, 2001.

2. A. Ymeti, J.S. Kanger, J. Greve, P.V. Lambeck, R. Wijn, and R.G. Heideman, Multichannel integrated optical Young interferometer, Poster presentation at the Workshop "The Sense of Contact IV", Zeist, The Netherlands, March 20-21, 2002.

3. A. Ymeti, J.S. Kanger, J. Greve, P.V. Lambeck, R. Wijn, and R.G. Heideman, Realization of a four-channel integrated optical Young interferometer, Presentation and Proceedings of the Workshop "The Sense of Contact V", Wageningen, The Netherlands, March 12-13, 2003. [isbn: 90 73461 359]

IV. Patent applications

1. A. Ymeti, J.S. Kanger, and J. Greve, Optical Analysis, Patent application (February 06, 2004). (This patent is based on the results presented in chapter 6).